Characterization of the Structural and Optical Properties of III-V Semiconductor

Materials for Solar Cell Applications

by

Hongen Xie

A Dissertation Presented in Partial Fulfillment
of the Requirements for the Degree
Doctor of Philosophy

Approved Oct 2016 by the
Graduate Supervisory Committee:

Fernando A. Ponce, Chair
Peter A. Crozier
Martha R. McCartney

ARIZONA STATE UNIVERSITY

December 2016

ABSTRACT

The work contained in this dissertation is focused on the structural and optical properties of III-V semiconductor structures for solar cell applications. By using transmission electron microscopy, many of their structural properties have been investigated, including morphology, defects, and strain relaxation. The optical properties of the semiconductor structures have been studied by photoluminescence and cathodoluminescence.

Part of this work is focused on InAs quantum dots (QDs) embedded in AlGaAs matrices. This QD system is important for the realization of intermediate-band solar cells, which has three light absorption paths for high efficiency photovoltaics. The suppression of plastic strain relaxation in the QDs shows a significant improvement of the optoelectronic properties. A partial capping followed by a thermal annealing step is used to achieve spool-shaped QDs with a uniform height following the thickness of the capping layer. This step keeps the height of the QDs below a critical value that is required for plastic relaxation. The spool-shaped QDs exhibit two photoluminescence peaks that are attributed to ground and excited state transitions. The luminescence peak width is associated with the QD diameter distribution. An InAs cover layer formed during annealing is found responsible for the loss of the confinement of the excited states in smaller QDs.

The second part of this work is focused on the investigation of the $In_xGa_{1-x}N$ thin films having different bandgaps for double-junction solar cells. $In_xGa_{1-x}N$ films with x

i

≤ 0.15 were grown by metal organic chemical vapor deposition. The defects in films with different indium contents have been studied. Their effect on the optical properties of the film have been investigated by cathodoluminescence. $In_xGa_{1-x}N$ films with indium contents higher than 20% were grown by molecular beam epitaxy. The strain relaxation in the films has been measured from electron diffraction patterns taken in cross-sectional TEM specimens. Moiré fringes in some of the films reveal interfacial strain relaxation that is explained by a critical thickness model.

To my family for their unconditional support.

ACKNOWLEDGMENTS

TABLE OF CONTENTS

LIST OF TABLES

LIST OF FIGURES

<div align="center">

CHAPTER 1

INTRODUCTION TO III-V COMPOUND SEMICONDUCTORS

</div>

1.1. General properties of III-V compound semiconductors

III-V compound semiconductors are made of atoms from group III element such as Al, Ga, and In, and group V elements such as N, P, and As. (Fig. 1.1) In III-V semiconductors, atoms form a tetrahedrally coordinated structure. One inner-shell s-orbital and three outer-shell p-orbitals in one atom reorganize themselves to form four-fold degenerate hybrid orbitals with a 109.47° angle between each other. Two atoms from different groups align in such a way that maximize the overlap of the directional hybrid orbitals. As a result of this tetrahedral configuration, III-V semiconductors are usually found in a zincblende or wurtzite structure.

III	IV	V
B	C	N
Al	Si	P
Ga	Ge	As
In	Sn	Sb

Figure 1.1. Elements of groups III, IV, and V in the first four rows of the periodic table.

Compared with elementary semiconductors such as silicon, most III-V compound semiconductors such as GaAs, InP, GaN, etc. have a direct band gap (except for AlAs, AlSb, GaP), which makes them widely used in the optoelectronic applications. The

band gap of III-V semiconductors can be engineered by forming alloys. For example, the band gap of $In_xGa_{1-x}N$ can theoretically cover the range from 0.7 to 3.4 eV, which can be even extended to 6.2 eV if AlN is incorporated.[1] This capability does not only allow the alloy semiconductor to emit photon at any designed energy in a range but also provides more possibilities in the design of nanostructures such as quantum wells, quantum dots, etc. to achieve new properties.

Among all the III-V semiconductors, the three materials that have attracted most attentions are GaAs, InP and GaN. GaAs and its alloys have been extensively studied since 1950's, InP system since 1970's and GaN system since 1990's. Recently, InAs quantum dot/GaAs system has been used to explore the possibilities of intermediate band solar cells and modification of this system using alloys such as AlGaAs,[2] InGaP,[3] GaAsSb,[4] is being studied to improve the solar cell performance. On the other hand, a lot of efforts are being devoted to understanding the microstructures of $In_xGa_{1-x}N$ films,[5,6] and to achieve good material quality in order to fabricate optoelectronic devices active in the entire visible and near ultraviolet regions.[7,8]

1.2. GaAs and related alloys

GaAs has a zincblende crystal structure with lattice parameter of 5.56 A. (Fig. 1.2) The Ga and As atoms form two interpenetrating face-centered cubic lattice displaced by a/4[111]. The bandgap of GaAs is 1.424 eV at 300K.
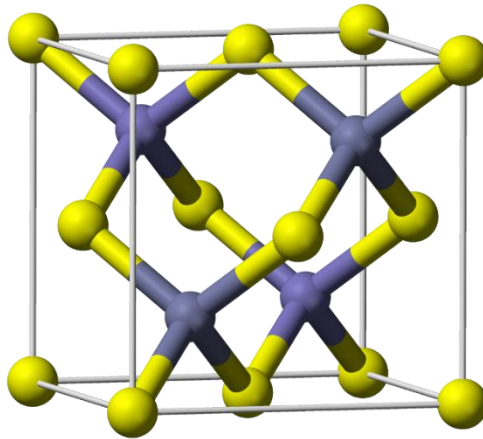
Figure 1.2. Crystal structure of GaAs. The yellow and the grey spheres represent Ga and As atoms, respectively. The line connecting two yellow spheres on base is the lattice parameter equaling 5.56 A.

Bulk GaAs are usually grown by vertical gradient freeze process where single crystal growth propagates from the seed crystal placed at the bottom of the crucible following the temperature gradient. Another technique called liquid encapsulated Czochralski growth using seed crystal to pull a single crystal from an encapsulated melt can produce high-purity single crystal GaAs that exhibits semi-insulating characteristics.[9] The bulk GaAs is sliced to make GaAs wafers which can be used as a substrate to grow epitaxial films. Optoelectronic devices based on thin film GaAs can be fabricated by metalorganic vapor phase epitaxy (MOVPE) and molecular beam epitaxy (MBE) on the GaAs wafers or other substrates such as Si wafers.

GaAs and AlAs have the same lattice structure and similar lattice parameters so their alloys can be easily grown on GaAs substrate. But the band gap of AlGaAs becomes indirect when the AlAs content is higher than ~40%, which limits the usage of this alloy for optoelectronic application at any energy higher than 1.88 eV. GaAs can

3

also form alloys with other III-V semiconductors such as InAs, GaSb, etc. (Fig. 1.3) but

the different in the size of the lattices of the alloy semiconductors and the GaAs

substrate usually leads to generation of defects when either the thickness of the film or

the content of the alloy material exceeds a critical value.[10] However, this lattice

mismatch can be utilized to fabricate self-assembly nanostructures such as QDs.[11]
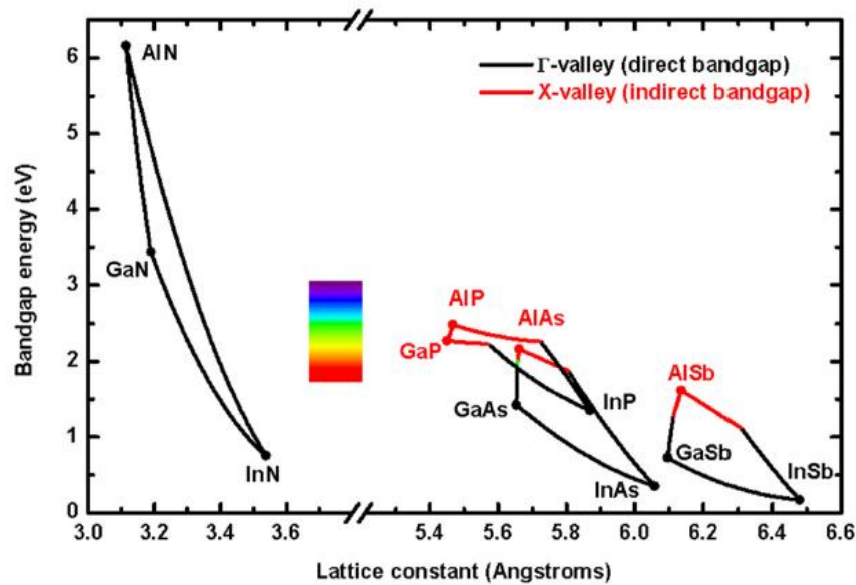
Figure 1.3. The band gap and lattice parameter of various III-V semiconductors. (adapted from Ref. 12)

1.3. GaN and related alloys

GaN is usually grown in the form of wurtzite structure where Ga and N atoms form

two hexagonal close-packed structures displaced in [0001] direction by the length of a

chemical bond. (Fig. 1.4) The lattice parameter on the basal plane is 3.189 A and the

lattice parameter in [0001] direction is 5.189 A. GaN has a direct band gap of 3.4 eV
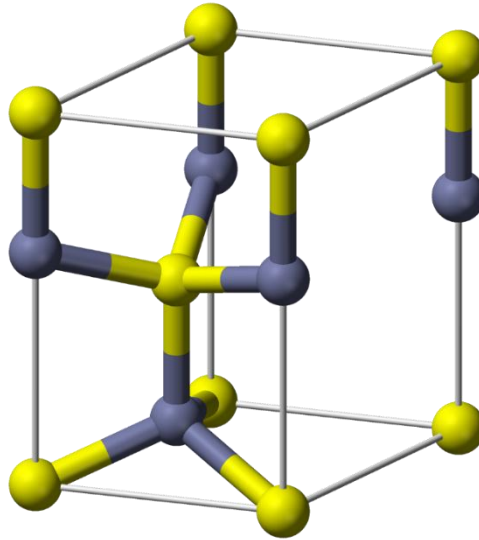
Figure 1.4. Crystal structure of wurtzite GaN. The yellow and grey spheres represent Ga and N atoms, respectively. The lattice parameter a = 3.190 A and c = 5.189 A.

It is difficult to grow bulk GaN from melt because GaN only exhibit congruent melting at very high temperature (2200 °C) and high pressure (6.0 GPa).[13] Currently, commercial GaN substrate are manufactured by growing thick GaN using hydride vapor phase epitaxy (HVPE) on another substrate such as Si, sapphire, GaAs, etc. However, the cost of GaN substrates limits its use in most optoelectronic devices such as LED, etc. Most devices are still fabricated by MOVPE or MBE on sapphire substrates.

The band gaps of GaN, AlN and InN span a wide range from 0.7 eV to 6.2 eV which opens great possibilities for optoelectronic devices. Growth of AlGaN alloy or $In_xGa_{1-x}N$ alloy on GaN or AlN template is a challenge due to the large lattice mismatch between the epitaxial films and the underlying templates (Fig. 1.3). Dislocations forms during growth to accommodate the accumulating strain in the film.[14–16]

In addition to the lack of lattice-matching substrate, another challenge for the growth of InGaN with high indium contents is attributed to the miscibility gap of InN-GaN binary system. The alloy is not a thermodynamic stable phase if its composition falls in the miscibility gap. The thermodynamic stable state under constant pressure and temperature has the lowest Gibbs free energy. The change of Gibbs free energy due to mixing of indium and gallium anions in the formation of InGaN has two components:

$$\Delta G_{mix} = \Delta H_{mix} - T\Delta S_{mix} \qquad (1.1)$$

where ΔG_{mix}, ΔH_{mix} and ΔS_{mix} are the change of Gibbs free energy, enthalpy and entropy by mixing. ΔS_{mix} always has a position value because mixing increase the disorder of the system and pushes the mixing process. ΔH_{mix} equals the energy required for breaking of interatomic bonds in the pure GaN and InN and forming new bonds in the mixed system. The large difference in the interatomic spacing between InN and GaN leads to a positive ΔH_{mix} due to bond distortion in the alloy, which gives rise to the solid phase miscibility gap (Fig. 1.5).[17] The bimodal curve shows that InN solubility in GaN as a function of temperature. $In_xGa_{1-x}N$ with indium content lower than the solubility limit is thermodynamically stable and can usually be grown with a good quality. $In_xGa_{1-x}N$ alloys with content in the range delimited by the bimodal and spinodal curves are metastable, which means phase separation can be suppressed if large compositional fluctuation is absent. In the region below the spinodal curve, any single phase $In_xGa_{1-x}N$ film is unstable and will spontaneously separate into two phases without any thermodynamic barrier. When the $In_xGa_{1-x}N$ layer is grown epitaxially on

GaN substrate, the elastic strain energy in the film cause an increase of the Gibbs free

energy of high indium $In_xGa_{1-x}N$. The misfit strain shifts the miscibility gap to the high

indium end as shown in Fig. 1.6.[18] However, the strain relaxation in the epitaxial layer

may return the miscibility gap back to the situation of an unstrained layer.
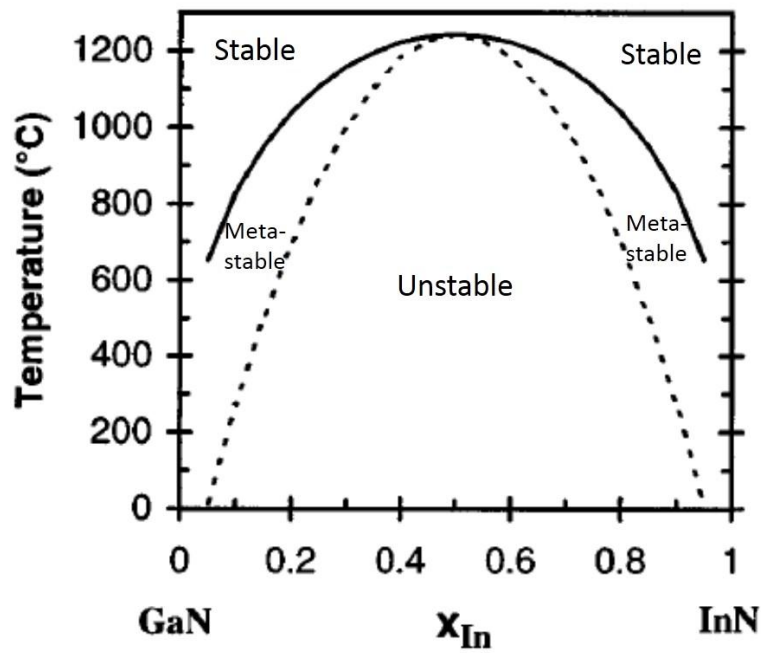
Figure 1.5. Phase diagram of GaN-InN alloy. The solid line shows the binodal curve which separate the stable and metastable domain. The dash line shows the spinodal curve which separates the metastable and unstable domain. (adapted from Ref. 17)
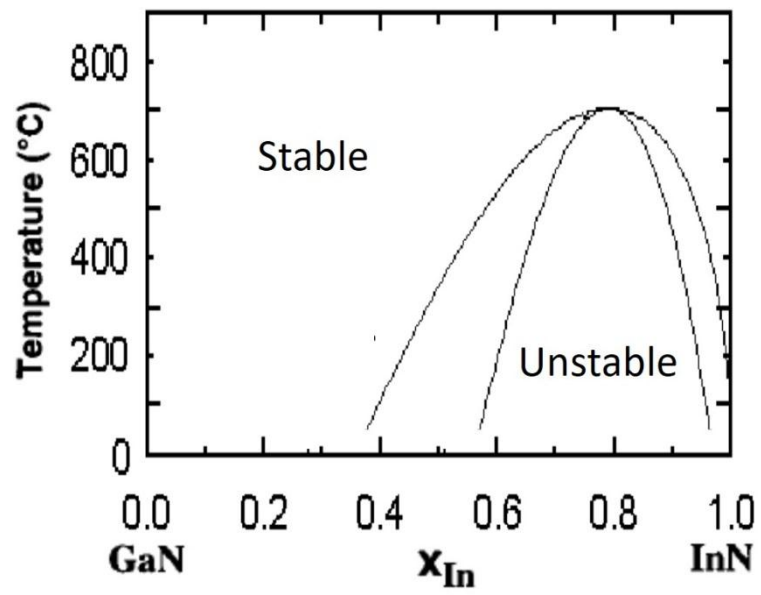
Figure 1.6. Phase diagram of strained $In_xGa_{1-x}N$ on GaN. The unstable domain is shifted towards the high indium end. (adapted from Ref. 18)

CHAPTER 2

DEFECTS IN ZINCBLENDE AND WURTZITE STRUCTURES

2.1. Misfit dislocations

2.1.1. Strain relaxation in epitaxial films by misfit dislocations

Lattice mismatch between the epitaxial film and the substrate is defined as

$$f = \frac{a_{film} - a_{substrate}}{a_{substrate}} \qquad (2.1)$$

where a_{film} and $a_{substrate}$ are the lattice parameters of the film and the substrate, respectively. When the film has a larger lattice parameter than the substrate, a compressive strain develops in the film. On the contrary, a tensile strain is resulted from a film with a smaller lattice parameter than the substrate. (Fig. 2.1)
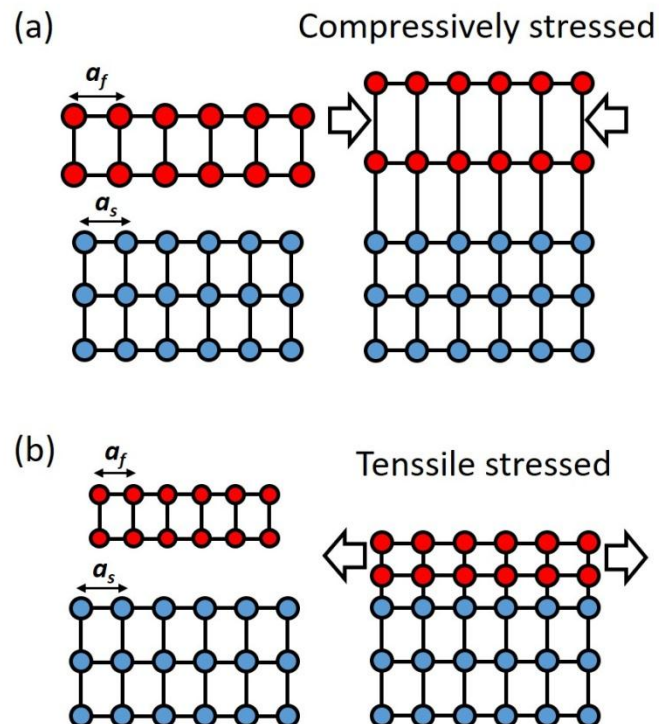
Figure 2.1. Misfit strain due to the lattice mismatch between the film and the substrate, corresponding to compressive and tensile stresses.

The free surface has no restriction so the stress normal to surface is zero and the

film is thin so the problem can be reduced to a plane-stress situation. Generally, only

normal strain and normal stress are produced as a result of lattice mismatch.[19] Assuming

isotropic mechanical properties, the in-plane strain in an epitaxial film is given by:

$$\varepsilon_{xx} = \varepsilon_{yy} = \varepsilon = \frac{a_{film} - a_{substrate}}{a_{film}} \tag{2.2}$$

$$\varepsilon_{xy} = 0 \tag{2.3}$$

where ε_{xx} and ε_{yy} are the in-plane strain in x and y directions, ε is the misfit strain

(also called "eigen strain"), ε_{xy} is the in-plane shear strain. The relationship between

strain and stress are given by the constitutive equations in tensor form:

$$\begin{bmatrix} \sigma_{xx} \\ \sigma_{yy} \\ \sigma_{xy} \end{bmatrix} = \frac{2G}{1-v} \begin{bmatrix} 1 & v & 0 \\ v & 1 & 0 \\ 0 & 0 & (1-v)/2 \end{bmatrix} \begin{bmatrix} \varepsilon_{xx} \\ \varepsilon_{yy} \\ 2\varepsilon_{xy} \end{bmatrix} \tag{2.4}$$

where σ_{xx} and σ_{yy} are the normal stress in x and y directions, σ_{xy} is the in-plane

shear stress. The in-plane stresses are:

$$\sigma_{xx} = \sigma_{yy} = 2G\frac{1+v}{1-v}\varepsilon \tag{2.5}$$

$$\sigma_{xy} = 0 \tag{2.6}$$

where G is the shear modulus, v is the Poisson's ratio. The strain energy per unit area

is:

$$U = \frac{1}{2}(\sigma_{xx}\varepsilon_{xx} + \sigma_{yy}\varepsilon_{yy})h = 2G\frac{1+v}{1-v}\varepsilon^2 h \tag{2.7}$$

where h is the thickness of the film. When a film with large lattice mismatch to the

substrate is epitaxially grown, strain builds up in the film until a point at which it can

be relaxed by generation of misfit dislocations. A misfit dislocation can introduce or

remove a lattice plane at the interface on the film side (Fig. 2.2(a)) compressing or

stretching the film by an amount equal to the in-plane edge component of Burgers vector of the dislocation, $b_\perp$. (Fig. 2.2(b)) The decrease of misfit strain energy by an array of misfit dislocations is:

$$\Delta\varepsilon = -b_\perp/d \qquad\qquad (2.8)$$

where d is the spacing between dislocations. The in-plane edge component of the Burgers vector has to be determined in each specific case.
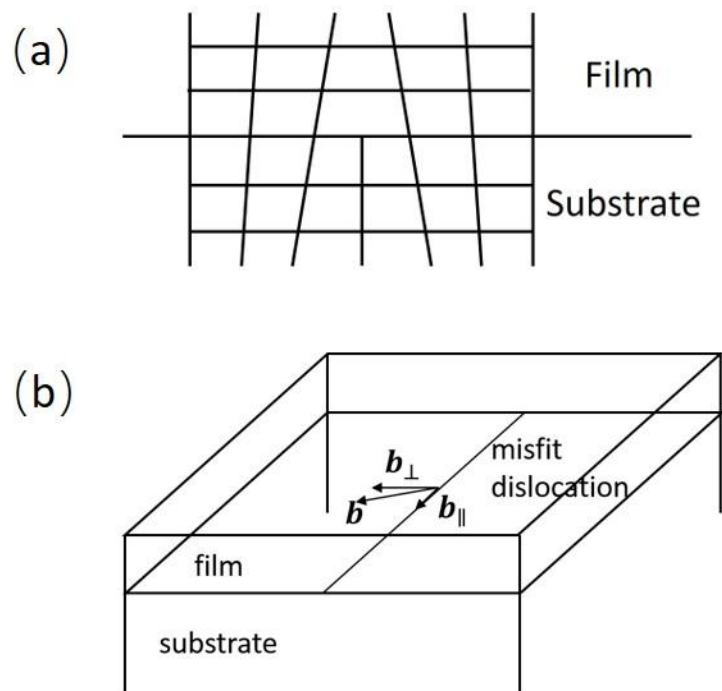
Figure 2.2. A misfit dislocation at an interface. (a) A missing plane in the film associated with a misfit dislocation. (b) Schematic diagram showing the in-plane edge component of the Burgers vector of a misfit dislocation.

2.1.2. Critical thickness for dislocation generation

The strain energy in a film increases with the thickness of the film. When the strain energy is larger than the energy necessary to generate a dislocation, plastic relaxation takes place.[20] The energy per unit length associated with an isolated edge dislocation

is:[21]

$$U_d = \frac{Gb^2}{4\pi(1-\nu)}\left[ln\left(\frac{3h}{b}\right)\right] \approx \frac{Gb^2}{4\pi(1-\nu)}\left[ln\left(\frac{h}{b}\right)+1\right] \qquad (2.9)$$

By equating misfit strain energy and the energy associated with a dislocation, a critical thickness for the generation of dislocation is obtained. In the model, the critical thickness is estimated for a film grown on a substrate which is initially free of dislocations.[20]

Another model considers the force balance between the two forces acting on an existing dislocation – one is the force exerted by the misfit strain (F_a) and the other is the force due to dislocation line tension (F_l).[22] The force due to misfit strain is

$$\mathrm{F}_a = 2G\frac{1+\nu}{1-\nu}bh\varepsilon\,cos(\lambda) \qquad (2.10)$$

where λ is the angle between the Burgers vector and the direction on the interfacial plane that is perpendicular to the dislocation line, $b\,cos(\lambda)$ is the in-plane edge component of the Burgers vector that contributes to relaxation. The dislocation line tension is

$$F_l = \frac{Gb^2}{4\pi}\frac{1-\nu\,cos^2(\alpha)}{1-\nu}\left[ln\left(\frac{h}{b}\right)+1\right] \qquad (2.11)$$

where α is the angle between the misfit dislocation and its Burgers vector. When the two forces equal, a critical thickness is obtained for misfit strain relaxation starting from a pre-existing dislocations.[22]

2.2. Stacking faults

Stacking faults form when the original stacking sequence is disturbed. In face centered cubic (FCC) structure, each close-packed {111} plane shifts by 1/6<-211>

with respect to the former plane. The total three possible positions of the {111} planes are labelled by A, B and C. The stacking sequence of a zincblende structure is then written as …ABCABC… The removal of one layer "A" leads to a stacking sequence of …AB<u>CB</u>CA…, known as an intrinsic stacking fault (Fig. 2.3(a)). The intrinsic stacking faults are usually bound by partial dislocations with Burgers vectors equaling 1/6<-211>. Shockley partial dislocations are the ones that lead to the formation of a stacking fault. The insertion of an extra layer "B" leads to a stacking sequence of ...ABC<u>B</u>ABC…, known as an extrinsic stacking fault (Fig. 2.3(b)). The dislocation at the boundaries of extrinsic stacking faults are known as Frank partial dislocations with Burgers vectors equaling 1/3<111>.
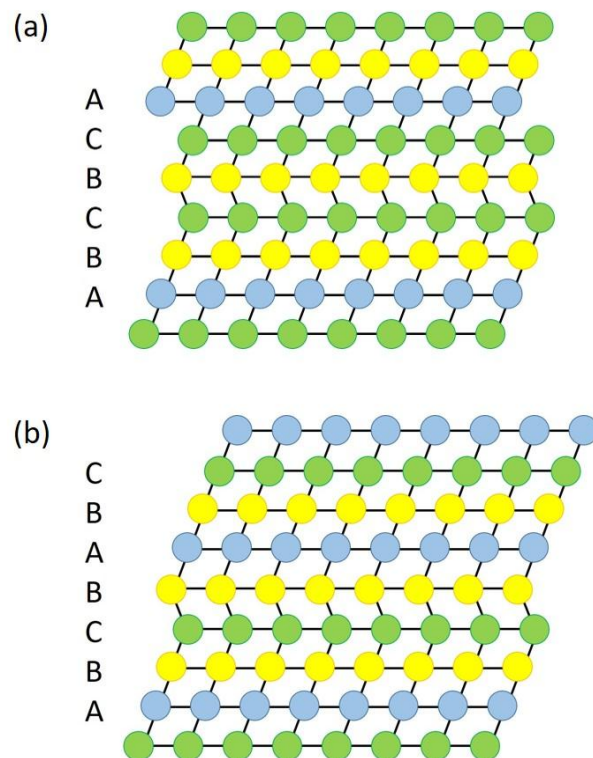
Figure 2.3. Stacking faults in FCC. (a) An intrinsic stacking fault, where an "A" plane is missing. (b) An extrinsic stacking fault, where a "B" plane has been inserted into the normal stacking sequence.

In hexagonal close-packed (HCP) structures, the close-packed planes are the {0001} planes. The stacking sequence is …ABABAB… Insertion of one extra layer leads to an extrinsic stacking fault associated with a shift of 1/2<0001>. The stacking sequence becomes …ABA<u>C</u>BAB… (Fig. 2.4(a)). When removing a basal plane, there are two possible intrinsic stacking faults. One is related to a shift of one layer by 1/3<1-100> and is denoted as I_2SF. The corresponding stacking sequence is …ABACBC… (Fig. 2.4(b)). The other is related to a shift by 1/6<2-203> and is denoted by I_1SF. The corresponding stacking sequence is …ABACAC… (Fig. 2.4(c)). The I_2SF results from a horizontal shift in the {0001} plane and I_1SF results from a combination of a horizontal shift and a vertical shift.
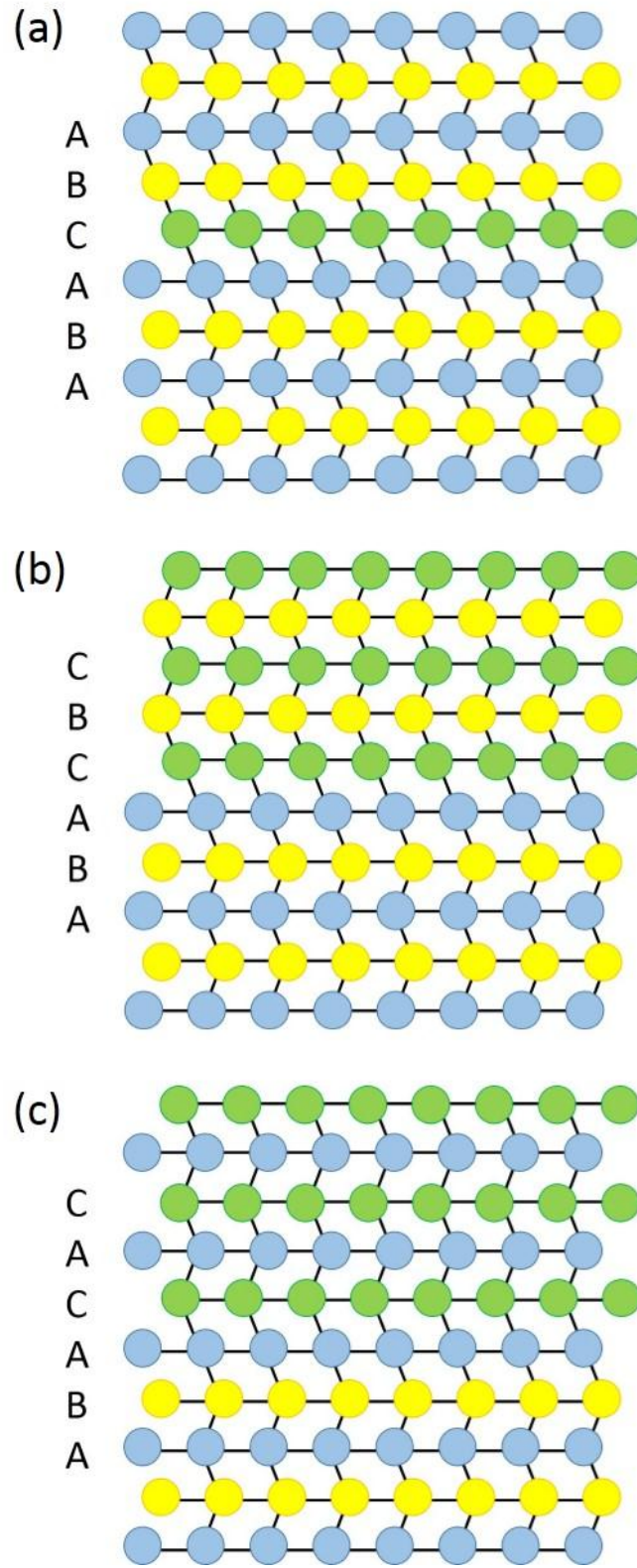
Figure 2.4. Stacking faults in HCP. (a) Extrinsic stacking fault, (b) I_2SF and (c) I_1SF.

CHAPTER 3

EXPERIMENTAL METHODS

3.1. Transmission electron microscopy

Transmission electron microscopy has been and still is heavily used to study semiconductor devices. Several useful techniques for the study of semiconductor devices include two-beam diffraction-contrast imaging, high-resolution imaging, high-angle annular dark field (HAADF) imaging, selected area diffraction (SAD), convergent beam electron diffraction (CBED), electron holography, etc.

3.1.1. Electron diffraction

When an electron beam passes through a thin crystalline sample, the incident electrons that are elastically scattered by the periodically arranged atoms form a diffraction pattern on the back focal plane (BFP) of the objective lens (Fig. 3.1). In the diffraction pattern, each spot corresponds to the reflection by a specific set of planes except the central spot that corresponds to the not-scattered, transmitted beam. The sample is usually thin along the beam direction and as a result the diffracted beams may deviate from the exact Bragg conditions within a small amount which is inversely proportional to the thickness of the sample. As the direction of the electron beam tilts, the diffraction pattern moves on the BFP. The shift of the spots in the diffraction pattern is thus a good indication of the beam tilting and it is useful in for alignment of central dark-field imaging or weak-beam dark-field imaging. Due to inelastic scattering, a Kikuchi pattern which consists of intersecting bands superimposes on the set of spots.

The Kikuchi pattern is formed by the electrons which are scattered at exact Bragg conditions so the bands are good indication of the crystal orientation. The crystal orientation with respect to the beam direction can be aligned using the diffraction spots and the Kikuchi bands as reference.

In an electron diffraction pattern, each diffraction spot corresponds to Bragg reflection of the electron wave by a set of parallel crystal planes. The interplanar spacing and the diffraction angle are related by Bragg's law:

$$2d\sin\theta = n\lambda$$

(3.1)

where d is the interplanar spacing, θ is the Bragg angle, λ is the wavelength depending on accelerating voltage, the and n is a positive integer. The distance in the diffraction pattern is related to the diffraction angle trigonometrically, and the relation can be established by calibration using a known crystal. In the study of epitaxial films, the substrate away from the interface is relaxed and can be used for the calibration. The Bragg angle is then:

$$\theta = \frac{g}{g_{sub}}\theta_{sub}$$

(3.2)

where g is the distance from the central beam spot to the diffraction spot, g_{sub} and θ_{sub} are respectively the distance and Bragg angle corresponding to a known crystallographic plane of the substrate.
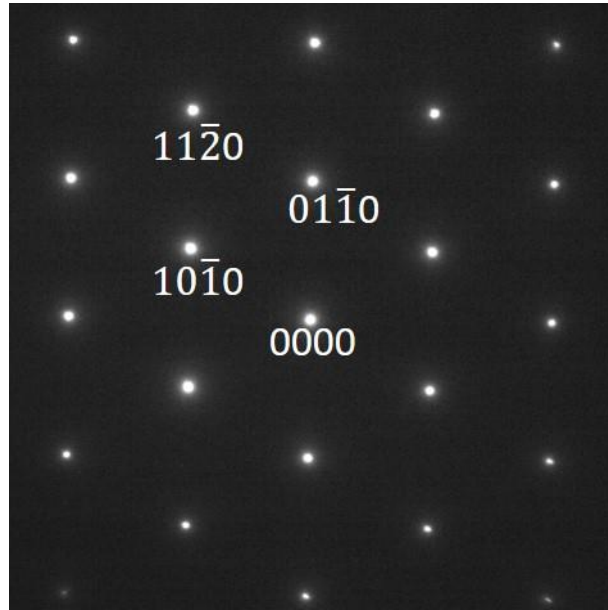
Figure 3.1. An electron diffraction pattern obtained from GaN along [0001] zone axis.

3.1.2. Two-beam diffraction-contrast imaging

For defect analysis, the sample is usually tilted to a so-called "two-beam condition" to excite only one strong diffraction beam (Fig. 3.2(a)) and then either the strong diffracted beam or the transmitted beam is selected to form a dark field or a bright field image (Fig. 3.2(b)). The contrast in the resulting image is due to change of intensity in the diffracted beam as a function of the position on the sample. The contrast is uniform in regions where the sample is uniform with no defects. In the region that is close to a defect such as a dislocation, local bending of crystal planes diffracts the electron beam differently and a dark contrast in the BF image or a bright contrast in a DF image is observed. The Burgers vector of defects can be inferred by comparing the contrast of the defect under different diffraction conditions.[23] For example, the visibility of a dislocation with Burgers vector $\boldsymbol{b}$ under diffraction condition $\boldsymbol{g}$ depends on the value of $\boldsymbol{g} \cdot \boldsymbol{b}$. If $\boldsymbol{g} \cdot \boldsymbol{b} = 0$ meaning that the Burgers vector is parallel to the reflection

18

planes, and no change in contrast is observed.
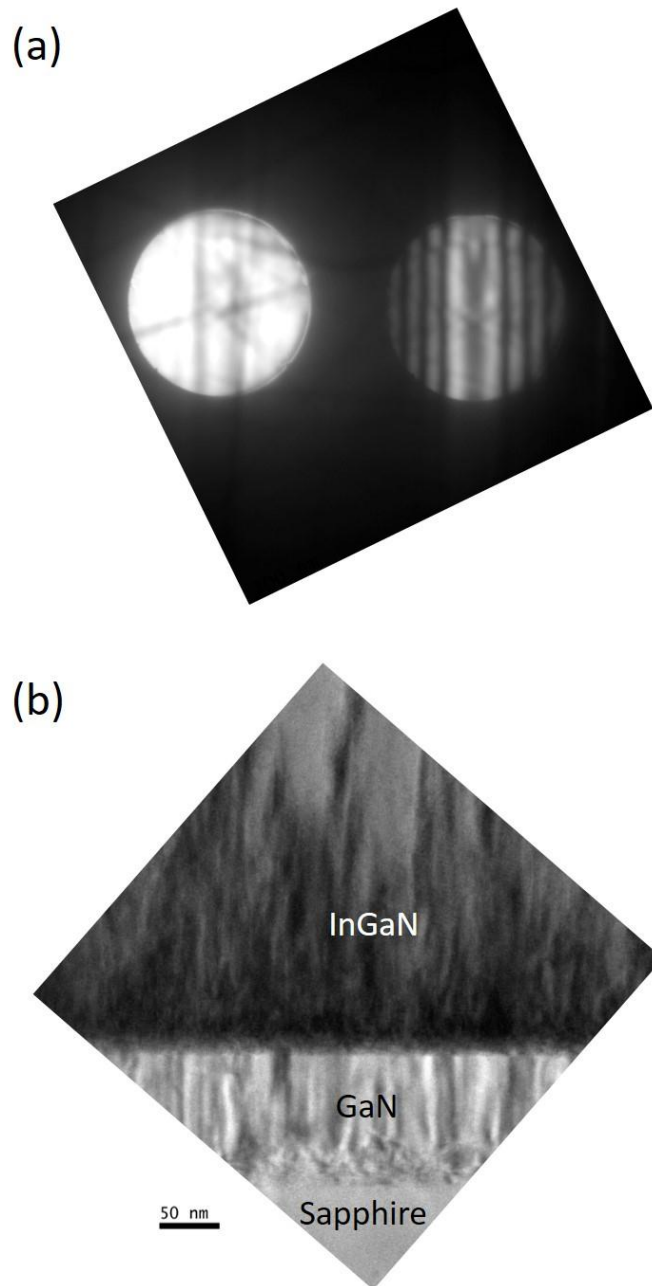
Figure 3.2. Two-beam diffraction-contrast imaging showing an $In_xGa_{1-x}N$/GaN/sapphire heterostructure. (a) A diffraction pattern shows excitation of one strong reflection with a convergent beam. (b) Bright-field image taken in the two-beam condition using $g = 1\bar{1}00$.

3.1.3. High-resolution TEM and STEM imaging

High-resolution TEM can be used to visualize the atomic arrangement in the beam

projection, providing a powerful tool to study the structure of interfaces, defects, etc.

In high resolution TEM, a virtually parallel electron beam traverses the sample, and the

wave front of the plane wave is modified by the periodic atomic potential. The electron

wave close to the atomic columns travels faster and results in a phase advance. If the

sample is thin enough, it can be regarded as a phase object which produce a wave with

a spatially dependent phase shift at the exit surface:[24]

$$\Psi_{exit} = \exp(i\sigma V_z) \tag{3.3}$$

where V_z is the position-dependent projected crystal potential, the interaction constant

$\sigma = \lambda m e/(2\pi\hbar^2)$ is a function of electron wavelength. The spatial distribution of the

wave at the exit surface is imaged by the objective lens and magnified by the projection

lens onto the screen. An example is shown in Figure 3.3.
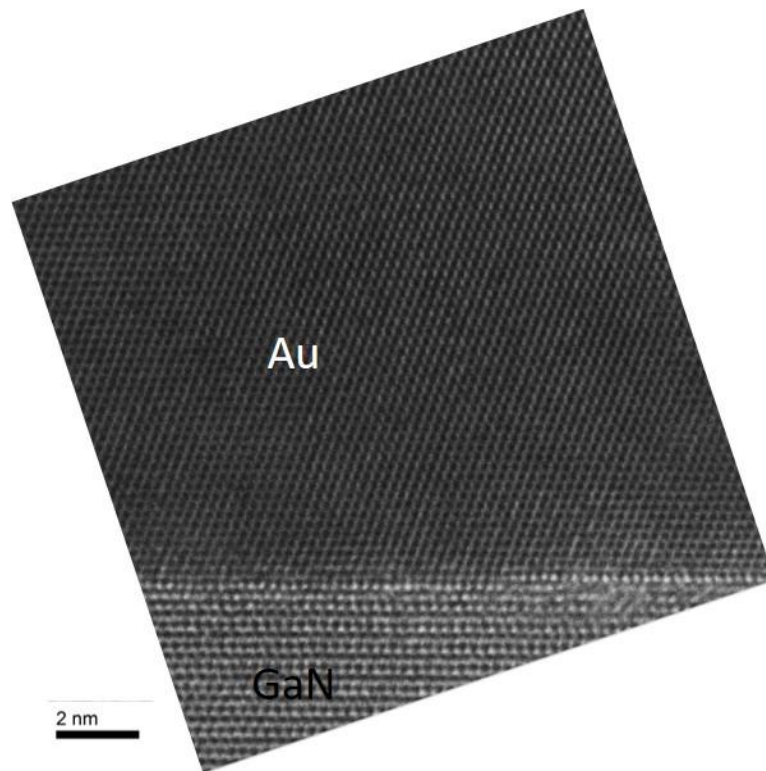
Figure 3.3. HREM image of an Au-GaN contact showing the atomic arrangement at the interface.

In high resolution STEM, the electron beam is focused to a small probe on the sample by the objective lens. The small probe scans over the sample and the signals produced by the interaction of the beam and the sample at each position are collected by various detectors, such as a bright-field detector, an annular-dark-field detector, etc. to record the intensity at a pixel in the image. The electrons that are scattered to high angles (>50 mrad) are sensitive to the average atomic number in the beam projection. Images formed by the high-angle annular dark-field (HAADF) detector are very useful to visualize the content variation at the atomic scale.[25] Figure 3.4 shows a HAADF image of an InAs/AlGaAs interface along a <110> projection.
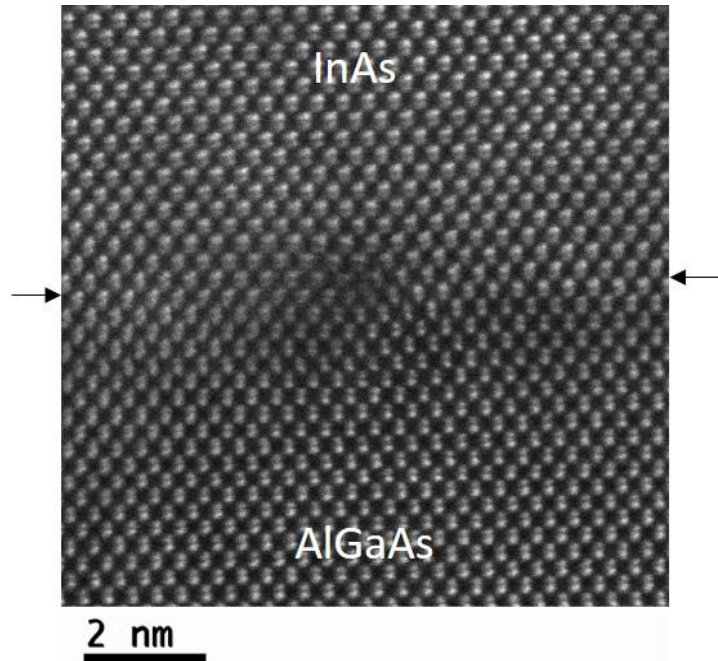
Figure 3.4. A HAADF image of an InAs/AlGaAs interface taken along a <110> projection. The inteface was identified by tracing the brighter contrast from In atomic columns. A misfit dislocation is observed at the InAs/AlGaAs interface.

High-resolution images are usually taken in an axial view so that each atomic column in the beam projection corresponds to a spot in the image. For the zincblende structure, <110> zone axes are preferred to reveal the A-B-C stacking sequence. For the wurtzite structure, <11-20> zone axes are used because (1) the A-B stacking sequence is easily recognized and (2) the interplanar spacing of {1-100} planes observed in <11-20> zones are larger than {11-20} planes observed in <1-100> zones.

3.1.4. Convergent beam electron diffraction

The electron beam can be focused at one position on the sample to form a diffraction pattern from a localized area less than 100 nm in diameter. The convergent beam gives rise to diffraction disks that contain important structural details in the form of higher-order Laue zone (HOLZ) lines and dynamical diffraction effects. The HOLZ

22

lines are useful for strain measurement and the dynamical diffraction effects are useful for the determination of thickness of a small area and extraction of crystallographic symmetry information.

An extended technique called large-angle convergent-beam electron diffraction (LACBED) has been developed defocusing the CBED pattern.[26] Both real space and reciprocal space are presented in a LACBED pattern, which is useful for the study of line defects and planar defects. Figure 3.6 shows splitting of a HOLZ line at its intersection with a dislocation line. The splitting pattern can be used to determine the Burgers vector of the dislocation.[26]
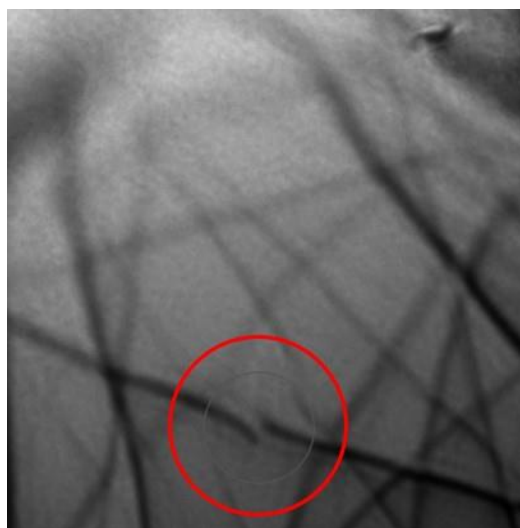
Figure 3.5. LACBED showing HOLZ line splitting (marked by a red circle) due to intersection with a dislocation line.

3.2. Photoluminescence and cathodoluminescence spectroscopy

The optical properties of samples are studied by photoluminescence and cathodoluminescence spectroscopy. In photoluminescence spectroscopy, a laser is used to excite the electrons from the valence band into the conduction band, forming an

electron-hole pair. The electrons and the holes then thermalize to the conduction band minimum and valence band maximum, respectively. The excited carriers can recombine either radiatively or non-radiatively. The radiative recombination can be divided into two types: one is due to recombination of electrons and holes in the conduction and valence band, the other is via impurity levels in the bandgap. The non-radiative recombination happens through phonon scattering or Auger process. Photons can be emitted by radiative recombination. The emission at different wavelengths can be filtered and recorded. The emission as a function of wavelength provides information such as band gap energy, donor and acceptor levels, alloy content, etc.

In cathodoluminescence, an electron beam is used to excite valence electrons into electron-hole pairs. The excitation energy originates from the incident electron beam that has an evergy of several keV, which gets dissipated within the material. Thus, the excitation energy in CL can be much larger than the excitation energy of several eV used in PL measurements. The large excitation energy in CL facilitates the study of wide-bandgap materials. Another advantage of CL is that the electron beam can be focused to study the luminescence characteristics of a small region. The penetration depth of the electron beam can be controlled by the accelerating voltage, which enables us to investigate the depth-dependence of the electronic properties. In addition, a monochromator can be used to select emission at a specific wavelength. Under such conditions, a monochromatic CL image can be recorded as the electron beam scans over an area, and the spatial distribution of the feature corresponding to the selected emission

can be observed.

CHAPTER 4

IMPROVED OPTICAL PROPERTIES OF InAs QUANTUM DOTS FOR INTERMEDIATE BAND SOLAR CELLS APPLICATIONS BY SUPPRESSION OF MISFIT STRAIN RELAXATION[*]

4.1. Introduction

The realization of electron confinement in nanostructures has triggered the development of novel optoelectronic devices. Quantum dots (QDs), made of a material with lower bandgap than the surrounding semiconductor, create three-dimensional potential wells that lead to carrier localization and discrete energy levels. Unlike quantum wells and quantum wires, the electronic states of the QDs are isolated from the conduction and valence bands with a zero density of states in between.[27] Using QD-based structures, single-electron transistors,[28–30] diode lasers,[31–34] and photodetectors[35] have been successfully developed and commercialized. Currently, there is much interest in the application of QDs for intermediate band solar cells.

The use of an intermediate band has been proposed for semiconductor solar cells in order to overcome the Shockley-Queisser limit[36] by increasing the photocurrent while preserving the output voltage of the matrix.[37] This concept may be achieved by introducing a sufficient number of states in the bandgap, which overlap in space creating an intermediate band. Such intermediate band allows two additional transition paths for light absorption, with a theoretical efficiency similar to a triple-junction solar cell connected in series.[38] The new transition paths are from the valence band to the intermediate band and from the intermediate band to the conduction band, corresponding to two additional sub-bandgaps. A detailed-balance model predicts optimum values of 1.96 eV for the main bandgap, and 1.24 eV and 0.72 eV for the sub-bandgaps, resulting in a photovoltaic efficiency of about 63% under maximum solar concentration.[39]

The InAs QD system has been explored for applications in intermediate band solar cells (IBSC), taking advantage from knowledge derived from other optoelectronic applications.[40,41] A high density of InAs quantum dots embedded in GaAs is expected to result in an intermediate band due to the overlap of the three-dimensional confined states.[42] A weakness in the InAs/GaAs system is in the experimentally determined bandgaps (1.2, 1.0, and 0.2 eV)[43] that differ from the ideal values (1.96, 1.24, and 0.72 eV). $Al_xGa_{1-x}As$ alloys have been used as a matrix to approach the optimum bandgap value.[2,42] $In_xGa_{1-x}As$ quantum dots with spherical symmetry,[42] as well as fully-strained lens-shaped InAs QDs,[2] have been reported to approach the optimum sub-bandgap

values.   An important aspect of InAs QDs in an (Al)GaAs matrix is the large

difference in lattice parameter between the QDs and the matrix. The lattice mismatch

is necessary for the formation of a two-dimensional *wetting layer* followed by island

(QD) growth, described by the *Stranski-Krastanov* growth mode.[11] However, the lattice

mismatch strain can be relaxed by the generation of misfit dislocations.[44–46] The

presence of dislocations can degrade the photocurrent in a QD photovoltaic device.[42]

In thin film epitaxy, plastic relaxation takes place after the film thickness reaches a

critical value.[22] The height (thickness) of the QD can be controlled using a thin capping

layer to partially cover the QDs, followed by a high temperature anneal.[47] This process,

known in molecular beam epitaxy as *indium flushing*, removes the top of the dots above

the capping level, converting the dots into disks of approximately equal height. The use

of this approach on InAs QDs grown on GaAs has been reported to result in superior

electric and optical properties.[48] More recently, InAs QDs on AlGaAs using a similar

approach have shown improved structure quality and optical response.[2]

In this chapter, we show the effect of the partial capping and annealing on the

morphology of the QDs grown by metalorganic vapor phase epitaxy (MOVPE).

Suppression of plastic relaxation due to the change of morphology is demonstrated. A

force balancing model is used to understand the relationship between plastic relaxation

and QD height. The optoelectronic properties of InAs QD-based thin film structures are

significantly improved by the suppression of plastic relaxation. The optoelectronic

properties are correlated with the morphology and the size of the QDs by calculated

optical transition energy as a function of QD diameter.

4.2. Experimental techniques

The InAs/AlGaAs QD structure was grown by MOVPE, in an Aixtron AIX 200 horizontal reactor at 100 mbar on n-doped (001) GaAs substrates, with a total hydrogen carrier gas flow of 8 l/min.[*] Tri-methyl aluminum (TMAl), tri-methyl gallium (TMGa), tri-methyl indium (TMIn) and arsine (AsH$_3$) precursors were used as Al, Ga, In, and As sources. CBr$_4$ and SiH$_4$ were used for p- and n-type doping. The Al/III gas phase was calibrated for the growth of Al$_{0.3}$Ga$_{0.7}$As layers, with a growth rate of 1 nm/s, V/III ratio of 14.9, while the growth rate of GaAs layers was 0.65 nm/s, the V/III ratio 23.3 and the growth temperature 630°C. The samples were subjected to the pre-growth treatment of de-oxidation at 720°C for 15 min with AsH$_3$ overpressure.

The growth sequence was as follows: A 500-nm-thick Si-doped (1×10^{18}cm^{-3}) n-GaAs buffer layer is grown at 630°C on the GaAs (001) substrate, followed by a 300-nm-thick n-type Si-doped (5×10^{17}cm^{-3}) and a 100-nm-thick undoped Al$_{0.3}$Ga$_{0.7}$As layers. The active region is composed of 10 layers of InAs QDs grown at 490°C, with a V/III ratio of 6.4, a growth time of 2.4 s and a growth rate of 0.14 nm/s. The dots are n-type doped using the same SiH$_4$ flow as was used to dope GaAs.   Before growth of the InAs QDs, the temperature is lowered to 490 °C with a ramping of ~ 4 min, keeping at that temperature during 1.5 min for surface stabilization. After the QD growth the

(*) The QD structures in this chapter were grown at the *Laboratorio de Semicondutores*, *Pontificia Universidade Católica do Rio de Janeiro*, Brazil.

temperature is maintained fixed for 12 s, and a GaAs capping layer is then grown at a constant temperature of 490 °C. The QDs were capped by either a 20-nm complete capping layer or a 5-nm partial capping layer. The temperature is then raised to 630 °C with a ramping time of 4 min followed by 1.5 min settling time for surface stabilization. Afterwards, a 90 nm $Al_{0.3}Ga_{0.7}As$ barrier is grown. Ten periods of the QDs, capping layer, and AlGaAs barrier were deposited to produce the active region in the device, shown schematically in Fig. 4.1(a). After the active region, the following layer sequence is deposited at 630 °C: a 100-nm-thick p-doped (5×10^{17} cm^{-3}) AlGaAs layer, a 200 nm p^+-AlGaAs window layer, and 30 nm thick p^+- GaAs (2×10^{18} cm^{-3}) contact layer. In the case of partial capping (Sample B), the indium atoms of the dots that exceed the capping layer height are spread from the top (Other reports for a similar process in molecular beam epitaxy call this approach the *indium-flush* method).

Cross-section samples were prepared for TEM by mechanical wedge polishing followed by argon-ion milling using a 2 kV accelerating voltage, at liquid N_2 temperatures. Two-beam diffraction contrast TEM was performed in a Philips CM 200 instrument to determine the nature of local strain variation. The morphology of the InAs dots was studied using high-angular annular dark-field (HAADF) imaging in an aberration-corrected JEOL ARM 200 instrument. The bright-field plan-view images of the QDs were taken using JEOL ARM 200 as well. Both instruments were operated at 200 kV.

Photoluminescence spectra were taken using a diode-pumped solid-state (DPSS)

laser operated at 532 nm. The laser power level was varied between 0.5 and 6.4 mW, with a beam radius of ~ 0.54 mm. A liquid N_2 cooled Ge detector was used to collect spectra from 800 to 1600 nm. The samples were held at low temperatures (~15K).

4.3. Results and discussion

4.3.1. Effect of partial capping and annealing on the morphology of the QDs

A diagram of the InAs/AlGaAs QD layer structure used in this study is shown in Fig. 4.1(a). It consists of 10 layers of InAs QDs covered by GaAs capping layers in an $Al_{0.3}Ga_{0.7}As$ matrix, with *p*-type and *n*-type GaAs layers at the two ends. The QD structures were grown by metalorganic vapor phase epitaxy. The InAs QDs were grown at 490 ºC, following the *Stranski-Krastanov* growth model. The QDs were capped by either a 5 or 20-nm-thick GaAs layer at 490 ºC, followed by temperature ramping to 630 ºC. The temperature was then kept at 630 ºC for 1.5 min before the subsequent growth of the 90-nm-thick $Al_{0.3}Ga_{0.7}As$ barrier. QDs capped by 20 nm capping layer were fully covered and protected at 630 ºC. In contrast, a 5 nm capping layer partially covered the QDs and the indium atoms in the exposed region are spread out at 630 ºC

The morphology of the InAs dots was visualized using high-angle annular dark-field (HAADF) electron microscopy.[25] The images were produced under axial illumination by scanning a 200 keV electron beam over the area of interest, and collecting the transmitted electrons that are scattered into high angles (90 to 150 mrad). Since the angle of scattering depends on the atomic number, the contrast in HAADF images is closely related to the local chemical content.   Figures 4.1(b) and 1(c) show

31

HAADF images of two layers of QDs and a specific QD in sample A (top images) and

in sample B (bottom images). For sample A, the QDs are lens shaped and most of

them are fully covered by the 20-nm-thick GaAs capping layer as highlighted. The

annealing step did not change the morphology of the dots due to the protecting capping

layer. For sample B, the dots are flat with a uniform height as a result of truncation of

the top portion, except for those dots small enough to be fully covered by the 5-nm-

thick capping layer.
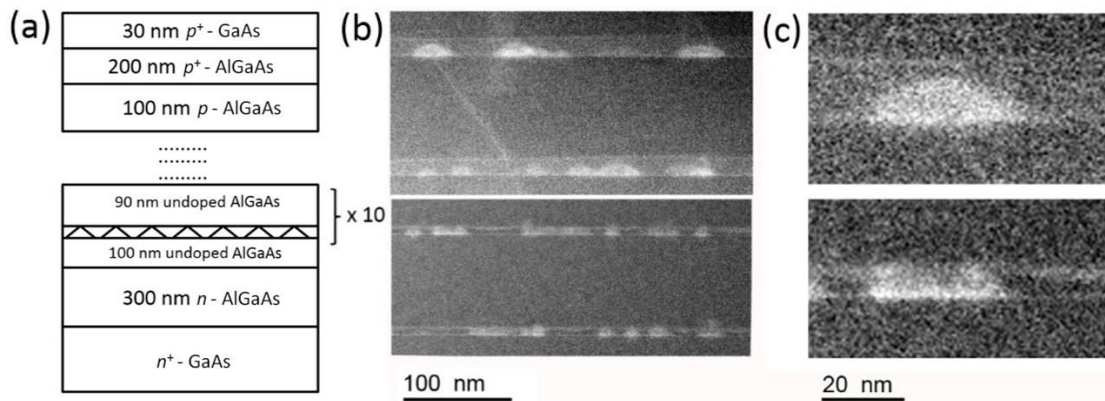
Figure 4.1. The QDs structure. (a) Schematic diagram of the structure of the sample consisting of 10 periods of InAs QDs on $Al_{0.3}Ga_{0.7}As$. (b) Cross-section high-angle annular dark-field TEM images of sample A (top image, 20 nm capping layer) and sample B (bottom image, 5 nm capping layer). (c) Images at higher magnification showing the shape of QDs in sample A (top image) and sample B (bottom image). Bright contrast in these images corresponds to higher average atomic numbers.

A detailed study of the morphology of the QDs truncated by the partial capping

and annealing step are shown in Figure 4.2. Figure 4.2(a) is a HAADF cross-section

image of the QD layered structure, taken along a <110> projection. Each QD layer is

defined by the presence of indium-rich layers on both sides of the GaAs capping layer.

The lower layer corresponds to the InAs wetting layer associated with the Stranski-Krastanov growth mode, while the upper layer is an indium-rich layer that results from the lateral migration of indium during the thermal annealing step. The top layer is less sharp than the wetting layer, probably due to diffusion at the high temperature annealing that produced it. This layer has not been observed in QD structures grown by MBE with *indium-flush*, perhaps because indium re-evaporates at high temperatures in vacuum.[47] After the thermal annealing step, the InAs QDs that were partially capped develop into truncated-lens-shape dots (Fig. 4.2(b)). The larger dots have the appearance of spools, where the central disk has a uniform height of ~ 5 nm. Figure 4.2(c) is a high-resolution HAADF image of one such dot, with a central disk bound by the top and bottom In-rich layers. The base of the QD reflects the original morphology since it was protected by the capping layer. The broadening near the top is due to the indium migration on the surface and possibly diffusion into the GaAs capping layer.
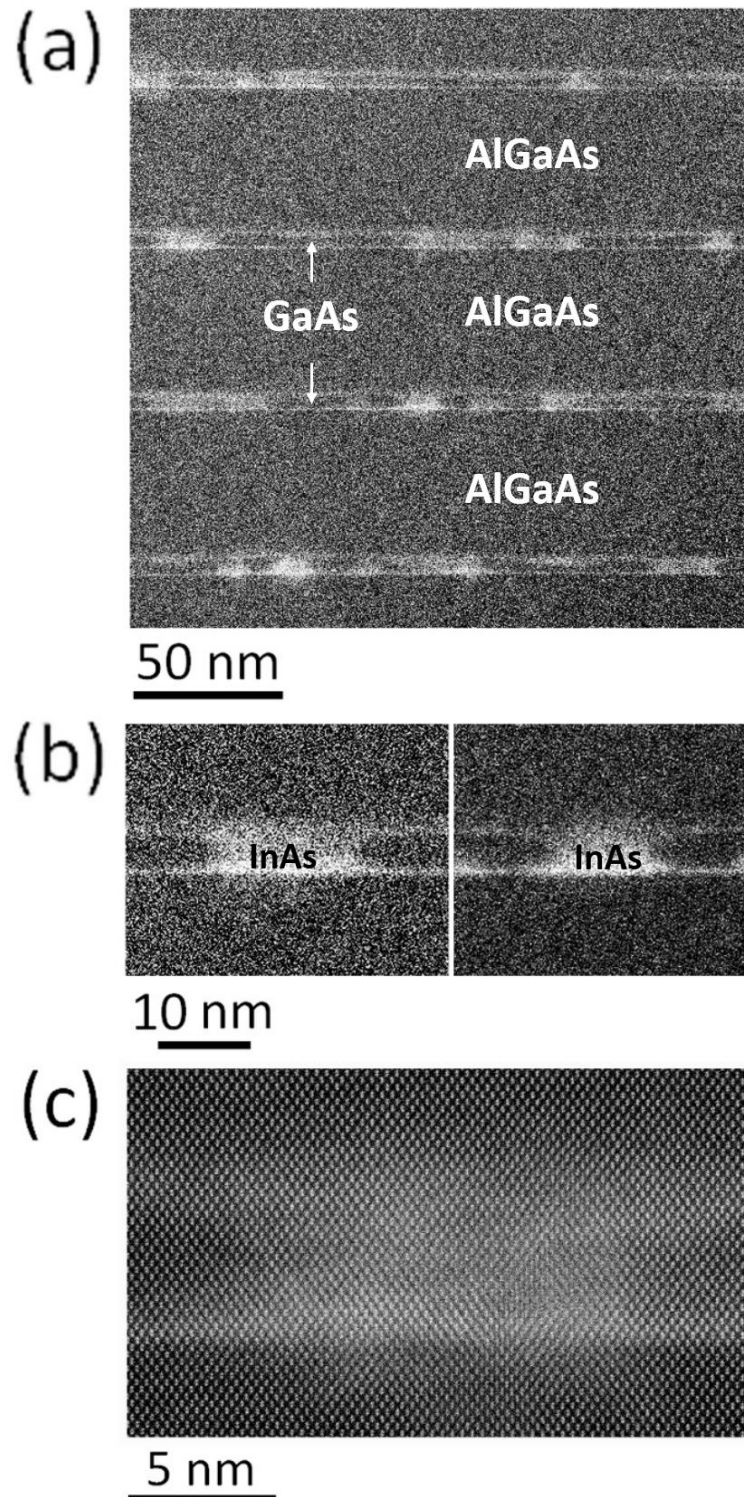
Figure 4.2. Cross-section HAADF images of the InAs QD layered thin film structure. (a) Image of four QD layers of the 5-layer structure. (b) Magnified view of two QDs truncated as a result of partial capping and annealing step. (c) Lattice image of one truncated QD.

Though the height of the spool-shaped QDs has been reduced to a uniform value

during the annealing step, the lateral size distribution of the spool-shaped QDs remains and can be determined from plan-view TEM imaging. Figure 4.3(a) is a bright-field image of the top QD layer, showing a QD density of ~10^{10} cm^{-2}. The QDs exhibit an Ashby-Brown contrast, reflecting unrelaxed coherent strain distribution.[49] The size distribution of 189 QDs (97 in Fig. 2(a)) is shown in Figure 4.3(b). The lateral sizes show a unimodal asymmetric distribution with a maximum diameter between 6 and 9 nm, which can be fitted well with a lognormal distribution curve.[50]
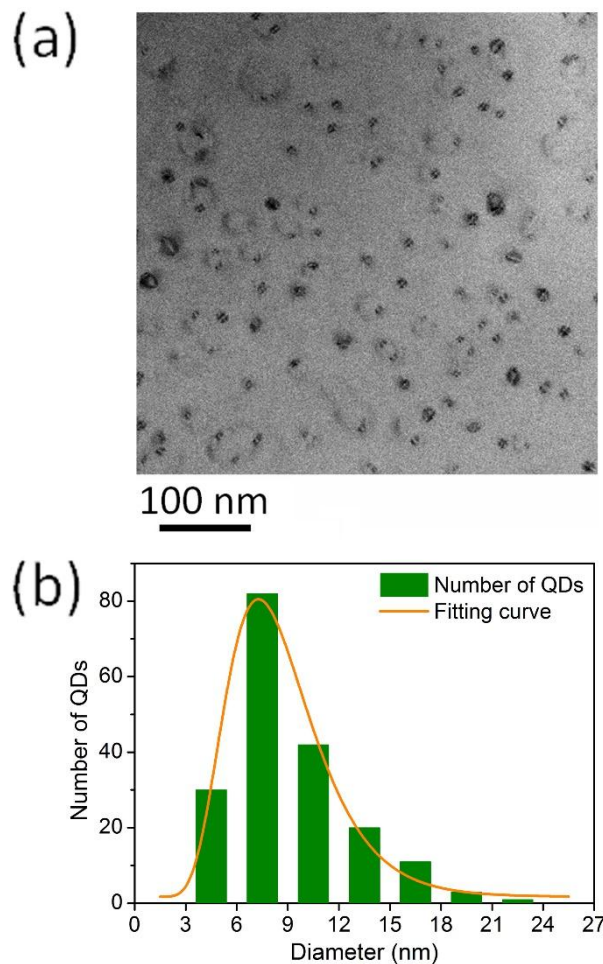
Figure 4.3. Size distribution in a single QD layer. (a) Plan-view bright-field TEM image. (b) Lateral size distribution extracted from the plan-view image. Binning size is 3 nm.

4.3.2. Suppression of misfit strain relaxation

A large difference in the microstructure resulting from the capping-plus-anneal step was observed by TEM. Threading dislocations were observed associated with QDs with a capping thickness of 20-nm (sample A) but not for capping thickness of 5-nm (sample B). The microstructure of the film in sample A is shown in the two-beam diffraction contrast image in Fig. 4.4(a), which is a cross-section view along the $[110]$ projection, taken under diffraction contrast with $\boldsymbol{g} = \bar{2}20$ (Bragg diffraction by the $(\bar{2}20)$ planes). It shows dislocations emanating from some of the dots, forming a V-shape pattern with branches lying on $(1\bar{1}1)$ and $(\bar{1}11)$ planes; similar patterns have been reported in the literature.[51] The dislocations in Fig. 4.2(a) show dark contrast under $\boldsymbol{g} = \bar{2}20$ meaning that the burgers vectors have an edge component along $[\bar{1}10]$. Thus, the segments of the dislocations lying on the (001) plane of the InAs/AlGaAs interface have an edge component that relaxes the misfit strain in a given QD. The microstructure of sample B is shown in Fig. 4.4(b). The two-beam diffraction contrast image shows no evidence of threading dislocations, suggesting coherently strained QDs embedded in the matrix.
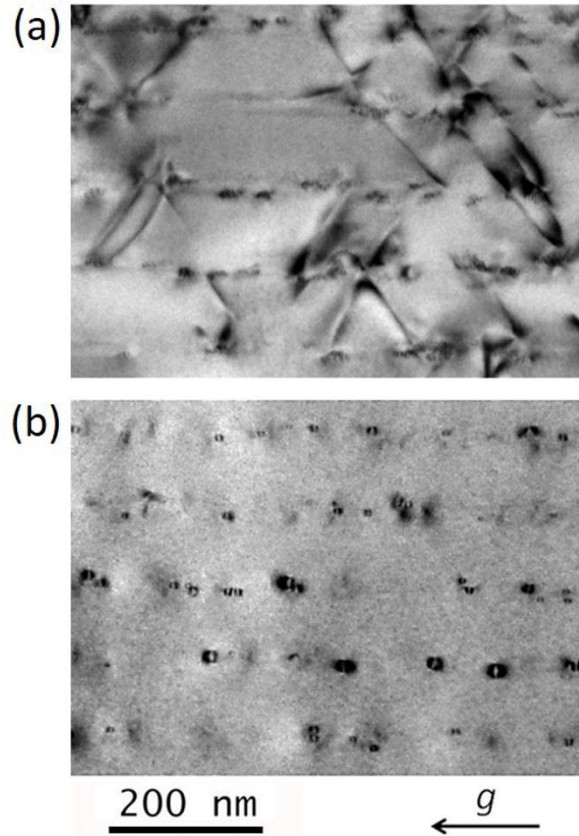
Figure 4.4. Two-beam diffraction contrast TEM images of the QD region in (a) sample A and (b) sample B, taken under $g = \bar{2}20$ condition. Threading dislocations are observed in sample A.

At higher magnification, the QDs in sample A (Fig. 4.5(a)) show moiré fringes perpendicular to the diffraction vector g caused by the overlap along the electron beam projection of the InAs dots with the surrounding lattice.[52] The moiré fringes imply strain relaxation in the QDs, with loss of coherence due to the presence of misfit dislocations. The image at higher magnification for sample B (Fig. 4.5(b)) shows that for each QD two lobes of dark contrast with a bright region in the middle (perpendicular to g). This is also known as Ashby-Brown contrast, which is typical for coherent precipitates where bending of crystal planes is produced by elastic strain.[49]

37
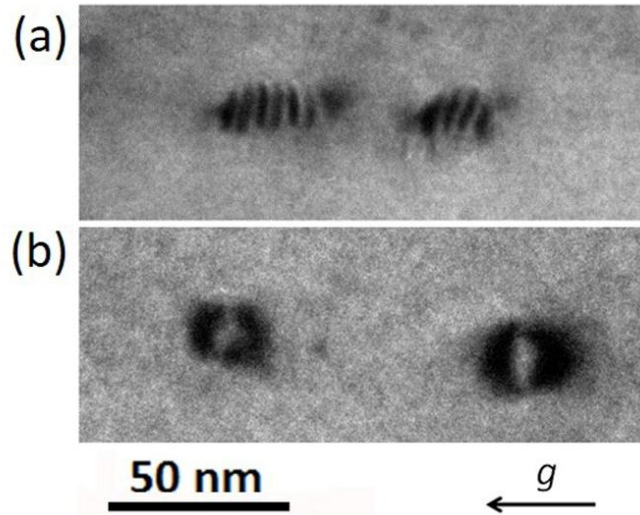
Figure 4.5. Two-beam diffraction contrast TEM images of QDs in (a) sample A and (b) sample B, under $g = \bar{2}20$ condition. The QDs in sample A exhibit moiré fringes. The QDs in sample B show Ashby-Brown contrast.

High-resolution HAADF images of two InAs QDs are shown in Fig. 4.6. The smaller QD (Fig. 4.6(a)) does not show dislocation loops, indicating a fully strained state. On the other hand, a larger dot (6 nm high, in Fig. 4.6(b)) has misfit dislocations characterized by planes ending at the QD boundary. Models of the coherently-strained QD and the relaxed QD are shown below each HAADF image. For the relaxed dot, 60° and Lomer dislocations and a threading dislocation are labeled. The former are misfit dislocation loops that surround the dot and appear as dislocation dipoles in the cross-section. The latter is associated with a dislocation that failed to form a loop.
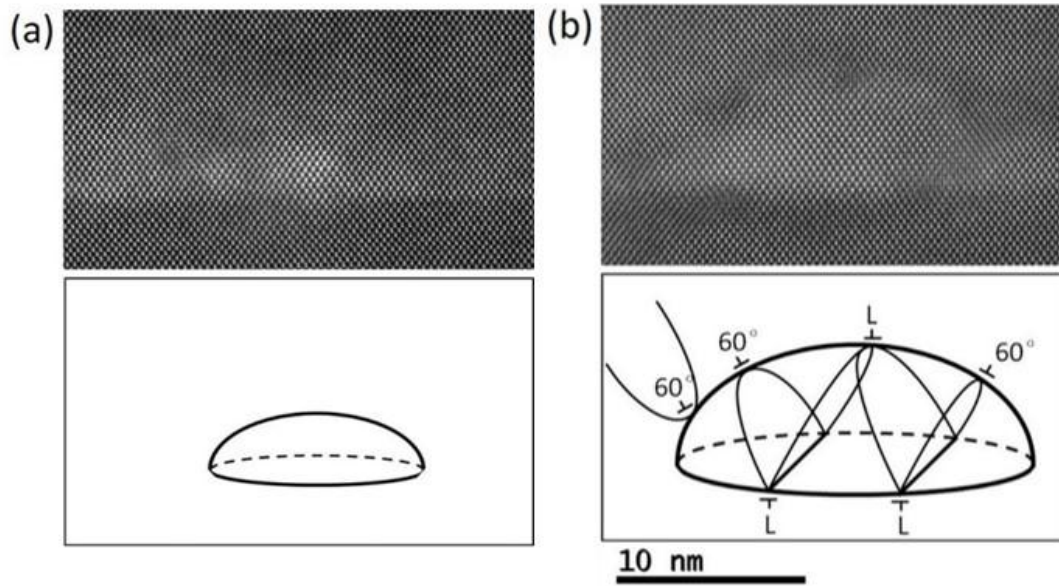
Figure 4.6. High-resolution HAADF images show the atomic arrangement of (a) 3 nm and (b) 6 nm thick InAs dots, viewed in the [110] projection. Schematic diagrams below each image show the arrangement of dislocations around the QD.

To understand the misfit strain relaxation in an InAs QD, we consider the forces acting on a misfit dislocation loop surrounding the dot. One force is due to the misfit strain promoting the presence of misfit dislocations and another is the dislocation loop line tension attempting to minimize the total length of the misfit dislocations. We approximate the problem by considering the InAs QD as a disk with two surfaces parallel to the growth plane, with the disk height determined by the capping layer thickness, and the disk diameter much larger than its height. Parallel segments of the dislocation loops surrounding the disks form dipoles (i.e. dislocations with equal but opposite Burgers vectors). The segments lying on the top and bottom interfaces exert an attractive force on each other.[21] We use the model developed by Fischer et al.[53] to calculate the critical separation (QD height) at which the two forces are equal in magnitude. The model deals with the relaxation of strained layers using an

equilibrium approach that includes the elastic interaction of dislocation dipoles. In the original model, the dipole consists of a real dislocation at a heterointerface plus an image dislocation across a free surface. This method has been used to correctly predict the critical thickness for strained GeSi films on silicon.[53] We use the same approach to determine the critical thickness for a double heterointerface associated with a buried InAs disk.

Figure 4.7(a) shows the alignment of 60-degree dislocation pairs separated by a distance h, forming a dislocation dipole. The critical separation below which the dislocation dipole loop collapses, h_c, is calculated as a function of lattice mismatch using the excess shear stress given by the equation[53]

$$\tau_{exc} = cos\lambda \, cos\phi \left[\frac{2G(1+v)}{(1-v)}\right]\{\varepsilon - [b \, cos\lambda/(2R_{h,p})](1+\beta)\} \tag{4.1}$$
$$= 0$$

with

$$\beta = \{[1-(v/4)]/[4\pi \, cos^2\lambda \, (1+v)]\}ln(R_{h,p}/b) \tag{4.2}$$

$$R_{h,p} = \left(\frac{4}{h^2}+\frac{4}{p^2}\right)^{-1/2} \tag{4.3}$$

where $\lambda = 60°$ is the angle between the Burgers vector and the direction in the interface, normal to the dislocation line, $\phi = 35.3°$ is the angle between the slip plane and the strained interface normal, G is the shear modulus, $v = 0.35$ is the Poisson ratio,[54] h is the vertical separation between the two segments of the dislocation dipole, and p is the lateral separation between two dislocations. The magnitude of the

Burgers vector of a 60° dislocation in InAs is $b = a/\sqrt{2} = 0.428$ nm.[55] Note that h in the Eq. (4.3) represents the distance between dislocations in the dipole, while in the original Fischer's equation it represents half that value.

In Fig. 4.7(b), the solid and dashed curves show hc for the cases of one dislocation $(p \to +\infty)$ and of a dislocation array with full strain relaxation $\left(p = a_{InAs}\,a_{GaAs}/(a_{InAs} - a_{GaAs})\right)$. Considering the lattice parameters for InAs (0.6058 nm) and GaAs (0.5654 nm),32 a value for p = 8.5 nm is obtained. The critical thickness for InAs/AlGaAs QDs is predicted to be 4 nm by the model. This is in agreement with TEM observation which shows that the transition from strained to relaxed QDs occurs at a height of about 6 nm. This explains the suppression of strain relaxation in the QDs whose height is limited to 5 nm which is below the critical thickness.
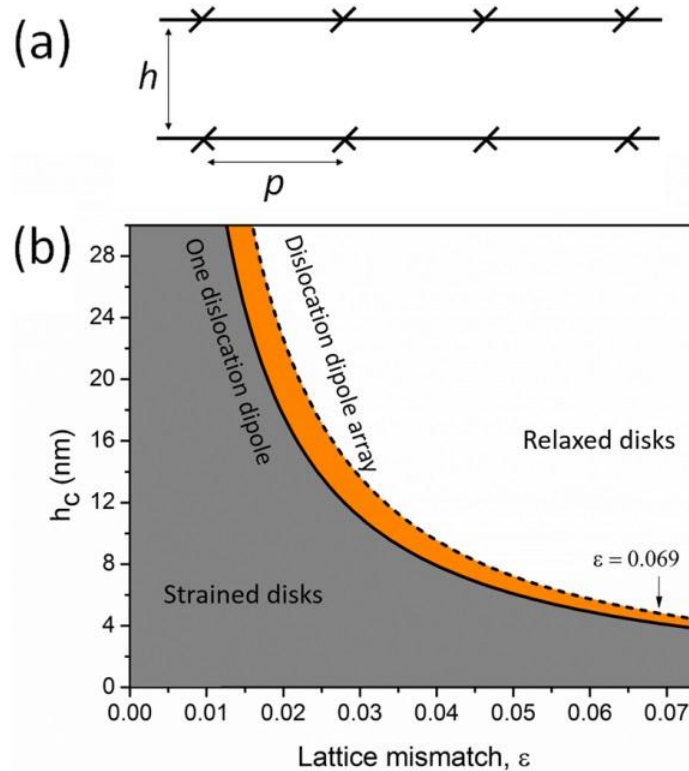
Figure 4.7. A Critical Thickness Model for Generation of Misfit Dislocations. (a) Schematic diagram of simplified model used to determine the critical thickness. (b) Equilibrium force calculation of the critical thickness as a function of lattice mismatch, for a single dislocation dipole and for a periodic array of dislocation dipoles.

4.3.3. Effects of suppression of misfit strain relaxation on optical properties

The influence of plastic relaxation on optical transitions is observed in the photoluminescence spectra of samples A and B in Fig. 4.8.[*] The emission peak at 1.49 eV is from the GaAs capping layer, which because of the presence of the dislocations induced by plastic relaxation, the peak value in sample A is ~ 60% lower than in sample B. We attribute the emission at ~ 1.46 eV to the InAs wetting layer, which is identical in both samples. In sample A, an In-rich layer is present on top of the GaAs capping

(*) The photoluminescence measurement was done by Dr. Alec Fischer and Mr. Hangxiao Liu at Arizona State University, Tempe, Arizona, USA.

layer (Figs. 4.1(b) and (c), top images), which we attribute to trapping of the indium segregated during growth of the GaAs capping layer,[56] blocked by the AlGaAs barrier.[57] We assign the 1.43 eV emission to this layer.   In sample B, the top of the InAs dots is spread over by the annealing step, forming the In-rich layer on top of the GaAs capping layer (see Figs. 4.1(b) and (c), bottom images).   This layer is thicker than in sample A, and emits at 1.39 eV. A strong emission is observed in the 1.181 to 1.363 eV range for sample B, which lacks dislocations, and present uniform dot height caused by the annealing step. No such emission is observed in Sample A, which we attribute to dislocation acting as non-radiative recombination centers. Indeed, the PL data, where sample B exhibits better optical properties with a stronger emission corresponding to the QDs transitions, shows that high-efficiency QD nanostructure for intermediate band solar cells can be achieved with suppression of the misfit-strain relaxation in InAs QDs and lead to the desired intermediate band.
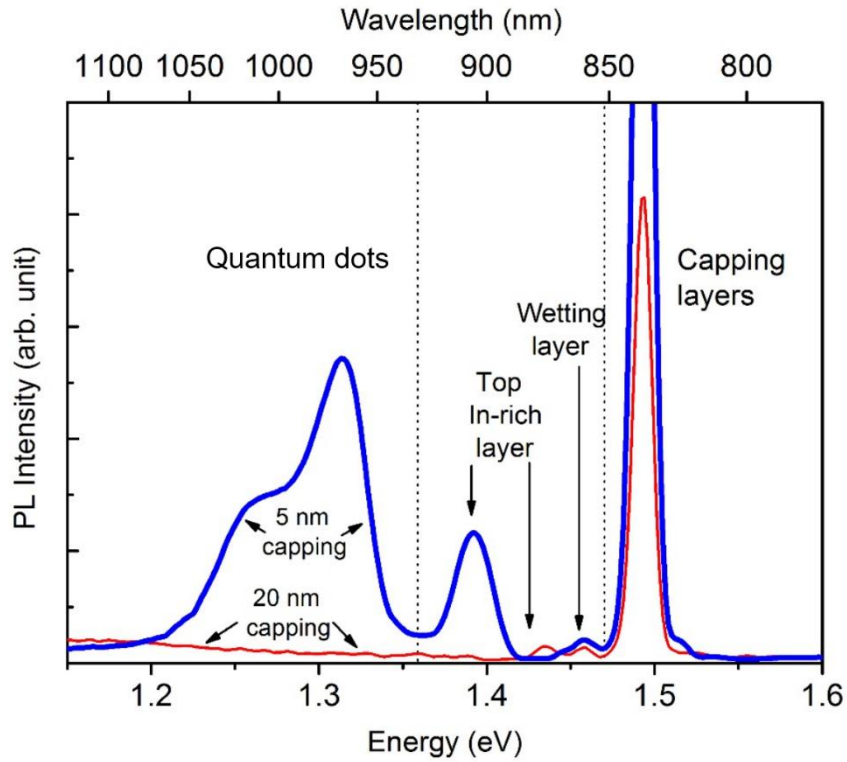
Figure 4.8. Photoluminescence spectra for relaxed QDs (sample A) and for strained QDs (sample B).

4.3.4. A detailed study of the optical properties of the truncated QDs

Figure 4.9 shows the photoluminescence spectrum of the QD structure at 15 K fitted by two Gaussian functions. The fitting curve reproduce the QD emission well, except for the low-energy tail. The QD emission shows energy levels close to the optimum values for transitions between the intermediate band and the valence band (1.24 eV).
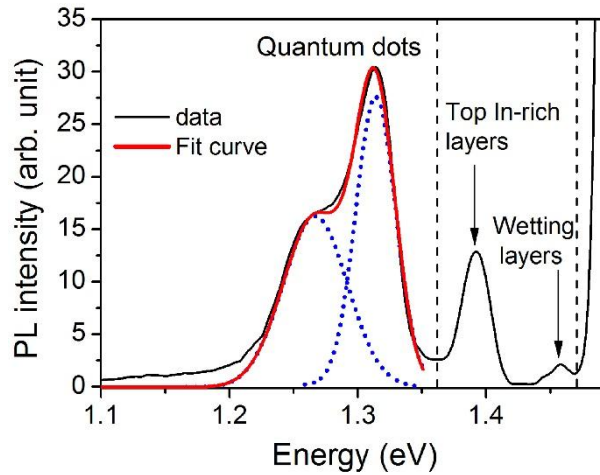
Figure 4.9. Photoluminescence spectrum from the InAs layered structure. Two Gaussian peaks are used to fit the emission from the QDs.

To establish the origin of the double-peak emission, we have studied the excitation power dependence of the luminescence. The spectra for excitation power in the range from 0.5 mW to 6.4 mW, taken at 15 K, are shown in Fig. 4.10(a). Two Gaussian peaks were used to fit each spectrum. The resulting peak maxima do not change significantly with excitation power. The integrated intensity of each Gaussian peak and the ratio of the intensity of the second peak to the first peak are plotted in Fig. 4.10(b). This increase in the ratio with excitation power has been observed in InAs QDs and has been associated with the population of excited states.[58]
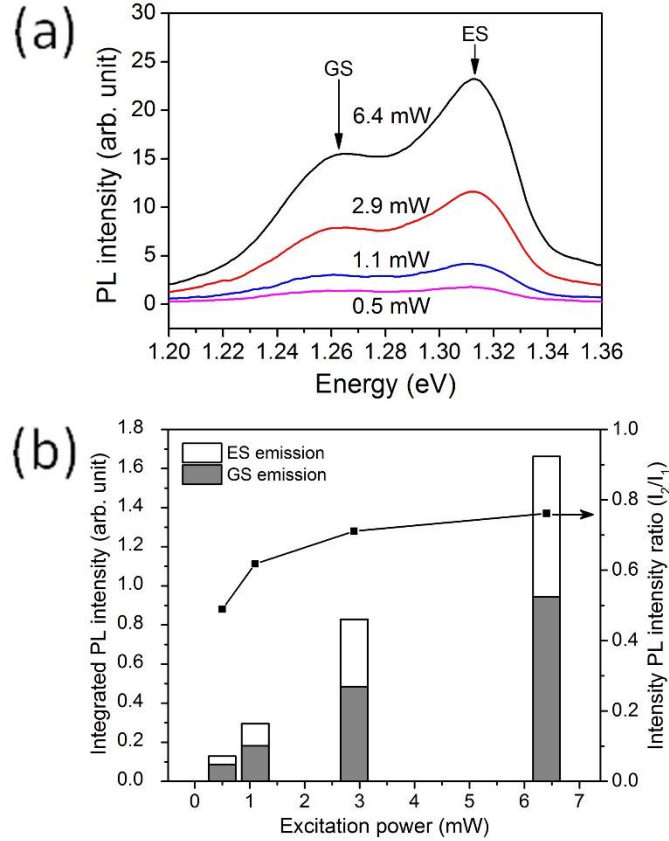
Figure 4.10. Excitation power dependence of the photoluminescence characteristics. (a) PL spectra of the QD layer emission at different excitation powers. (b) Integrated intensity of the two Gaussian peaks as a function of the excitation power. The ratio of the integrated intensity of the second peak to the first peak is also shown.

The temperature dependence of the photoluminescence is shown in Fig. 4.11(a). The intensity of the two QD emission peaks decreases with increasing temperature, reportedly due to increasing non-radiative recombination.[59] The relative intensity of the excited-state transition with respect to the ground-state transition decreases with temperature (Fig. 4.11(b)). We interpret this to be due to the excited levels of the QDs being close in value to the energy levels in the In-rich layer, which allows carrier escape by thermal excitation.[3] For smaller QDs that are covered with GaAs, the spatial proximity of the In-rich layer also facilitates carrier escape by reducing the potential

barrier width for thermal escape.
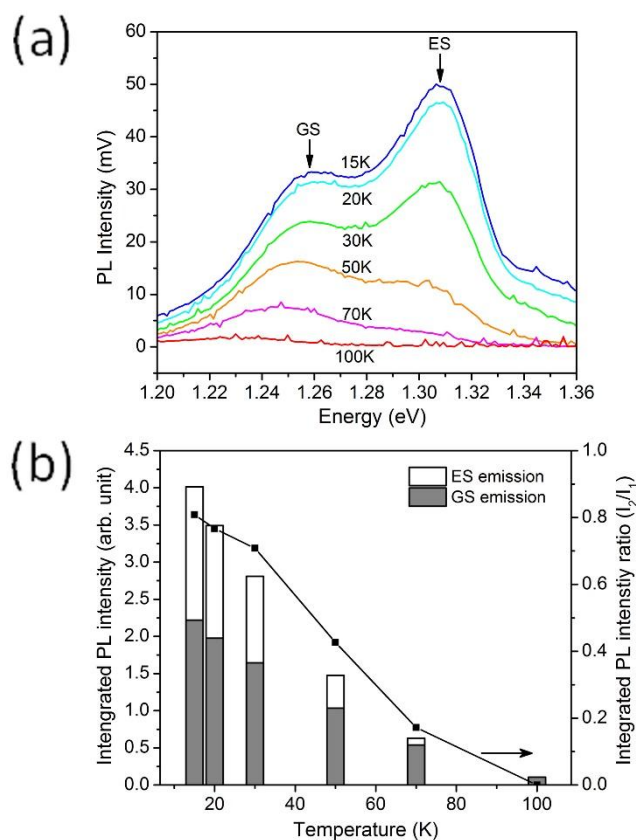
Figure 4.11. Temperature dependence of the photoluminescence characteristics. (a) PL spectra of the QD layer emission at different temperatures. (b) Integrated intensity of the two Gaussian peaks as a function of the temperature. The ratio of the integrated intensity of the second peak to the first peak is also shown.

4.3.5. Correlation of optical properties and the morphology of truncated QDs

A single QD has well defined energy levels and emits at specific wavelengths,[60] but the emission from an ensemble of QDs is usually broader than a single QD due to inhomogeneities in size, shape, content, and strain.[61]

Here the broadening is believed to be related to size inhomogeneity that is mostly associated with the variation of the lateral dimension of the QDs with relatively uniform heights as a result of the partial capping and annealing (section 4.3.1). Calculated

optical transition energies establish a close correlation between the optical properties and the lateral size distribution. The optical transition energies for disk-shaped QDs have been calculated as a function of the disk diameter, using a Schrödinger equation solver based on the split-operator method in the three-dimensional effective mass approximation model.[62,*] The interband transition energies are between electron and hole states with the same quantum number and symmetry, as allowed by selection rules.[63] In our model, the InAs disks are on a 0.6 nm InAs wetting layer, surrounded by GaAs capping layer of the same height as the disk, and otherwise embedded in $Al_{0.3}Ga_{0.7}As$ barriers. The calculations for disk with heights of 4.0, 4.5 and 5.0 nm, are shown in Fig. 4.12. The transition energies for large QDs are depicted by the lower curves corresponding to the 5-nm-high disks. Smaller QDs are lower in height, and their transition energies are better described by the upper curves corresponding to 4-nm-high disks. The electronic transition range observed in the PL spectra for ground-state transitions are shown in the lower left box; and for excited-state transitions in the upper right box inside Fig. 4.12. The respective peak maxima are marked by dash lines inside the boxes. This simplified model closely depicts the transitions observed in the PL spectrum in Fig. 4.9, and the corresponding QD diameter distribution observed by TEM in Fig. 4.3(b).

(*) The calculations were done by Mr. Guilherme Torelly and Dr. Roberto Jakomin at *Laboratório de Semicondutores, Pontifícia Universidade Católica do Rio de Janeiro*, Brazil.

The first and second emission peaks are associated with ground-state and excited-state emissions of QDs with different diameters. The first peak ranges from 1.1 eV to 1.34 eV corresponds to ground-state emission of QDs with diameters from 6 to 15 nm. The peak maximum at 1.27eV matches the most common diameter at ~ 8 nm. The tail on the low energy side of the first emission peak is due to the residual large QD tail observed in the size distribution. The second emission peak starts at ~ 1.25 eV, which corresponds to the excited-state emission of QD with a diameter of 15 nm. But this peak ends at 1.36 eV corresponding to a disk diameter of 12 nm and the peak maximum happens at 1.31 eV corresponding to a disk diameter of 13 nm, which does not match the diameter distribution as well as the first emission peak. This is attributed to the indium-rich layers that are not included in the calculation. Given that the energy levels of the adjacent indium-rich layers are ~ 1.39 eV, we speculate that the carriers on the excited-levels of the small QDs can escape from the QDs and redistribute through the indium-rich layers to lower energy levels of larger QDs, which cuts off the emission at high energy and red-shifts the peak maximum. The easy escape of carriers through the In-rich layers should lead to a reduced recombination rate (which is high in QDs), improving the figures of merit for intermediate-band solar cells.
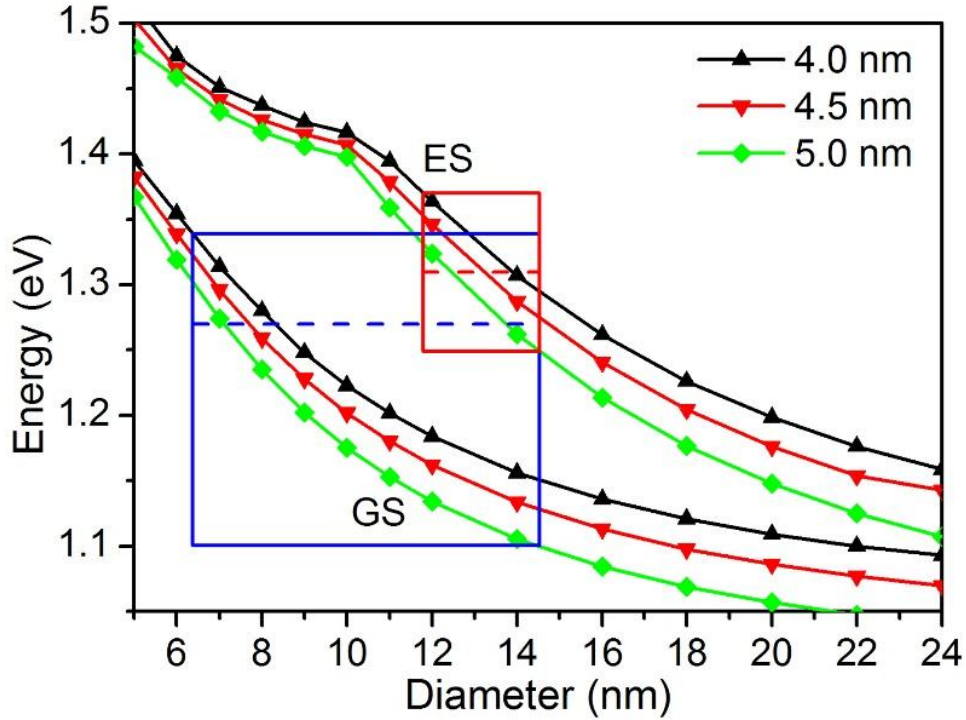
Figure 4.12. Calculated transition energies for disk-shape QDs with a height of 4, 4.5 or 5 nm as a function of disk diameter.

4.4. Conclusions

We have shown that the transition from relaxed to strained QDs grown by MOVPE can be controlled by partial capping followed by annealing at higher temperatures. We have successfully suppressed plastic strain relaxation in InAs dots by depositing a 5-nm-thick capping layer followed by annealing, which controls the height of the InAs dots below the critical value for dislocation generation. The suppression of plastic strain relaxation in the InAs dots is confirmed by the presence of moiré fringes for the relaxed dots and Ashby-Brown contrast for the strained dots. The experimental observations and the calculation of the critical height are in good agreement, indicating the interplay between strain and dislocation line tension. We have found direct evidence that InAs/Al$_{0.3}$Ga$_{0.7}$As is strongly affected by the presence of defects associated with plastic

relaxation. The suppression of plastic strain relaxation by the control of QD height generates effective gap states for application to optoelectronic devices. This is particularly useful for intermediate band solar cells in order to overcome the standard solar cell efficiency limit, and achieving improved harvesting of light for energy conversion.

The lateral sizes of the QDs truncated by partial capping and annealing have a unimodal distribution with a maximum value between 6 and 9 nm. The QDs are observed to be sandwiched by a lower wetting layers and an upper In-rich thin layer. The PL spectrum show ground-state emission and excited-state emission from QDs and emission from the In-rich layers. Thermal carrier escape from the QDs was seen with increasing temperature. Temperature-dependent photoluminescence indicates that carriers on the excited states have a higher tendency to escape under thermal excitation. The In-rich layer facilitates the carrier redistribution among the excited states of QDs leading to a narrower excited-state emission peak.

CHAPTER 5

CHARACTERIZATION OF $In_xGa_{1-x}N$ THICK FILMS (x ≤ 0.15) GROWN BY

MOCVD FOR PHOTOVOLTAIC APPLICATIONS

5.1. Introduction

$In_xGa_{1-x}N$ has a direct bandgap which can be engineered over a wide range between

0.7 to 3.4 eV,[1] making the material a perfect candidate for light-emitting, lasing and

photovoltaic application.[64] $In_xGa_{1-x}N$ multiple quantum wells consisting of several-

nanometer-thick $In_xGa_{1-x}N$ layers sandwiched by low $In_xGa_{1-x}N$ layers are used in light

emitting diodes (LEDs)[65,66] and laser diodes[67,68]. In solar cell applications, single-

junction solar cells have an energy efficiency limit of ~ 33% (Shockley–Queisser

limit)[36] due to losses associated with low-energy photons and thermalization of hot

carriers. Integration of multiple bandgaps in a solar cell diminishes the energy loss and

thus overcomes the Shockley–Queisser limit. The wide bandgap range of InGaN alloys

is utilized for fabrication of solar cells with high energy-conversion efficiency.

Compared with LED and laser structures, solar cells require thick $In_xGa_{1-x}N$ films

(thicker than 100 nm) in order to absorb a significant amount of solar radiation.[69,70]

The growth of good quality GaN thin films requires growth temperatures higher

than 1000°C for efficient cracking of NH_3. The In-N bonding being thermally less stable

than Ga-N bonding tends to break at such high temperatures. For that reason, the growth

temperature of InN is usually below 900°C at the expense of inefficient breaking of the

NH_3 bonds. On the other hand, at low temperatures liquid indium has an equilibrium

52

vapor pressure close to InN, which leads to a tendency to form indium droplets.[71] Therefore the temperature window for growth of $In_xGa_{1-x}N$ quality is narrow.

$In_xGa_{1-x}N$ films are usually grown on GaN templates on sapphire substrates. From the lattice point of view, $In_xGa_{1-x}N$ films and GaN templates are both wurtzite structure but with a lattice mismatch up to 10.7%. Such large lattice mismatch can trigger plastic relaxation in the epitaxial $In_xGa_{1-x}N$ films. In the most common c-plane epitaxy, the primary (0001) slip system is not active under the biaxial misfit strain due to the absence of a driving force. Several kinds of defects may develop in the strained films, some of which realize strain relaxation either locally or on a large scale. The threading dislocations from the GaN template layer bend towards the $In_xGa_{1-x}N$/GaN interface due to the interaction between the dislocations and the misfit strain in the film.[14] The secondary $\{11\bar{2}2\}\langle11\bar{2}3\rangle$ slip systems have been reports to be responsible for the formation of misfit dislocations.[72]

In this chapter, results of the study of the structural and optical properties of $In_xGa_{1-x}N$ films with $0.07 \leq x \leq 0.15$ are presented. For low indium contents the $In_xGa_{1-x}N$ films grow pseudomorphically strained. Dislocation clusters resembling *baskets* are observed at x ~ 0.07 and 0.12. At x ~ 0.15, a misfit dislocation arrays are observed that extend over large regions. The properties of each kind of defects will be discussed. The less reported dislocation clusters consist of a-type edge dislocations that cause local strain relaxation and the incorporation of additional indium, with local luminescence indicating lower bandgaps. We argue that the origin of the dislocations clusters is

associated with the formation of lagoons of indium metal which lead to lateral overgrowth, of higher indium content $In_xGa_{1-x}N$. The a-type dislocations threading from the baskets provide a transition from the relaxed region to the surrounding strained film.

5.2. Experimental details

Three $In_xGa_{1-x}N$ films were grown by MOCVD at temperatures at 790, 760 and 721 °C, resulting in indium contents of 7, 12 and 15%, as estimated by x-ray diffraction. The surfaces of the films were inspected by AFM.[*]

The TEM samples were made by mechanical polishing followed by ion milling using a 3.7 keV Ar^{2+} beam at liquid nitrogen temperatures. The samples were cleaned using a 2.0 keV Ar^{2+} beam before TEM observation. The TEM images were taken in a Titan 80/300 transmission electron microscope (TEM) using a 300-keV electron beam. The large-angle convergent-beam electron diffraction (LACBED) was done in a JEOL 2010F TEM operating at 200 keV.

The optical properties were measured by cathodoluminescence (CL) in a scanning electron microscope with an acceleration voltage of 5 kV and a beam current of 400 pA. Monochromatic CL images were obtained by fixing the grating in the spectrometer at specific wavelengths. The light emission intensity was measured using a GaAs

---

(*) The epitaxial growth, and the XRD and AFM analysis of the InGaN films were performed at Photonitride Inc., Tempe, Arizona, USA.

photomultiplier detector.[*]

5.3. Results and discussion

5.3.1. Microstructures of $In_xGa_{1-x}N$ films with $0.07 \leq x \leq 0.15$

Dislocations threading up from the GaN/sapphire interface and through the $In_xGa_{1-x}N$ film were observed in all the three samples. In addition to the threading dislocations from the layer below, new defects form in the $In_xGa_{1-x}N$ films due to lattice mismatch. Both GaN and InN have the wrutzite structure with lattice parameters on the basal plane of 3.19 Å and 3.54Å, which results in a significant lattice mismatch (that follows Vegard's Law) when $In_xGa_{1-x}N$ is grown epitaxially on (0001) GaN, as shown in Fig. 5.1. The variation of the bandgap of the $In_xGa_{1-x}N$ films is also plotted in Fig. 5.1 on the right y-axis assuming a bowing parameter of 2. The lattice mismatch between the GaN template and the $In_xGa_{1-x}N$ epilayer with x = 0.07, 0.12 and x = 0.15 are 0.77%, 1.31% and 1.64%, respectively.
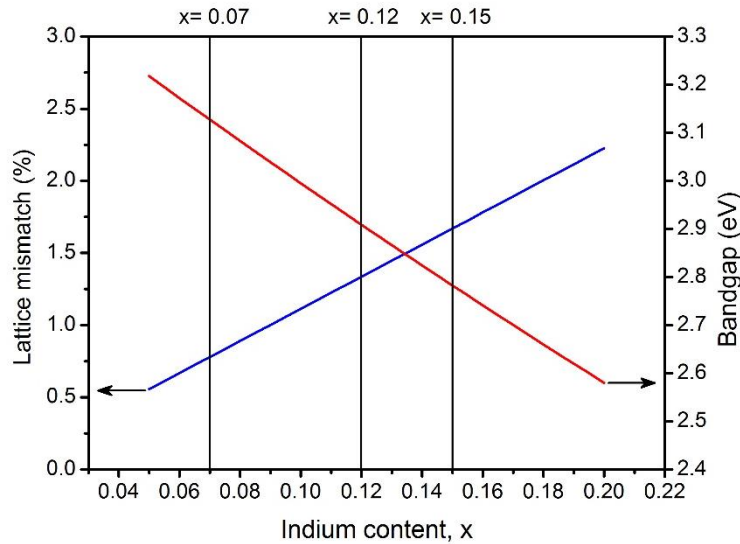
Figure 5.1. Lattice mismatch and bandgap of $In_xGa_{1-x}N$ films grown epitaxially on GaN as a function of indium content. The lattice parameter variation with indium composition follows Vegard's law.

For the $In_xGa_{1-x}N$ film with x = 0.07, the TEM two-beam diffraction-contrast bright-field plan-view image in Fig. 5.2(a) shows several dislocations forming a cluster surrounding a circular region These dislocations are inclined indicated by the alternating bright/dark contrast along each dislocation. The sample was tilted away from exact $[0001]$ zone axis towards a $\boldsymbol{g} = 11\bar{2}0$ condition. This type of dislocation clusters resembles baskets when viewed in cross-section (Fig. 5.2(b)). The dislocation cluster does not connect to any dislocation from the GaN template. About ten dislocations are counted in the specific dislocation cluster which is ~ 330 nm in diameter shown in the plan-view image (Fig. 5.2(a)). Another such dislocation cluster is captured in the cross-section TEM image Fig. 5.2(b) having similar dimensions. A threading dislocation from the template layer is also observed in the cross-section image. In the plan-view image, the single dislocations were categorize as threading dislocation

from the template layer with their threading part in the template layer removed during

the sample preparation thinning step.
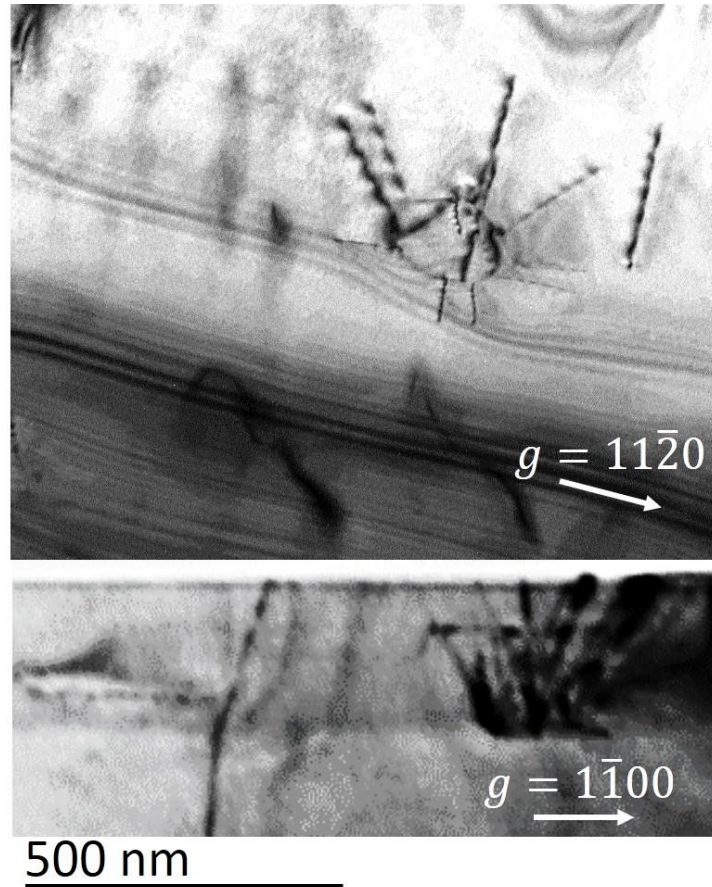
Figure 5.2. TEM images of a $In_xGa_{1-x}N$ film with x = 0.07. (a) plan-view image under $\boldsymbol{g} = 11\bar{2}0$. (b) Cross-section image under $\boldsymbol{g} = 1\bar{1}00$.

Dislocation clusters are also observed in $In_xGa_{1-x}N$ films with x = 0.12 but at a

higher density ~ $3.5\text{x}10^8$ cm^{-2} (Fig. 5.3(a)). The dislocation clusters are ~ 400 nm in

diameter and each has ~ 20 dislocations. From the cross-section TEM image in Fig.

5.3(b), not all of the dislocation clusters start from the $In_xGa_{1-x}N$/GaN interface with

some of them being ~ 70 nm above the interface. The surface above the dislocation

cluster is flat without any pits or trenches.

57
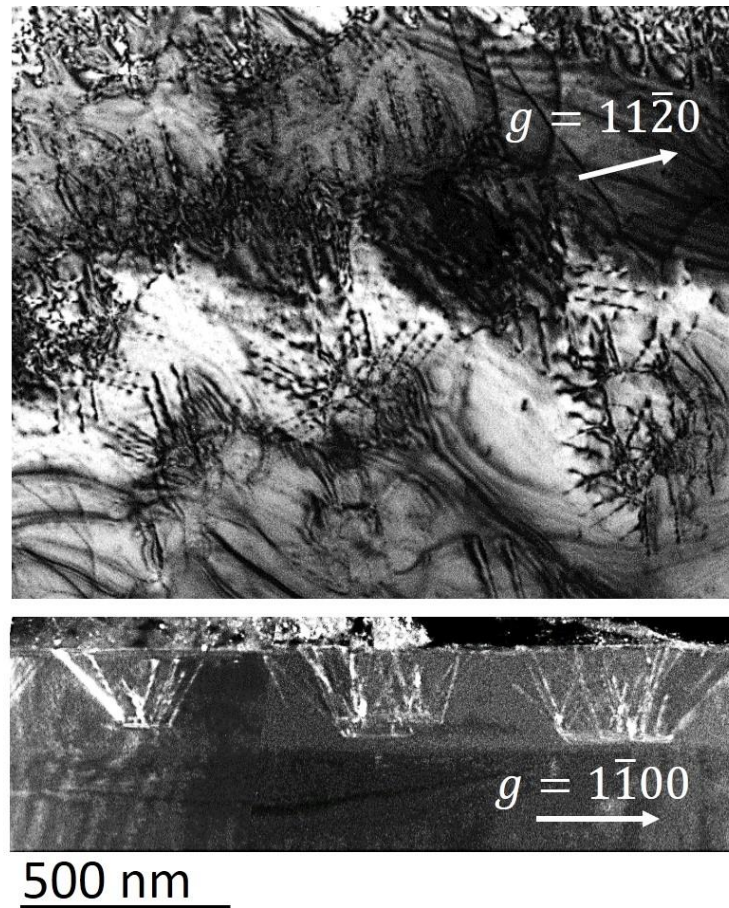
Figure 5.3. TEM images of a $In_xGa_{1-x}N$ film with x = 0.12. (a) plan-view image under $\boldsymbol{g} = 11\bar{2}0$. (b) Cross-section image under $\boldsymbol{g} = 1\bar{1}00$.

The microstructure of $In_xGa_{1-x}N$ films with x = 0.15 is different. An array of misfit

dislocations was observed which is formed by three groups of dislocations that are ~

60° to each other as shown in the plan-view TEM image in Fig. 5.4(a). One of the misfit

dislocations thread up to the surface near the center of the image. The average distance

between dislocations is ~ 260 nm. No dislocation clusters are observed. However, in

the cross-section TEM image in Fig. 5.4(b), a defect similar to a dislocation cluster is

observed which contains no dislocations but connects to trenches on the surface. This

kind of defects were reported in $In_xGa_{1-x}N$ multiple quantum wells[73,74] as well as in

$In_xGa_{1-x}N$ films[6,75].

$$g = 11\bar{2}0$$

$$g = 1\bar{1}00$$

500 nm
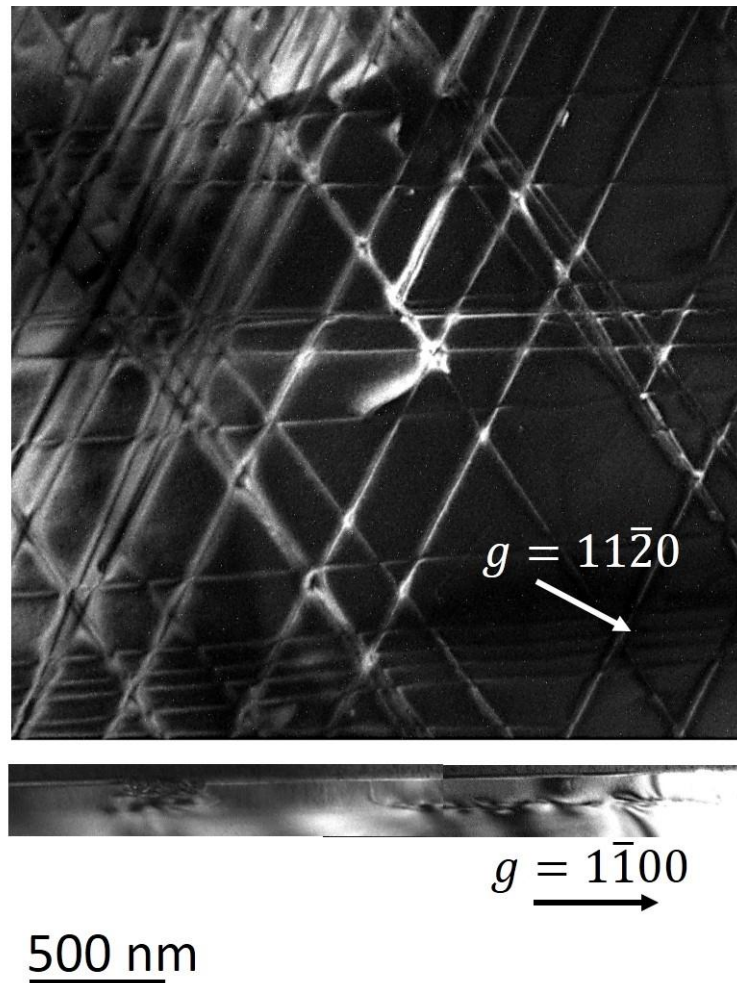
Figure 5.4. TEM images of the $In_xGa_{1-x}N$ film with x = 0.15. (a) Plan-view image under $\boldsymbol{g} = 11\bar{2}0$. (b) Cross-section image under $\boldsymbol{g} = 1\bar{1}00$.

The defects in this $In_xGa_{1-x}N$ film includes threading dislocation from the template layer, dislocation clusters, misfit dislocation arrays and trench defects, which appears in various regions of the film. The properties of these defects are studied below and the development of each kind of defects is discussed.

5.3.2. Dislocations from the template layer

The threading dislocations from the template layer can be sorted into two categories.

Some dislocations from the template layer bend at the interface and then thread straight up to the surface. (Fig. 5.5(a)) The Burgers vectors of this type of dislocation are determined using the $\boldsymbol{g} \cdot \boldsymbol{b}$ criteria. According to the $\boldsymbol{g} \cdot \boldsymbol{b}$ criteria, a dislocation is invisible when the product of the Burgers vector and the diffraction vector is zero. The visibility of a dislocation with a possible Burgers vector $\boldsymbol{b}$ under diffraction condition $\boldsymbol{g}$ is listed in Table 5.1. The bending dislocation are visible under $\boldsymbol{g} = 11\bar{2}0$ condition in Fig. 5.5(a) but not under $\boldsymbol{g} = 0002$ condition in Fig. 5.5(b), which indicates that it is an $\boldsymbol{a}$-type dislocation with Burgers vector $\boldsymbol{b} = 1/3[11\bar{2}0]$. The bending of the $\boldsymbol{a}$-type dislocation projects to a segment along [1-100] direction on the interface. This behavior of $\boldsymbol{a}$-type threading dislocation at hetero-interface have been previously reported.[14,76]
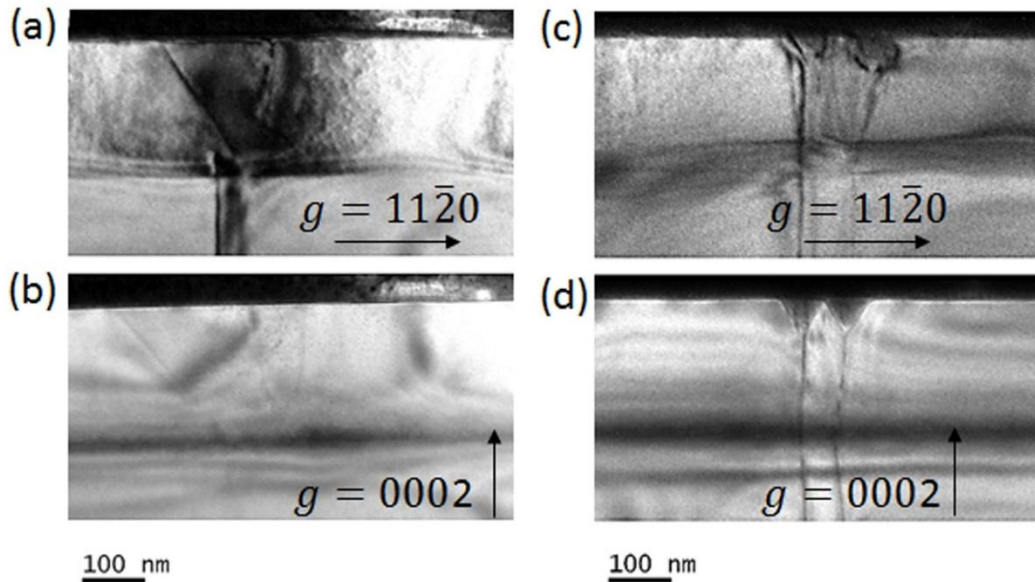
Figure 5.5. Two-beam diffraction-contrast TEM cross-section images of threading dislocations in a $In_xGa_{1-x}N$ film with x = 0.07: a-type dislocation under (a) $\boldsymbol{g} = 11\bar{2}0$ and (b) $\boldsymbol{g} = 0002$; two mixed-type dislocations under (c) $\boldsymbol{g} = 11\bar{2}0$ and (d) $\boldsymbol{g} = 0002$.

Table 5.1. Visibility of dislocations and stacking faults in $In_xGa_{1-x}N$.

Dislocation	Burgers vector	$g = 11\bar{2}0$	$g = 1\bar{1}00$	$g = 0002$
a-type:	$1/3[11\bar{2}0]$	all visible	1/3 invisible	all invisible
a+c-type:	$1/3[11\bar{2}3]$	all visible	1/3 invisible	all visible
c-type:	$[0001]$	all invisible	all invisible	all visible
Stacking fault	Displacement			
I1	$1/6[2\bar{2}03]$	invisible	visible	invisible
I2	$1/3[1\bar{1}00]$	invisible	visible	invisible

A threading **a**-type dislocation tilted away from the *c*-axis has an edge component, which interacts with the misfit strain in the lattice-mismatched epitaxial film and can contribute to strain relaxation. The amount of relaxation averaged over the film thickness is given by[14]:

$$\delta = \frac{1}{4} b_\perp \times \rho \times h \times tan\ \alpha \qquad (5.1)$$

where $b_\perp$ is the edge component of Burgers vector in the basal plane, ρ is the density of the **a**-type dislocations, h is the film thickness and α is the angle between dislocations and the normal of the interface. In the film with x = 0.07, $b_\perp = 0.318\ nm$, the density of dislocations is $\sim 10^8$ cm^{-2}, the thickness of the film is 230nm. In the cross-section image, the a-type dislocation bends in $(1\bar{1}00)$ plane forming an angle with the surface normal which is $\sim 36^\circ$ from the surface normal (Fig. 5.5(a)). The strain relaxed by the tilt of such **a**-type dislocation is estimated to be $\sim 0.001\%$.

Other dislocations from the template layer have *c*-component in their Burgers vectors which is evidenced by the visibility of these dislocations under $g = 0002$. These dislocations always leave a pit on the surface so the number of this kind of threading dislocations can be counted from topological surface measurements such as by AFM and SEM. A dislocation with a Burgers vector equaling *a+c* can glide on either $\{0\bar{1}11\}$ or $\{11\bar{2}2\}$ slip planes.[72] In the plan-view image in Fig. 5.1(a), the threading dislocations are observed to glide on $\{0\bar{1}11\}$ planes. The strain relaxation by an *a+c*-type dislocation is calculated by:

$$\delta = \frac{1}{2}b_\perp \times \rho \times l$$

(5.2)

where l is the distance that the *a+c*-type dislocation propagates on the interface which is ~ 250 nm from the plane-view image of the film with x = 0.07, and the dislocation density is ~10^8 cm^{-2}. Since the dislocation parallel to the interface forms a 60° angle with the *a* component, the edge component of the Burgers vector in the basal plane $b_\perp = b \times \sin 60° = 0.275\,nm$. The amount of relaxed strain by *a+c*-type dislocations is ~0.003%. In the In$_x$Ga$_{1-x}$N film with x = 0.07, the lattice mismatch is ~0.77% and thus the amount of strain relaxed by the threading dislocations are limited. In the film with similar thickness and more indium content, threading dislocations may relax more strain by either bending a larger angle for *a*-type dislocations or gliding for a longer distance for *a+c*-type dislocations.

5.3.3. Dislocation clusters

The dislocation clusters found in In$_x$Ga$_{1-x}$N film with x = 0.07 and 0.12 have

not been studied in detail. All of these dislocation clusters do not start from the initial

$In_xGa_{1-x}N$ interface with the substrate. Some are found ~ 70 nm above the interface.

The properties of this type of defects has been probed by a series of TEM diffraction

contrast images, as in Fig. 5.6. The fact that the dislocations are visible under $g = 11\bar{2}0$ (Fig. 5.6(a)) but not under $g = 0002$ (Fig. 5.6(b)) suggests that the Burgers

vectors of the dislocations are in the basal plane having no component in $[0001]$

direction. Similarly, by comparing the plan-view TEM images taken under $g = 11\bar{2}0$

(Fig. 5.6(c)) and under $g = 1\bar{1}00$ (Fig. 5.6(d)), dislocations of the clusters alone

$[1\bar{1}00]$ disappear under $g = 1\bar{1}00$ meaning that the Burgers vector is along $[11\bar{2}0]$

perpendicular to the diffraction vector. So the Burgers vectors are determined to be in

the basal plane and perpendicular to the dislocation lines.
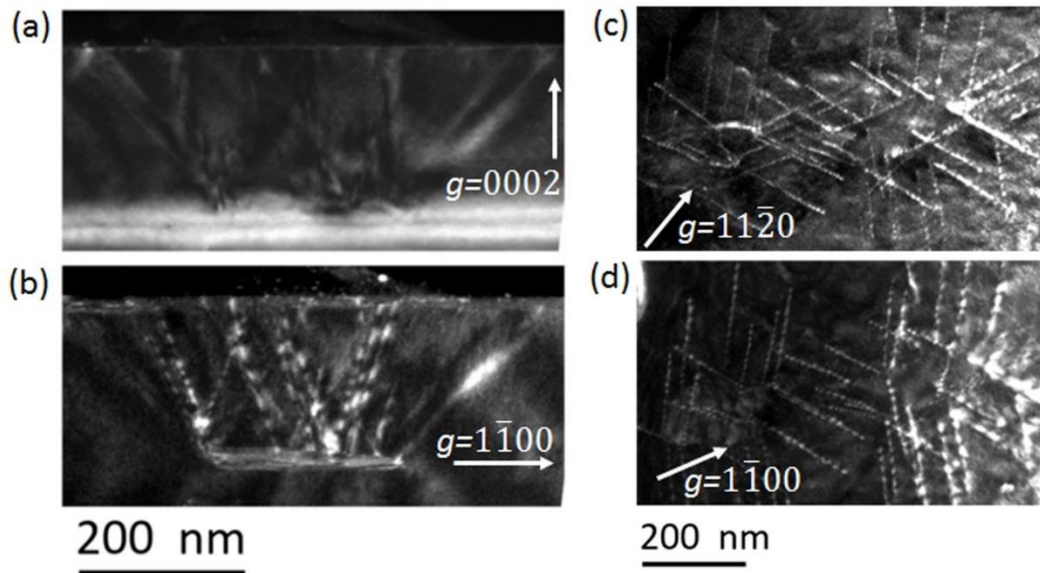
Figure 5.6. Weak-beam dark-field TEM images of dislocation clusters in the $In_xGa_{1-x}N$ film with x = 0.12. Cross-section TEM images under (a) $g = 0002$ and (b) $g = 1\bar{1}00$. Plan-view TEM images under (c) $g = 11\bar{2}0$ and (d) $g = 1\bar{1}00$ condition.

The exact nature of the Burgers vectors are determined by large-angle convergent-beam electron diffraction (LACBED).[77] Three dislocations in a cluster were studied (labelled in Fig. 5.7(a)) and the plan-view sample was tilted close to the $[10\bar{1}4]$ zone (Fig. 5.7(b)). The Bragg line intersecting a dislocation splits into several sections depending on the Burgers vector of the dislocation and on the nature of the Bragg line (Fig. 5.7(c)). Three LACBED images are recorded for each dislocation to completely determine the three independent components of the Burgers vector using Cherns and Preston rules[26]:

$$|g \cdot b| = m + 1 \qquad (5.3)$$

where g is the reciprocal lattice vector associated with the Bragg line, b is the magnitude of the Burgers vector of the dislocation, m is the number of subsidiary maxima at the intersection. The sign of $|g \cdot b|$ is determined by the direction of the dislocation, the positive deviation parameter and the asymmetric splitting at intersection. The direction of each of the three dislocations, the indices of each Bragg line, the values of $\boldsymbol{g} \cdot \boldsymbol{b}$ and Burgers vector of each dislocation are listed in Table. 5.2. The growth direction is pointing out the image which was carefully tracked during the TEM session. Combining the Burgers vector, the line direction of the dislocation and the growth direction, we concluded a missing plane is above each inclined dislocation in the dislocation clusters (Fig. 5.7(d)).
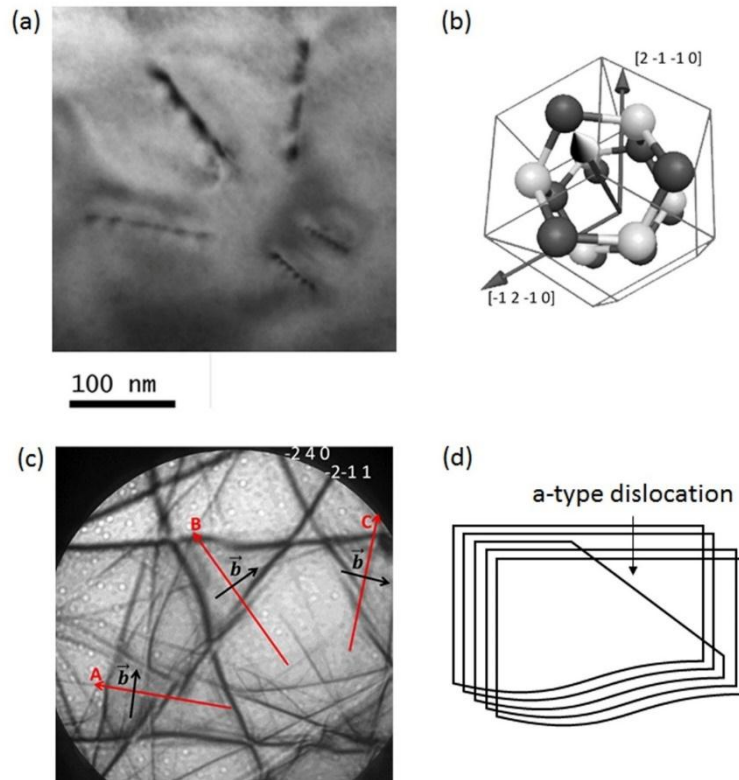
Figure 5.7. The Burgers vectors of the dislocations in a dislocation cluster in the $In_xGa_{1-x}N$ film with x = 0.07 were determined by LACBED. (a) The dislocation cluster imaged by two-beam diffraction-contrast imaging. (b) The orientation of the sample in the LACBED study. (c) One LACBED pattern showing splitting of Bragg lines due to intersection with dislocations. (d) Schematic showing of the missing plane associated with the a-type dislocation.

Table 5.2 Burgers vectors determined by LACBED and directions of dislocation lines.

	A			B			C		
g	$\bar{2}\,4\,0$	$4\,1\,\bar{2}$	$\bar{2}\,\bar{1}\,1$	$\bar{3}\,1\,1$	$\bar{2}\,\bar{1}\,1$	$\bar{3}\,2\,1$	$\bar{2}\,4\,0$	$1\,\bar{3}\,0$	$3\,\bar{2}\,\bar{1}$
$g \cdot b$	-2	4	-2	-1	1	-2	-2	2	-1
b	$[100] = 1/3[2\bar{1}\bar{1}0]$			$[0\bar{1}0] = 1/3[1\bar{2}10]$			$[\bar{1}\bar{1}0] = 1/3[\bar{1}\bar{1}20]$		
l	$[01\bar{1}0]$			$[10\bar{1}0]$			$[1\bar{1}00]$		

No dislocations were observed inside the dislocation cluster. In order to reveal

more details of the base of the dislocation clusters, the cross-section sample was tilted

65

away from edge-on orientation by ~ 20 degree. Bright-dark alternating fringes were observed on the base under $g = 1\bar{1}00$ (Fig. 5.8(a)) but not under $g = 11\bar{2}0$ (Fig. 5.8(b)). This contrast is associated with stacking faults, which is confirmed by high resolution lattice images. No misfit dislocations were observed on the base, which is obvious from the image of the tilted sample in $g = 11\bar{2}0$ condition in which the stacking faults was not visible.

(a)

$g = 1\bar{1}00$

(b)

$g = 11\bar{2}0$

200 nm
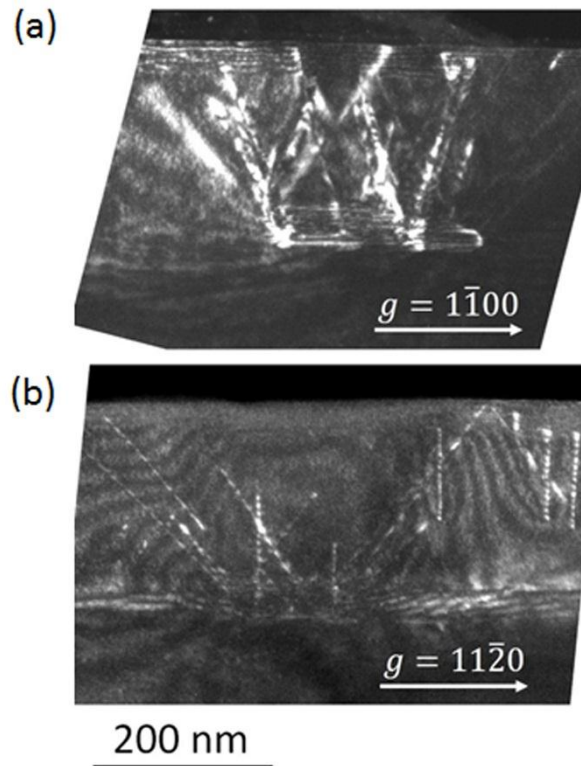
Figure 5.8. TEM images of the dislocation clusters in the In$_x$Ga$_{1-x}$N film with x = 0.12 indium content taken with the sample tilted away from edge-on direction. (a) Image under $g = 1\bar{1}00$ showing stacking fault and no misfit dislocations. (b) Image under $g = 11\bar{2}0$ condition showing no misfit dislocations. Stacking fault contrast was forbidden under this diffraction condition.

Based on the fact that no misfit dislocations were observed at the base of the dislocation clusters, two possible explanations about the origin of the dislocation

clusters can be given:

(1) A coherent interface: One way to relax lattice mismatch strain is by the generation of a misfit dislocation, the ends of which thread towards the surface during growth, creating a half loop. The misfit dislocation itself can dissociate into two partial dislocations with a stacking fault in between. The presence of a stacking fault with two threading a-type dislocations has been reported (Fig. 5.9(a)).[78,79] However, according to this explanation, each pair of a-type dislocations corresponds to a missing plane above the base of the cluster and the other extra half planes below the base accumulate on the edge of the base because there are no misfit dislocations on the base. This is only possible in the case of small number of dislocations as in ref [79]. We observed ~20 dislocation in one dislocation clusters (Fig. 5.3(a)) which means ~10 extra planes accumulating on the edge of the base. This is energetically not very likely.

(2) An incoherent interface: Another explanation assumes that the atomic layers above and below the base are separated by an incoherent interface. This incoherent interface probably originated from a liquid indium lagoon on the surface which slowed growth locally and was later covered by lateral overgrowth from the proceeding region around it (Fig. 5.9(b)). The formation of indium lagoon is probably resulted from indium enrichment at the growth front due to the exclusion of indium atoms by lattice mismatch stress[80] as well as the relatively low equilibrium pressure of indium droplets at low temperatures[71]. The overgrown film does not bond to the strained film underneath so it tends to recover to strain-free status. The dislocations on the edge

of the overgrown film realized the transition from the strained lattice to the relaxed lattice. In this case, though there are missing planes in the clusters, no one-to-one registry of atomic planes across the base is required and thus no misfit dislocations are produced. The stacking faults observed with the dislocation clusters were resulted from the interrupt of the growth by the indium lagoon.
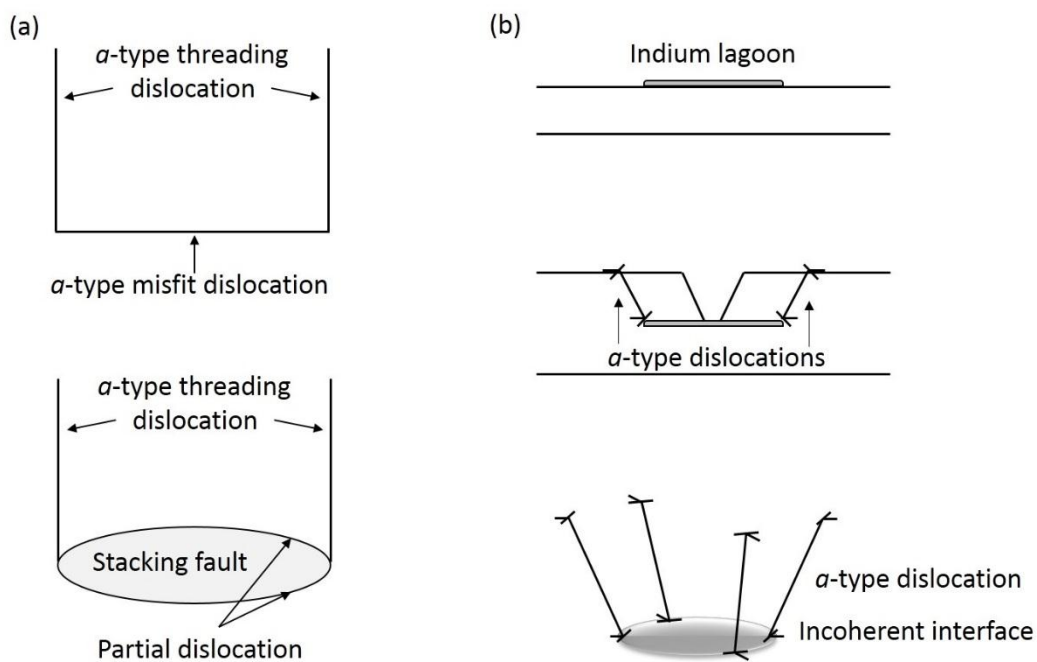
Figure 5.9. Two possible explanations for the formation of dislocation clusters. (a) Dislocations starting from a stacking fault. (b) Dislocations formed in the transition from the strained epitaxial film to the partially relaxed overgrown film over an incoherent interface.

Since the a-type dislocations of the dislocation clusters have edge component when projected to the interface, they can relax the misfit strain in the film. Since these dislocations are also inclined a-type dislocation, Eq. (5.1) is used to estimate the strain relaxation. In $In_xGa_{1-x}N$ film with $x = 0.12$, the number of dislocations associated with

each cluster is ~ 20, the typical size of the cluster is ~ 1.5×10^5 nm^2, so the density of

dislocation around the dislocation cluster is ~ 1.3×10^{10} cm^{-2}. The thickness of the film

is 230 nm, the inclination angle is 36°, which is the same as the inclined $\boldsymbol{a}$-type threading

dislocations and $b_\perp = 0.318 \, nm$. The strain in the local area at the dislocation cluster

is reduced by ~0.17%. Due to the strain relaxation, the material inside the dislocation

clusters was able to incorporate more indium during growth. From Fig. 5.1, the regions

inside dislocation clusters can have ~13.5% indium so that the residual strain inside the

cluster equals the misfit strain in the rest of the film.

The effect of indium fluctuation due to local strain relaxation by the dislocation

clusters is observed using cathodoluminescence. Figure 5.10(b) is the CL spectrum

taken from a 4x4 um^2 area (Fig. 5.10(a)). The emission peak is at 2.95 eV and has a

shoulder on the low energy side. Three monochromatic CL images were taken using

the luminescence at 2.82 eV, 2.90 eV and 2.99 eV (Fig. 5.10(c)-(e)). The CL map using

emission at 2.99 eV (Fig. 5.10(c))show that most area of the film has a strong emission

but this emission is weak in some localized regions which is ~400 nm in diameter each.

In contrast, these localized regions emit strongly at 2.82 eV (Fig. 5.10(e)) which means

a higher indium content in these area. So there are two spatially distributed

contributions to the total luminescence. One is from the localized regions and the other

is from rest of the film. The two contributions in the total emission spectrum are

deconvoluted with peaks at 2.90 eV and 2.96 eV, respectively. These two emission

energies correspond to the bandgaps of In$_x$Ga$_{1-x}$N with x = 0.12 and x = 0.135, assuming

a bowing parameter of 2,[81] and taking into account a 0.4 eV increase in bandgap due to the 1.3% strain in the film (see Fig. 5.1).[82]   In the monochromatic CL mapping using emission at 2.90 eV (Fig. 5.10(d)) where the two emission peaks have similar intensity, we found that the dislocation clusters do not eliminate emission though they include many dislocations. In contrast, several small dark spots were noticed, which are correlated with the surface pits observed in the SEM image (Fig. 5.10(a)). These surface pits are attributed to threading dislocations with a Burgers vector having a *c* component. Unlike the a-type dislocations in the dislocation clusters, these threading dislocations act as non-radiative recombination centers.
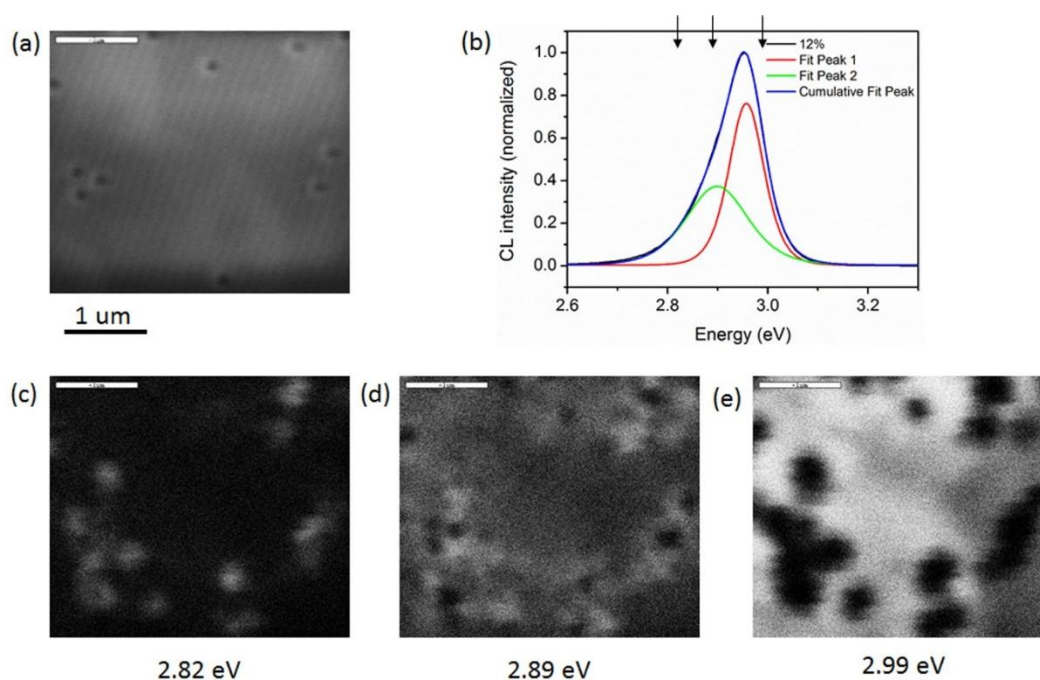
Figure 5.10. Surface and optical properties of the dislocation clusters. (a) SEM image showing the region of the film with x = 0.12 which was studied by CL. (b) The CL emission spectrum from the whole area shown in (a). (c)-(e) CL mappings using emission at 2.82 eV, 2.89 eV and 2.99 eV, respectively.

5.3.4. Trench defects

Another type of defects observed in the $In_xGa_{1-x}N$ film with x = 0.12 and 0.15 consist of a stacking fault in the film connected to a vertical stacking mismatch boundary which is terminated by a surface trench (Fig. 5.11(a)). AFM images (Fig. 5.11(b)-(d)) show that trench defects are only present in the $In_xGa_{1-x}N$ film with x=0.12 and x=0.15. Compared with the dislocation clusters in the $In_xGa_{1-x}N$ film with x = 0.12 (Fig. 5.3(a)), the shape of trench defects are more irregular and can be as long as 1 um in some direction (Fig 5.11(c) and (d)). The trench defects do not relax strain on a large scale and may cause some local relaxation near the surface by introduction of new surfaces.[6]
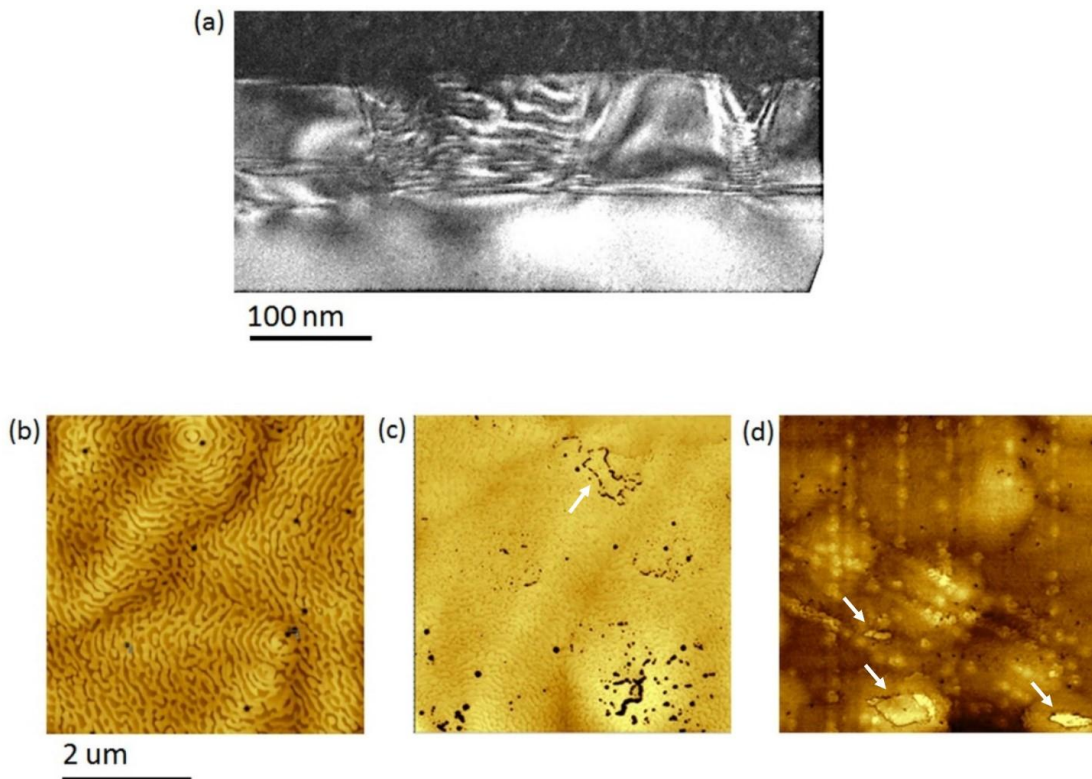
Figure 5.11. Identification of trench defects in $In_xGa_{1-x}N$ films. (a) TEM cross-section image of the trench defect in the film with x = 0.15. (b)-(d). AFM images showing the

surface of the films with x = 0.07, 0.12 and x = 0.15, respectively. The trench defects are labeled by white arrows.

The luminescence properties of the trench defects were also studied by CL from a $In_xGa_{1-x}N$ film with x = 0.15 (Fig. 5.12). The SEM image shows surface unevenness related to the trench defects (Fig. 5.12(a)). The emission from the whole area has contributions from two peaks (Fig. 5.12(b)). Three CL maps were recorded using emission at 2.77 eV, 2.81 eV and 2.89 eV (Fig. 5.12(c)-(e)). The emission with lower energy peaking at 2.77 eV originates from the edge of the trench defects (Fig. 5.12(c)). This is explained by the preferential incorporation of indium on undulated surfaces which red shifted the emission.[83] In the monochromatic CL mapping using emission at 2.81 eV (Fig. 5.12(d)), the brightness of the flat area of the film is highest compared with the other two CL maps. This trend follows the second emission peak reaching maximum at ~2.81 eV, suggesting the second emission peak are from the flat area of the film. Although the emission originating from the edge of the trench defects is lower than the emission from the rest of the film at 2.81 eV as seen in the CL spectrum of the whole area, the emission from the edge of trench defects is brighter in the CL map, which is reasonable considering their limited spatial coverage. The center of the trench defects does not emit which is probably due to a strong non-radiative recombination, which is different from the dislocation clusters.
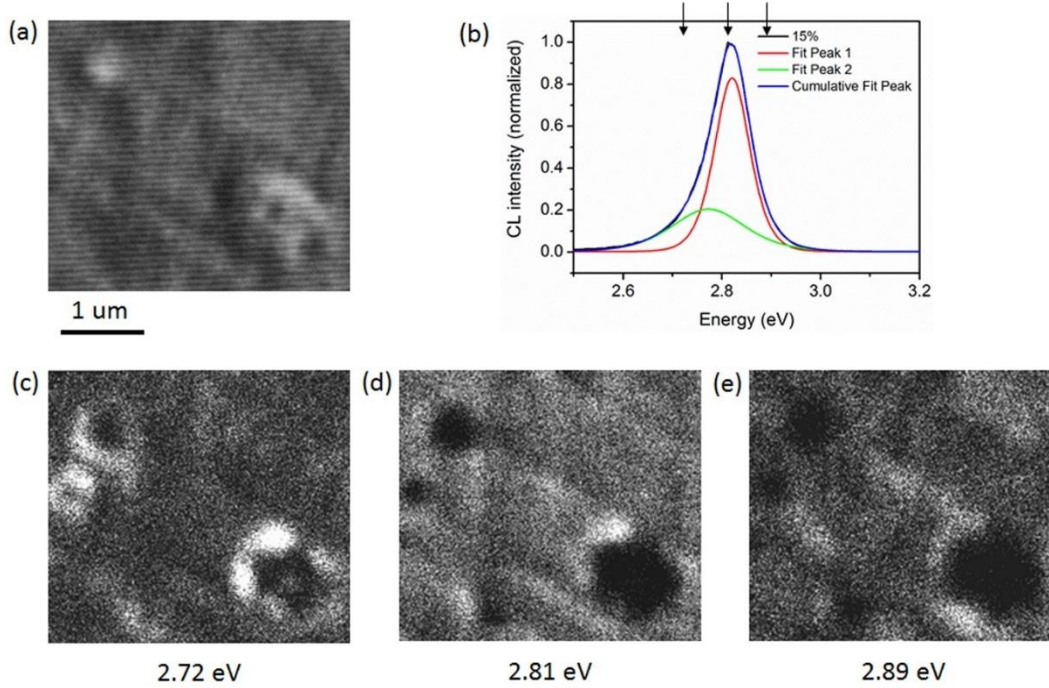
Figure 5.12. Surface and optical properties of the trench defects. (a) SEM image showing the region of the film with x = 0.15 which was studied by CL. (b) The CL emission spectrum from the whole area shown in (a). (c)-(e) CL mappings using emission at 2.72 eV, 2.81 eV and 2.89 eV, respectively.

5.3.5. Misfit dislocation array

A Misfit dislocation array is observed in the $In_xGa_{1-x}N$ film with x = 0.15. The dislocations divide into three groups each running in one of the three $\langle 1\bar{1}00 \rangle$ directions. One group of the misfit dislocations are invisible in the plan-view TEM image under $\mathbf{g} = 1\bar{1}00$ so their Burgers vector is alone $[11\bar{2}0]$ perpendicular to the $\mathbf{g}$ vector (Fig. 5.13, taken at the same location as Fig. 5.4(a)). The Burgers vector is also perpendicular to the dislocation lines which are parallel with $\mathbf{g}$. The edge component of the dislocation can relax the misfit strain by:

$$\delta = \frac{3}{2}b_\perp/d \quad\quad (5.4)$$

where $b_\perp$ is the in-plane edge component of Burgers vector, d is the average

73

spacing between misfit dislocations. The misfit dislocations have two possible origins.

(1) One is by gliding of the $a+c$-type threading dislocations on $\{11\bar{2}2\}$ planes. This mechanism requires the existence of $a+c$-type threading dislocations from the template layer. The edge component, $b_\perp$ of the resulted misfit dislocations equals a. (2) Alternatively, it was reported that misfit dislocations can generate by a "punch out" mechanism where two $a+c$-type dislocations on two opposite slip planes glide down from the surface pushing part of the film out of the surface. This mechanism does not require threading dislocations from the layer below and was observed in the $In_xGa_{1-x}N$ films grown on a free-standing GaN substrate with dislocation density less than 10^7 cm^{-2}.[15] The two gliding dislocations was reported to have the same a component but opposite c components. When they meet, they produce a misfit dislocation with Burgers vector equal $2a$ so $b_\perp$ equals $2a$. In our case, the threading dislocation density is $\sim 10^8$ cm^{-2} and the two mechanisms may operate simultaneously. The average spacing is ~ 240 nm measured from the plan-view TEM image (Fig. 5.4(a)). The amount of relaxed strain is $\sim 0.2\%$ assuming that all of the misfit dislocations were generated by the first mechanism and the in-plane edge component is a. The amount of relaxed strain is $\sim 0.4\%$ if assuming the second mechanism and the in-plane edge component being $2a$.
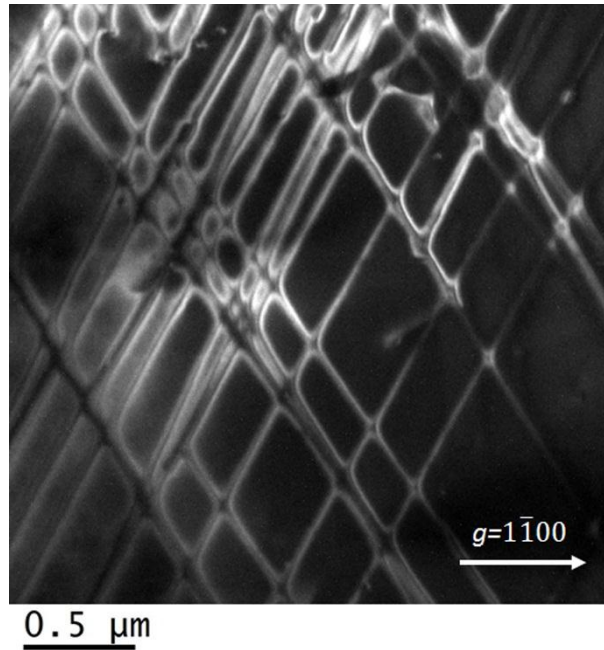
Figure 5.13. The misfit dislocation array in the $In_xGa_{1-x}N$ film with x = 0.15 under $\boldsymbol{g} = 1\bar{1}00$ condition. One set of misfit dislocations are missing under this condition.

5.3.6. Conclusions

The defects in $In_xGa_{1-x}N$ films with x = 0.07, 0.12 and 0.15 have been investigated. Threading dislocations from the GaN template layer are present in each film. The amount of strain relaxation depends on the type of the dislocation, the film thickness and the glide distance of the dislocations. In $In_xGa_{1-x}N$ with x = 0.07 and 0.12, the threading dislocation cause an insignificant amount of strain. Dislocation clusters were observed in the $In_xGa_{1-x}N$ films with x = 0.07 and 0.12, and the density of the clusters increases with indium content. We propose that the generation of dislocation clusters are probably due to the formation of indium lagoons and a consequent incoherent interface between the film and the underlying GaN layer. The dislocations in the clusters play a role in a transition from strained lattice outside the clusters to the partially relaxed lattice inside the clusters. The dislocation clusters cause local strain

relaxation and the incorporation of additional indium, with local luminescence indicating lower bandgaps. The *a*-type dislocations in the dislocation clusters do not act as non-radiative recombination centers. Trench defects are observed in films with x = 0.12 and 0.15. The trench defects cause indium segregation on their edges contributing to emission at lower energies. In $In_xGa_{1-x}N$ films with x=0.15, a misfit dislocation array formed which relaxed the strain on a large scale by ~ 0.2% to 0.4%.

CHAPTER 6

CHARACTERIZATION OF $In_xGa_{1-x}N$ (x ≥ 0.20) EPILAYERS GROWN BY

MOLECULAR BEAM EPITAXY [*]

6.1. Introduction

The $In_xGa_{1-x}N$ film with indium content below 20% in the previous chapter were grown by MOCVD. Growth of $In_xGa_{1-x}N$ films with indium content higher than 20% are difficult to obtain in good crystalline qualities by the same growth method. The difficulty lies in the high temperature needed to break the N-H bonds in ammonia (typically ~ 1,000°C), and the high indium vapor pressure under such conditions.[84] It has been reported that $In_xGa_{1-x}N$ grown by MOCVD with indium content x > 0.2 is thermodynamically unstable and has a tendency to spontaneously decompose into two phases during the vapor phase epitaxy. When the indium content is higher than 25%, the film is no longer a single crystal.[85] Surface kinetics may play a significant role in MOCVD at relatively low temperatures.[84] Growth of $In_xGa_{1-x}N$ with indium content up to 63% by MOVPE at low temperature has been reported[86] but the materials showed broad peaks in XRD indicating the presence of compositional inhomogeneity.

$In_xGa_{1-x}N$ films with indium content over the entire content range were grown by

molecular beam epitaxy (MBE) at 400-750 °C with little signs of spinodal decomposition.[87] The reason for the existence of non-equilibrium phases is probably because surface kinetics controls the MBE growth in this temperature range. A report by another group shows that $In_xGa_{1-x}N$ films with indium content > 30% grown by MBE in the temperature range from 700 to 800 °C exhibit spinodal decomposition.[88] It needs to be pointed out that the growth of $In_xGa_{1-x}N$ by different groups may involve a variety of growth parameters making tentative the explanation offered by the different groups.

For InGaN with high indium content, the lattice mismatch between the films and the templates (usually GaN or AlN) is large and thus a large misfit strain is observed in the films. A natural question is about the mechanism of misfit strain relaxation. To answer this question, it is necessary to measure the degree of strain relaxation. X-ray diffraction is often used for this purpose.[89,90] But XRD does not directly show the microstructures of the InGaN films that may provide clues for the understanding of the relaxation mechanism.

In this chapter, the results of a study by TEM of the microstructure of $In_xGa_{1-x}N$ films with $x \geq 0.20$ is presented. Electron diffraction patterns and moiré fringes in TEM images are used to measure the strain relaxation. Interfacial relaxation is observed and its onset is explained by a critical thickness model.

6.2. Experimental details

$In_xGa_{1-x}N$ films with indium content ranging from 20% to 80% were grown by

MBE under N-rich condition at temperatures from 450 to 360 °C. The nominal film structure consisted of a ~ 55 nm-thick $In_xGa_{1-x}N$ film with a ~ 10 nm-thick GaN capping layer. Two sets of films were grown on GaN/sapphire and on AlN/sapphire, respectively. The contents of the $In_xGa_{1-x}N$ films were determined by XRD.[7, *]

Cross-section TEM samples were prepared by wedge polishing followed by ion milling using 3.7 keV and then 2.0 keV argon ion beams at liquid nitrogen temperatures. The TEM images were taken in a Philips CM200 transmission electron microscope using a 200-keV electron beam.

6.3. Results and discussion

6.3.1. Microstructures of $In_xGa_{1-x}N$ films grown by MBE

Figure 6.1 shows the diffraction patterns and TEM images of $In_xGa_{1-x}N$ films with various indium contents grown on GaN/sapphire. The diffraction patterns were taken using a SAD aperture to include the $In_xGa_{1-x}N$ film and part of the GaN template. Two arrays of diffraction spots are observed. The smaller array is from $In_xGa_{1-x}N$ films since $In_xGa_{1-x}N$ has larger lattice parameters corresponding to smaller lattice in the reciprocal space. The difference between the two arrays of diffraction spots increases as the indium content corresponding to the increasing difference in the lattice parameters.

The TEM images in Fig. 6.1 were taken in two-beam condition with $g = 2\bar{2}00$ or $g = 22\bar{4}0$. The TEM images show that the thickness of most $In_xGa_{1-x}N$ layers are

---

(*) The MBE growth and XRD analysis were done at the Georgia Institute of Technology, Atlanta, Georgia, USA.

~ 60 nm, which may include GaN capping layers that are barely distinguishable. The thickness of $In_xGa_{1-x}N$ film with $x = 0.67$ is less than 50nm which is probably due to the thickness inhomogeneity near the clamped region that suffers from shadowing during the growth. The $In_xGa_{1-x}N$/GaN interfaces show different features for different indium contents. For $x = 0.2$ (Fig. 6.1(a)), the interface is not abrupt, which is attributed to the straining of the $(1\bar{1}00)$ planes. For $x = 0.37$, 0.52 and 0.67 (Figs. 6.1(b)-(d)), the contrast in the films is due to relative rotation and tilting of a columnar structure. Moiré fringes are observed at the $In_xGa_{1-x}N$/GaN interface for $x = 0.67$. For $x = 0.82$ (Fig. 6.1(e)), some bright domes are seen at the interfaces. The origin of the bright regions could be indium accumulation that has been preferential etched during ion milling.
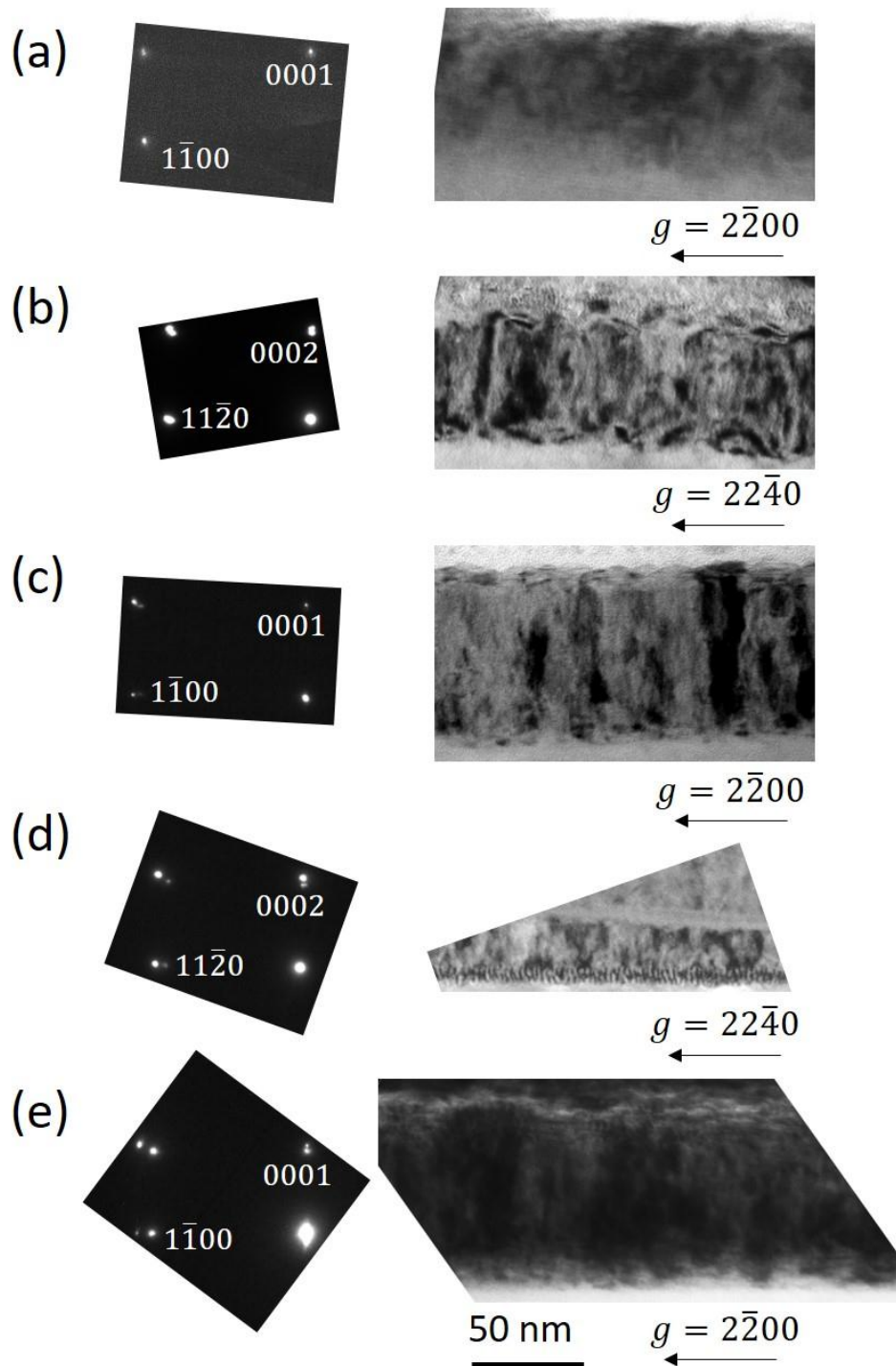
Figure 6.1. Diffraction patterns and TEM images of $In_xGa_{1-x}N$ layers grown on GaN template with (a) x = 0.20, (b) x = 0.37, (c) x = 0.52, (d) x = 0.67, and (e) x = 0.82.

To test the effect of the under layer, another set of $In_xGa_{1-x}N$ films were grown on

AlN templates (instead of GaN templates) by MBE with indium contents ranging from

~20% to ~80%. Cross-sectional TEM images of the $In_xGa_{1-x}N$ films are shown in Figure

6.2. The films exhibit similar features as observed in the films grown on GaN template.

The moiré fringes appear at the interface for x = 0.48 and 0.64. Our study of the film

with x = 0.80 did not give conclusive results.
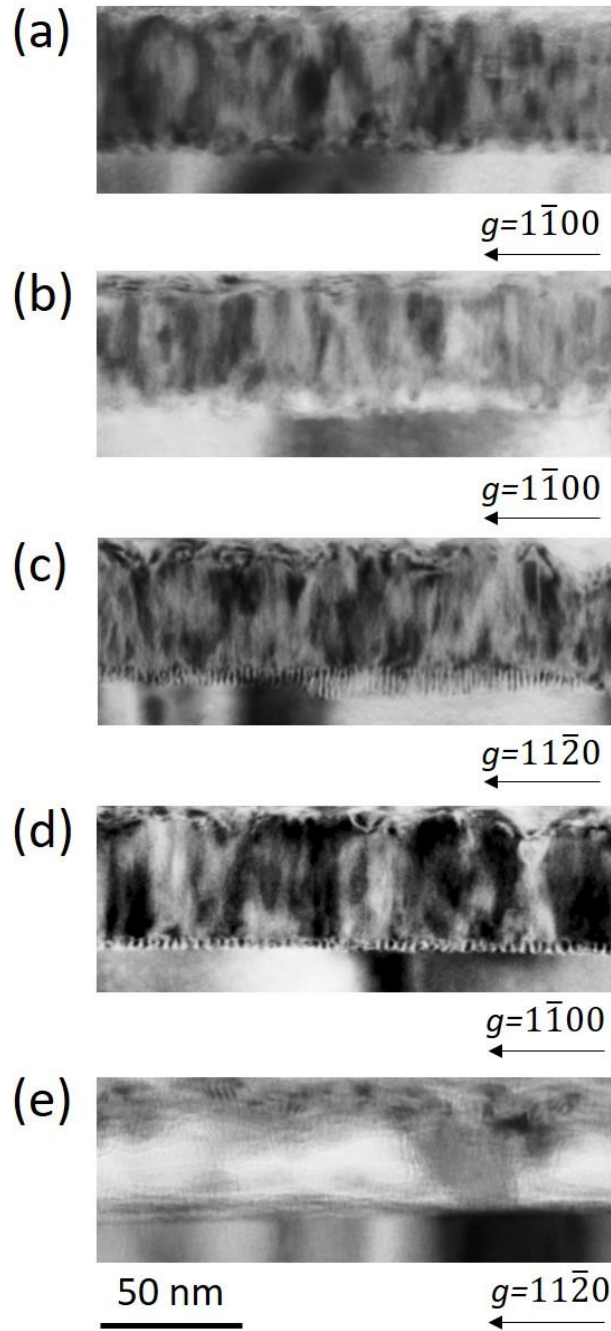
Figure 6.2. TEM images of $In_xGa_{1-x}N$ layers grown on AlN template with (a) x = 0.21, (b) x = 0.33, (c) x = 0.48, (d) x = 0.64, and (e) x = 0.80.

6.3.2. Measurement of strain relaxation from diffraction patterns

For the determination of strain relaxation using diffraction patterns, some prior knowledge about the strain conditions in the epitaxial films is needed. Hexagonal

systems have two lattice parameters, one is in the basal plane denoted by a and the other is normal to the basal plane denoted by c. In InGaN/GaN hetero-epitaxy, the lattice parameter of the film parallel to the interface is compressively strained due to the lattice mismatch, and a tensile strain is generated along the c-axis, as described by the Poisson ratio. For a basal plane epitaxial hexagonal system, the relationship between the change of the two lattice parameters Δc and Δa is:

$$\frac{\Delta c}{c_0} = \varepsilon_{zz} = -\frac{2v}{1-v}\varepsilon_{xx} = -\frac{2v}{1-v}\frac{\Delta a}{a_0} \tag{6.1}$$

where a_0 and c_0 are the lattice parameters of the relaxed crystal; ε_{zz}, ε_{xx} are strain in the growth direction and in the basal plane, respectively; and v is the Poisson ratio.

The lattice parameter c of the strained film is a function of the lattice parameter a:

$$c = (c_0 + \Delta c) = c_0 \left(1 - \frac{2v}{1-v}\frac{\Delta a}{a_0}\right) = c_0 \left(\frac{1+v}{1-v} - \frac{2v}{1-v}\frac{a}{a_0}\right) \tag{6.2}$$

For relaxed $In_xGa_{1-x}N$, the lattice parameters follow Vegard's law:

$$a_0[In_xGa_{1-x}N] = x \cdot a_0[InN] + (1-x) \cdot a_0[GaN] \tag{6.3}$$

$$c_0[In_xGa_{1-x}N] = x \cdot c_0[InN] + (1-x) \cdot c_0[GaN] \tag{6.4}$$

The lattice parameters a_0 and c_0 are plotted as a function of indium content x in Figure 6.3.
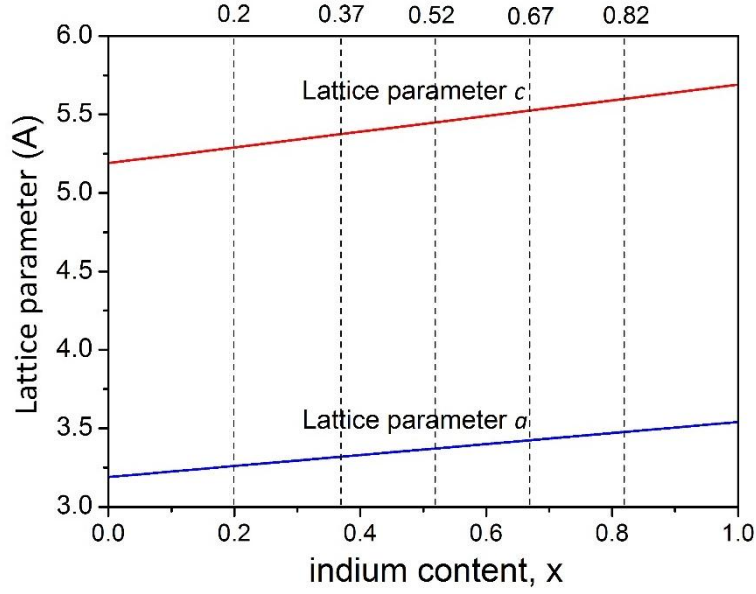
Figure 6.3. Lattice parameters as a function of indium content x.

For In$_x$Ga$_{1-x}$N grown on c-plane GaN, the lattice parameter a is stretched, the misfit strain is defined as

$$\varepsilon_m = \frac{a_s - a_f}{a_f} \qquad (6.5)$$

where a_s and a_f are the lattice parameters of relaxed GaN templates and relaxed InGaN films, respectively. The sign of the misfit strain tells whether the film is stretched or compressed. In our case, the misfit strain is negative signifying a compressive strain in the film. The magnitude of misfit strain as a function of indium content is plotted in Figure 6.4. For x = 0.2, 0.37, 0.52, 0.67, 0,82, the magnitude of the misfit strain is 2.1%, 3.9%, 5.4%, 6.8% and 8.3%, respectively.
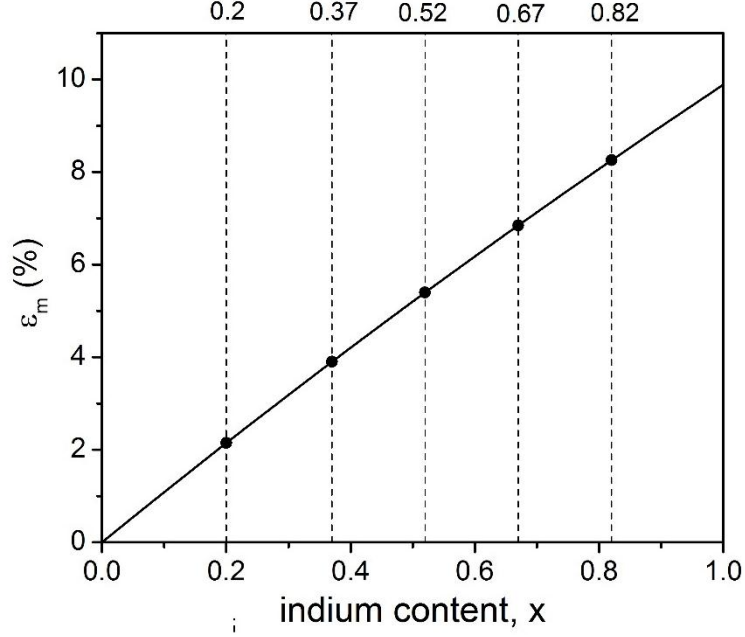
Figure 6.4. Misfit strain in $In_xGa_{1-x}N$ grown on GaN template as a function of indium content x.

The strain in the film changes the interplanar spacing of each set of crystal planes by changing the lattice parameters. The dependence of the interplanar spacing on the lattice parameters in a hexagonal lattice is

$$\frac{1}{d^2} = \frac{4}{3}\left(\frac{h^2 + hk + k^2}{a^2}\right) + \frac{l^2}{c^2} \qquad (6.6)$$

where d is the interplanar spacing, h, k, l are the Miller indices. The interplanar spacing is the inverse of the magnitude of the reciprocal lattice vector that can be measured from the diffraction pattern.

For the study of a general strain condition, a diffraction spot that measures the in-plane lattice parameter a and the out-plane lattice parameter c is very useful. Here we choose the $11\bar{2}4$ diffraction to study the strain condition in the $In_xGa_{1-x}N$ film grown on GaN. Using Eq. (6.1), the interplanar spacing of $(11\bar{2}0)$ planes and (0004) planes are

$$d_{11\bar{2}0} = \frac{1}{2}a \tag{6.7}$$

$$d_{0004} = \frac{1}{4}c \tag{6.8}$$

For a crystal plane, the conversion from four indices that are commonly used for hexagonal system to three indices as is used in Eq. (6.2) is simply dropping the third index. The magnitude of reciprocal lattice vectors $g_{11\bar{2}0}$ and g_{0004} are proportional to the inverse of $d_{11\bar{2}0}$ and d_{0004} and can be expressed as a function of strained lattice parameter a:

$$g_{11\bar{2}0} = \frac{1}{d_{11\bar{2}0}} = \frac{2}{a} \tag{6.9}$$

$$g_{0004} = \frac{1}{d_{0004}} = \frac{4}{c} = \frac{4}{c_0 \left(\frac{1+\nu}{1-\nu} - \frac{2\upsilon}{1-\nu} \frac{a}{a_0} \right)} \tag{6.10}$$

Figure 6.5 shows g_{0004} as a function of $g_{11\bar{2}0}$ for indium content $x = 0.37$ (blue solid line) and 0.67 (red solid line) assuming Poisson ratio is 0.2.[91] Each solid line corresponds to the films with constant indium content but different residual strains so these solid lines are called iso-composition lines. The degree of strain relaxation is defined as the ratio of the relaxed strain to the misfit strain:

$$R = \frac{\varepsilon_m - \varepsilon_{xx}}{\varepsilon_m} = \frac{a_s - a}{a_s - a_f} \tag{6.11}$$

The dash lines in Fig. 6.5 show the trajectory for constant relaxation degree. The vertical dash line corresponding to a fully strained condition, or zero degree of relaxation. The dash line with $R = 1$ corresponding to a fully relaxed condition.
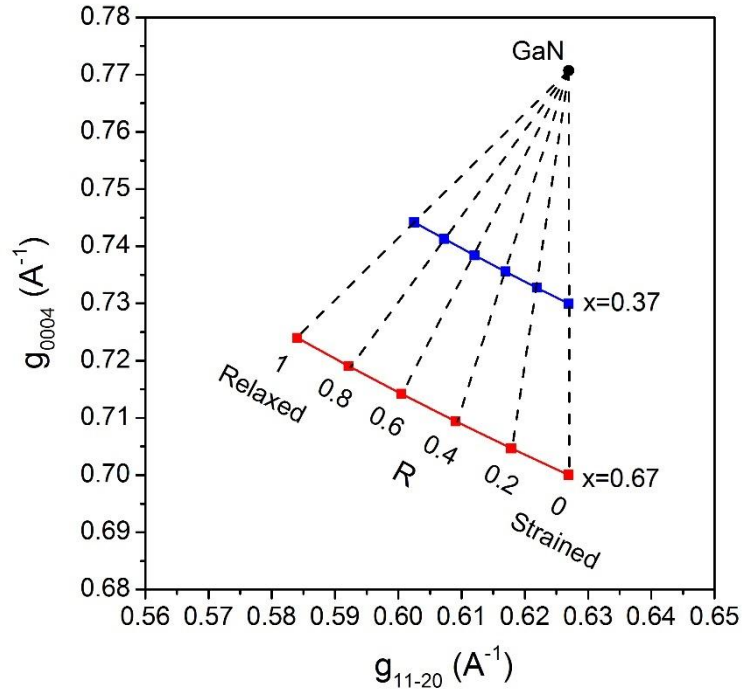
Figure 6.5. g_{0004} as a function of $g_{11\bar{2}0}$. Iso-composition lines (solid lines) and Iso-strain lines (dash lines) are shown.

Since in the reciprocal space g_{0004} is perpendicular to $g_{11\bar{2}0}$, Fig. 6.5 can be seen as a "ruler" that can measure strain relaxation once aligned with the diffraction pattern. $In_xGa_{1-x}N$ films with indium content of 37% and 67% are used as examples to show the procedure. The GaN $11\bar{2}4$ diffraction spot and the direct beam spot in the diffraction pattern are aligned to coincide with the GaN data point and origin (which is not shown here), respectively. The resulted figures are shown in Fig. 6.6. For $In_xGa_{1-x}N$ film with $x = 0.37$ (Fig. 6.6(a)), the diffraction spot of $In_xGa_{1-x}N$ is relatively wide. The diffraction spot falls close to the $R = 0.4$ line meaning ~ 40% of the strain in film has been relaxed. On the other hand, the diffraction spot extends in the direction normal to the iso-composition line, implying possible content inhomogeneity in the film. For $In_xGa_{1-x}N$ film with $x = 0.67$, the diffraction spot falls between $R = 0.8$ and $R = 1$ lines,

corresponding to a relaxation degree of ~90%. The diffraction spot of $In_xGa_{1-x}N$ is

relatively narrow indicating a fairly uniform content. Quantification based on the width

of the diffraction spots are not done here for the reason that will be mentioned at the

end of this section. The degree of strain relaxation for other $In_xGa_{1-x}N$ films grown on

GaN are summarized in Table 6.1. The relaxation degree increases with the indium

content almost linearly in the range of $x < 0.52$, then undergoes a faster increase to 90%

between $0.52 < x < 0.67$ and reaches 100% at $x = 1$. The fast increase of relaxation

degree implies the onset of a new relaxation process.
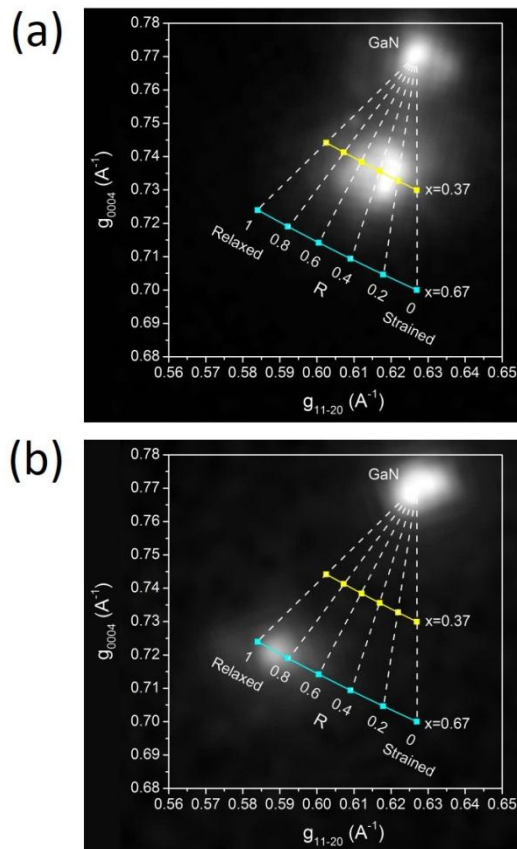
Figure 6.6. The diffraction pattern overlapped with Fig. 6.10. (a) Diffraction pattern for $x = 0.37$. (b) Diffraction pattern for $x = 0.67$.

Table 6.1. The degree of relaxation measured from diffraction pattern

Indium content	0.20	0.37	0.52	0.67	0.82
R by diffraction pattern	~ 20	~ 40	~ 60	~ 90	~ 100

The principle of this method is similar to strain measurement by X-ray reciprocal spacing mapping (RSM).[89] In X-ray RSM, the sample and detector have to be moved to probe each position in reciprocal space. While in electron diffraction, the diffraction spots in the zero-order Laue zone can be easily obtained with the incident beam aligned along the zone axis. The tolerance of deviation from exact Bragg conditions comes from two aspects: (1) the wavelength of the electron wave is much smaller than the lattice parameter so that the Laue sphere is almost flat near the origin of the zero order Laue plane, and (2) the thickness of the TEM sample is typically less than 200 nm and the reciprocal lattice points are stretched in the direction normal to the sample foil. However, the accuracy of the strain measurement by electron diffraction is expected to be not as good as X-ray RSM because of the tolerance in the deviation from exact Bragg condition. The short wavelength of electrons results in smaller Bragg angles, which requires more accurate angular measurement in order to achieve a similar accuracy as in X-ray RSM.

6.3.3. Measurement of strain relaxation from moiré fringes

Moiré fringes are observed at the interfaces for $In_xGa_{1-x}N$ with x = 0.67 on GaN template and for $In_xGa_{1-x}N$ with x = 0.48 and 0.64 on AlN template. Moiré fringes form when the electron beam passes through two materials with different lattice parameters.

In $g = 2\bar{2}00$ condition, the TEM sample is tilted away from the zone axis. The interface is no longer observed edge-on along the electron beam direction. When the electron beam pass near the interface, it sequentially passes the $In_xGa_{1-x}N$ film and the template. If the film is relaxed at the interface, moiré fringes will be produced. The spacing between the fringes can be used to deduce the lattice parameter of the film assuming the lattice parameter of the template is unchanged due to its large thickness. Moiré fringes are the interference pattern produced by the beams corresponding to the split diffraction spots and the spacing is described by

$$l = \frac{1}{|\boldsymbol{g} - \boldsymbol{g_s}|} \quad (6.12)$$

where l is the spacing between fringes, $\boldsymbol{g}$ and $\boldsymbol{g_s}$ are the reciprocal lattice vectors of the film and the template, respectively. For c-plane epitaxy and two-beam condition with $\boldsymbol{g} = 2\bar{2}00$, $\boldsymbol{g}$ and $\boldsymbol{g_s}$ are along the same direction and the moiré fringe spacing can be related to the lattice parameter a by

$$l = \frac{1}{g - g_s} = \frac{\sqrt{3}}{4} \frac{aa_s}{a - a_s} \quad (6.13)$$

where a and a_s are the lattice parameters of film and substrate, respectively.

For the $In_xGa_{1-x}N$ film with x = 0.67 grown on an GaN template, the spacing between moiré fringes is 2.42 nm and the lattice parameter a is 3.38 A. Using Eq. (6.11), the relaxation degree R ≈ 82%, which is slightly less than the relaxation degree measured from its diffraction pattern (~ 90%). This means that the interfacial relaxation reduces the strain by 82% and the rest 8% is believed to happen in the film above the interface.

A similar study has been carried out for each of the other samples that show moiré fringes at the interface. Table 6.2 summarizes the results. For $In_xGa_{1-x}N$ grown on GaN template with x < 0.52, no clear moiré fringes are observed at the interface meaning little strain relaxation happened at the interface. For $In_xGa_{1-x}N$ grown on an AlN template, clear moiré fringes are present for x = 0.48.

Table 6.2. Degree of relaxation at the interfaces.

$In_xGa_{1-x}N$ on GaN	0.20	0.37	0.52	0.67	0.82
	N/A	N/A	N/A	$R \approx 0.82$	N/A
$In_xGa_{1-x}N$ on AlN	0.21	0.33	0.48	0.64	0.80
	N/A	N/A	$R \approx 0.71$	$R \approx 0.62$	N/A

Compared with the diffraction method that usually measures strain in the whole film, moiré fringes can be used to measure the strain relaxation happening at the interface. The tilt angle used in two-beam condition is ~5° and the TEM sample thickness is ~100 nm. The resulting overlapping region is $100 \text{ nm} \times \tan 5° \approx 9 \text{ nm}$ from the interface. The overlapped region can be further reduced by moving to a thinner area on the TEM sample or reducing the tilting angle. However, the requirement of overlapping region limits the use of this method for strain measurement in the middle of film. The visibility of the moiré fringes is also a prerequisite.

6.3.4. A critical thickness model to explain the interfacial relaxation

In the previous two sections, we have seen that for $In_xGa_{1-x}N$ films grown on GaN template, the relaxation degree increases fast at x = 0.67. This fast increase coincides

with the appearance of moiré fringes that indicates an interfacial relaxation. Similar trend is observed for $In_xGa_{1-x}N$ films grown on AlN.   Interfacial relaxation happens at x = 0.48.

The occurrence of interfacial strain relaxation is explained using a critical thickness model which predicts the minimum film thickness for the generation of misfit dislocations as a function of lattice mismatch.[*] The lattice mismatch strain depends on the indium content in the film so the critical thickness is also a function of indium content. The critical thickness model proposed by Matthews and Blakeslee (section 2.1.2) considers that the relaxation happens when the force due to the lattice-mismatch strain is equal to the dislocation line tension.[22] This method has been applied to InGaN by Srinivasan and expanded by Fischer.[5,72]

For a GaN template, the critical thickness as a function of the indium content based on the Matthews-Blakeslee model is shown in Fig. 6.7 (red curve). The dislocation line tension in both models are formulated in a continuum framework, which is only valid when the film thickness is larger than the lattice parameters, so the models do not give real critical thickness for film thickness close to lattice parameters. However, the critical thickness as a function of indium content should continue the trend of the curve as shown by the dash line in Fig.6.7. It is found that when the indium content reaches ~0.55, the critical thickness is below one lattice parameter c. This means that at the

initial stage of the growth, the indium-rich $In_xGa_{1-x}N$ spontaneously nucleates in a nearly fully relaxed state, with an array of misfit dislocations forming on the interface.

For AlN template, the critical thickness curves are also shown in Fig. 6.7 (blue curve). Compared with GaN, AlN has smaller lattice parameters, which results in a larger lattice mismatch between InGaN films and AlN templates for each indium content. The critical thickness for $In_xGa_{1-x}N$ with $x > 0.4$ is less than one lattice parameter, which matches well with the observation of interfacial relaxation starting from $x = 0.48$.
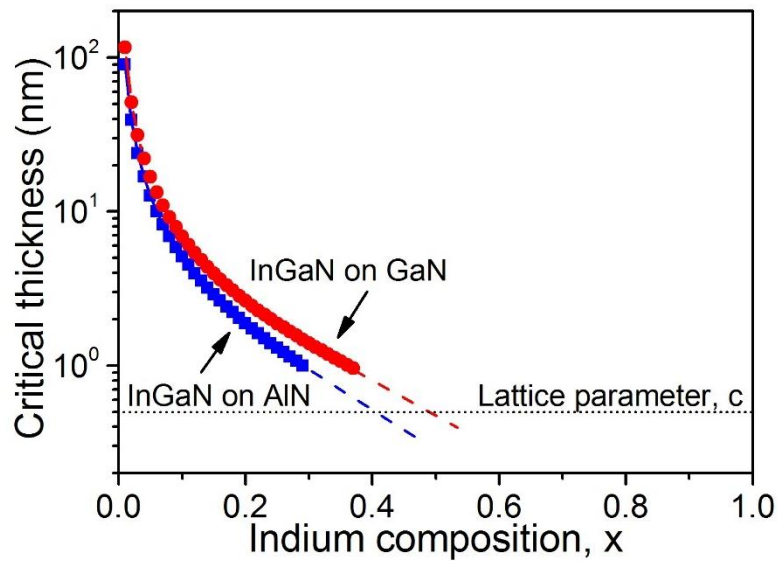
Figure 6.7. Critical thickness as a function of indium content for $In_xGa_{1-x}N$/GaN/sapphire and $In_xGa_{1-x}N$/AlN/sapphire.

6.4. Conclusions

The microstructures of $In_xGa_{1-x}N$ films on GaN or AlN templates with $x \geq 0.2$ have been studied by TEM. The $11\bar{2}4$ diffraction spot is used to measure the strain in the films. For the $In_xGa_{1-x}N$ films on GaN templates, the diffraction pattern shows that the

degree of strain relaxation increases more rapidly at x ~ 0.67. This rapid increase is associated with an interfacial strain relaxation revealed by the presence in the TEM image of moiré fringes at the interface. For $In_xGa_{1-x}N$ film grown on AlN template, the interfacial relaxation is observed at x ~ 0.48. Calculation based on a critical thickness model shows that the interfacial strain relaxation is due to the critical thickness reaches a value of the order of a monolayer, leading to spontaneous nucleation of relaxed $In_xGa_{1-x}N$ with a periodic misfit dislocation array on the interface.

CHAPTER 7

SUMMARY AND FUTURE WORK

7.1. Summary

In this dissertation, III-V semiconductor thin film structures for solar cell applications are studied. Good structural and optical properties of the thin film structures are necessary for fabrication of high efficiency photovoltaic devices. TEM is used to characterize the microstructures to understand the development of defects. PL or CL are used for characterization of optical properties.

In chapter 4, InAs QDs are grown by MOVPE and covered by capping layers of different thicknesses. QDs that are fully protected by the capping layer are plastically relaxed by generation of misfit dislocations. The QDs with reduced height do not have dislocations, which is explained by a forced balanced critical thickness model. The optical properties of the strained QDs show an improvement due to the absence of the dislocations as non-radiative recombination centers. The luminescence from the strained QDs are correlated with the morphology and lateral size distribution of the QDs. An InAs cover layer due to the partial capping plus annealing step reduces the confinement of carriers in the QDs.

In chapter 5, $In_xGa_{1-x}N$ films with $x \leq 0.15$ grown by MOCVD are studied. The defects found in these $In_xGa_{1-x}N$ films include dislocations from the template, dislocation clusters, misfit dislocation arrays and trench defects. The strain relaxation due to each kind of defect are studied. The origin of dislocation clusters is discussed.

96

The optical properties of the $In_xGa_{1-x}N$ films are investigated by cathodoluminescence imaging and spectroscopy and are related to the observed defects in the films.

In chapter 6, $In_xGa_{1-x}N$ films with thickness ~ 60 nm and $x \geq 0.20$ grown by MBE are studied. Electron diffraction patterns and moiré fringes are used to determine the strain relaxation in these films. Moiré fringes reveal interfacial strain relaxation. It is found that with AlN templates, the onset of the interfacial relaxation happens at an indium content of ~ 0.48 while the InGaN films grown on GaN template do not have interfacial relaxation until indium content reaches ~ 0.67. A critical thickness shows that at large indium contents, the critical thickness for generation of misfit dislocations can be lower than one monolayer. This means in the initial stage the InGaN nucleates as relaxed films on the template with a misfit dislocation array on the interface.

7.2. Future work

For InAs QDs grown on AlGaAs, the photoluminescence at room temperature is low. This is probably due to high density of non-radiative recombination related to the defects in AlGaAs. Other matrix materials such as InP should be tried. Another important issue for QD solar cells is to efficiently separate electrons and holes to reduce recombination. One of the possible approaches is to replace InAs by GaSb to form type-II QDs. No matter what materials are used, the lattice mismatch between the QD material and the matrix material is required for the formation of QDs. Suppression of possible plastic relaxation is still needed. It would be interesting to study if partial capping and annealing works for different systems than InAs/AlGaAs.

InGaN films have been designed to function in solar cells operating at high temperatures. The stability of the materials at high temperatures is important. The effect of thermal annealing on the InGaN films with different indium contents should be studied. For indium content less than ~ 20%, InGaN is in a metastable regime. For indium content higher than ~ 20%, the material is unstable. It is expected that the changes of microstructures of InGaN in the two regimes will be different. On the other hand, the contact to p-type GaN is an issue for making good solar cell devices. The interface between the contact and p-GaN affects the contact resistance. Again, the stability of the contact at high temperatures is of great importance if the device is going to work at high temperatures.

Usually, solar cells are expected to work for about 20 years. An accelerated life test is needed to predict the performance of the solar cells. Many processes in the materials are exponentially dependent on temperature, so a relatively small time increase can accelerate the process a lot. Accelerated life testing is often performed by testing the material or device at a temperature higher than its working temperature and then using an Arrhenius equation to convert time to failure at elevated temperatures to service life at working temperature. Determination of the parameters in the Arrhenius equation is of great importance for this test. The structural and optical properties of the tested materials or devices can be characterized and slow processes can be studied.

REFERENCES

[1] F. K. Yam and Z. Hassan, Superlattices Microstruct. **43**, 1 (2008).

[2] R. Jakomin, R. M. S. Kawabata, R. T. Mourão, D. N. Micha, M. P. Pires, H. Xie, A. M. Fischer, F. A. Ponce, and P. L. Souza, J. Appl. Phys. **116**, 093511 (2014).

[3] I. Ramiro, J. Villa, P. Lam, S. Hatch, J. Wu, E. Lopez, E. Antolin, H. Liu, A. Marti, and A. Luque, IEEE J. Photovolt **5**, 840 (2015).

[4] Y. Kim, K. -Y. Ban, C. Zhang, and C. B. Honsberg, Appl. Phys. Lett. **107**, 08KA12 (2015).

[5] A. M. Fischer, Y. O. Wei, F. A. Ponce, M. Moseley, B. Gunning, and W. A. Doolittle, Appl. Phys. Lett. **103**, 131101 (2013).

[6] S. L. Rhode, W. Y. Fu, M. A. Moram, F. C. -P. Massabuau, M. J. Kappers, C. McAleese, F. Oehler, C. J. Humphreys, R. O. Dusane, and S. -L. Sahonta, J. Appl. Phys. **116**, 103513 (2014).

[7] C. A. M. Fabien, B. P. Gunning, W. A. Doolittle, A. M. Fischer, Y. O. Wei, H. Xie, and F. A. Ponce, J. Cryst. Growth **425**, 115 (2015).

[8] A. Yamamoto, K. Kodama, M. T. Hasan, N. Shigekawa, and M. Kuzuhara, Jpn. J. Appl. Phys. **54**, 08KA12 (2015).

[9] M. Jurisch, F. Borner, T. Bunger, S. Eichler, T. Flade, U. Kretzer, A. Kohler, J. Stenzenberger, and B. Weinert, J. Cryst. Growth **275**, 283 (2005).

[10] A. Maros, N. Faleev, R. R. King, C. B. Honsberg, D. Convey, H. Xie, and F. A. Ponce, J. Vac. Sci. Technol. B **34**, 02L113 (2016).

[11] D. Leonard, K. Pond, and P. Petroff, Phys. Rev. B **50**, 11687 (1994).

[12] D. Zhu, D. J. Wallis, and C. J. Humphreys, Rep. Prog. Phys. **76**, 106501 (2013).

[13] W. Utsumi, H. Saitoh, H. Kaneko, T. Watanuki, K. Aoki, and O. Shimomura, Nat. Mater. **2**, 735 (2003).

[14] Z. Wu, K. Nonaka, Y. Kawai, T. Asai, F. A. Ponce, C. Chen, M. Iwaya, S. Kamiyama, H. Amano, and I. Akasaki, Appl. Phys. Express **3**, 111003 (2010).

[15] R. Liu, J. Mei, S. Srinivasan, H. Omiya, F. A. Ponce, D. Cherns, Y. Narukawa, and T.

Mukai, Jpn. J. Appl. Phys. Part 2 **45**, L549 (2006).

[16] R. Liu, J. Mei, S. Srinivasan, F. A. Ponce, H. Omiya, Y. Narukawa, and T. Mukai, Appl. Phys. Lett. **89**, 201911 (2006).

[17] I. H. Ho and G. B. Stringfellow, Appl. Phys. Lett. **69**, 2701 (1996).

[18] S. Karpov, MRS Internet J. Nitride Semicond. Res. **3**, 16 (1998).

[19] X. M. Shen, Y. Fu, G. Feng, B. S. Zhang, Z. H. Feng, Y. T. Wang, and H. Yang, J. Cryst. Growth **246**, 69 (2002).

[20] R. People and J. C. Bean, Appl. Phys. Lett. **47**, 322 (1985).

[21] J. P. Hirth and J. Lothe, *Theory of Dislocations*, 2nd ed. (Krieger Publishing Company, Malabar, Florida, 1982).

[22] J. W. Matthews and A. E. Blakeslee, J. Cryst. Growth **27**, 118 (1974).

[23] A. Howie and M. J. Whelan, Proc. R. Soc. London, Ser. A **263**, 217 (1961).

[24] M. Vulovic, L. M. Voortman, L. J. van Vliet, and B. Rieger, Ultramicroscopy **136**, 61 (2014).

[25] J. Liu and J. M. Cowley, Ultramicroscopy **37**, 50 (1991).

[26] D. Cherns and A. R. Preston, J. Electron Microsc. Tech. **13**, 111 (1989).

[27] A. Luque, A. Martí, N. López, E. Antolín, E. Cánovas, C. Stanley, C. Farmer, L. J. Caballero, L. Cuadra, and J. L. Balenzategui, Appl. Phys. Lett. **87**, 083505 (2005).

[28] M. A. Kastner, Rev. Mod. Phys. **64**, 849 (1992).

[29] S. Ihara, A. Andreev, D. A. Williams, T. Kodera, and S. Oda, Appl. Phys. Lett. **107**, 013102 (2015).

[30] S. J. MacLeod, A. M. See, A. R. Hamilton, I. Farrer, D. A. Ritchie, J. Ritzmann, A. Ludwig, and A. D. Wieck, Appl. Phys. Lett. **106**, 012105 (2015).

[31] Y. Arakawa and H. Sakaki, Appl. Phys. Lett. **40**, 939 (1982).

[32] Y. Narukawa, Y. Kawakami, M. Funato, S. Fujita, S. Fujita, and S. Nakamura, Appl. Phys. Lett. **70**, 981 (1997).

[33] D. Bimberg, N. Kirstaedter, N. N. Ledentsov, Z. I. Alferov, P. S. Kopev, and V. M. Ustinov, IEEE J. Sel. Top. Quantum Electron. **3**, 196 (1997).

[34] D. L. Huffaker, G. Park, Z. Zou, O. B. Shchekin, and D. G. Deppe, Appl. Phys. Lett. **73**, 2564 (1998).

[35] S. Maimon, E. Finkman, G. Bahir, S. E. Schacham, J. M. Garcia, and P. M. Petroff, Appl. Phys. Lett. **73**, 2003 (1998).

[36] W. Shockley and H. J. Queisser, J. Appl. Phys. **32**, 510 (1961).

[37] A. Luque and A. Martí, Phys. Rev. Lett. **78**, 5014 (1997).

[38] A. Luque, A. Marti, and C. Stanley, Nat. Photonics **6**, 146 (2012).

[39] S. P. Bremner, R. Corkish, and C. B. Honsberg, IEEE Trans. Electron Devices **46**, 1932 (1999).

[40] D. Bimberg, M. Grundmann, and N. N. Ledentsov, *Quantum Dot Heterostructures* (John Wiley & Sons, Chicester, 1999).

[41] K. A. Sablon, J. W. Little, V. Mitin, A. Sergeev, N. Vagidov, and K. Reinhardt, Nano Lett. **11**, 2311 (2011).

[42] A. Luque and A. Martí, Adv. Mater. **22**, 160 (2010).

[43] E. Antolin, A. Marti, C. D. Farmer, P. G. Linares, E. Hernandez, A. M. Sanchez, T. Ben, S. I. Molina, C. R. Stanley, and A. Luque, J. Appl. Phys. **108**, 064513 (2010).

[44] K. Tillmann, D. Gerthsen, P. Pfundstein, A. Förster, and K. Urban, J. Appl. Phys. **78**, 3824 (1995).

[45] Y. Chen, X. W. Lin, Z. Liliental-Weber, J. Washburn, J. F. Klem, and J. Y. Tsao, Appl. Phys. Lett. **68**, 111 (1996).

[46] F. Tinjod and H. Mariette, Phys. Status Solidi B **241**, 550 (2004).

[47] Z. R. Wasilewski, S. Fafard, and J. P. McCaffrey, J. Cryst. Growth **201**, 1131 (1999).

[48] V. Polojarvi, A. Schramm, A. Aho, A. Tukiainen, and M. Guina, J. Phys. D: Appl. Phys. **45**, 365107 (2012).

[49] M. F. Ashby and L. M. Brown, Philos. Mag. **8**, 1083 (1963).

[50] R. M. Makhijani, S. Chakrabarti, and V. A. Singh, J. Lumin. **136**, 401 (2013).

[51] L. Nasi, C. Bocchi, F. Germini, M. Prezioso, E. Gombia, R. Mosca, P. Frigeri, G. Trevisi, L. Seravalli, and S. Franchi, J. Mater. Sci. Electron. **19**, S96 (2008).

[52] R. Vincent, Philos. Mag. **19**, 1127 (1969).

[53] A. Fischer, H. Kuhne, and H. Richter, Phys. Rev. Lett. **73**, 2712 (1994).

[54] S. W. Ellaway and D. A. Faux, J. Appl. Phys. **92**, 3027 (2002).

[55] O. Madelung, *Semiconductors: Data Handbook* (Springer, Berlin, Heidelberg, 2004).

[56] H. Toyoshima, T. Niwa, J. Yamazaki, and A. Okamoto, Appl. Phys. Lett. **63**, 821 (1993).

[57] A. A. Marmalyuk, O. I. Govorkov, A. V. Petrovsky, D. B. Nikitin, A. A. Padalitsa, P. V. Bulaev, I. V. Budkin, and I. D. Zalevsky, Nanotechnology **12**, 434 (2001).

[58] M. Grundmann, N. N. Ledentsov, O. Stier, D. Bimberg, V. M. Ustinov, P. S. Kopev, and Z. I. Alferov, Appl. Phys. Lett. **68**, 979 (1996).

[59] D. S. Sizov, Y. B. Samsonenko, G. E. Tsyrlin, N. K. Polyakov, V. A. Egorov, A. A. Tonkikh, A. E. Zhukov, S. S. Mikhrin, A. P. Vasil'ev, Y. G. Musikhin, A. F. Tsatsul'nikov, V. M. Ustinov, and N. N. Ledentsov, Semiconductors **37**, 559 (2003).

[60] M. Grundmann, J. Christen, N. N. Ledentsov, J. Bohrer, D. Bimberg, S. S. Ruvimov, P. Werner, U. Richter, U. Gosele, J. Heydenreich, V. M. Ustinov, A. Y. Egorov, A. E. Zhukov, P. S. Kopev, and Z. I. Alferov, Phys. Rev. Lett. **74**, 4043 (1995).

[61] N. Perret, D. Morris, L. Franchomme-Fosse, R. Cote, S. Fafard, V. Aimez, and J. Beauvais, Phys. Rev. B **62**, 5092 (2000).

[62] M. H. Degani and M. Z. Maialle, J. Comput. Theor. Nanosci. **7**, 454 (2010).

[63] I. E. Itskevich, M. S. Skolnick, D. J. Mowbray, I. A. Trojan, S. G. Lyapin, L. R. Wilson, M. J. Steer, M. Hopkinson, L. Eaves, and P. C. Main, Phys. Rev. B **60**, R2185 (1999).

[64] F. A. Ponce and D. P. Bour, Nature **386**, 351 (1997).

[65] S. Nakamura, N. Senoh, N. Iwasa, and S. I. Nagahama, Jpn. J. Appl. Phys., Part 2 **34**, L797 (1995).

[66] M. R. Krames, O. B. Shchekin, R. Mueller-Mach, G. O. Mueller, L. Zhou, G. Harbers, and M. G. Craford, J. Disp. Technol. **3**, 160 (2007).

[67] S. Nakamura, M. Senoh, S. Nagahama, N. Iwasa, T. Yamada, T. Matsushita, H. Kiyoku, and Y. Sugimoto, Jpn. J. Appl. Phys., Part 2 **35**, L74 (1996).

[68] S. Nakamura, M. Senoh, S. Nagahama, N. Iwasa, T. Yamada, T. Matsushita, Y. Sugimoto, and H. Kiyoku, Appl. Phys. Lett. **69**, 4056 (1996).

[69] O. Jani, I. Ferguson, C. Honsberg, and S. Kurtz, Appl. Phys. Lett. **91**, 132117 (2007).

[70] C. J. Neufeld, N. G. Toledo, S. C. Cruz, M. Iza, S. P. DenBaars, and U. K. Mishra, Appl. Phys. Lett. **93**, 143502 (2008).

[71] A. Koukitu and Y. Kumagai, J. Phys.: Condens. Matter **13**, 6907 (2001).

[72] S. Srinivasan, L. Geng, R. Liu, F. A. Ponce, Y. Narukawa, and S. Tanaka, Appl. Phys. Lett. **83**, 5187 (2003).

[73] J. Bruckbauer, P. R. Edwards, S. -L. Sahonta, F. C. -P. Massabuau, M. J. Kappers, C. J. Humphreys, R. A. Oliver, and R. W. Martin, J. Phys. D: Appl. Phys. **47**, 135107 (2014).

[74] F. C. -P. Massabuau, S. -L. Sahonta, L. Trinh-Xuan, S. Rhode, T. J. Puchtler, M. J. Kappers, C. J. Humphreys, and R. A. Oliver, Appl. Phys. Lett. **101**, 212107 (2012).

[75] J. Smalc-Koziorowska, E. Grzanka, R. Czernecki, D. Schiavon, and M. Leszczynski, Appl. Phys. Lett. **106**, 101905 (2015).

[76] P. Cantu, F. Wu, P. Waltereit, S. Keller, A. E. Romanov, S. P. DenBaars, and J. S. Speck, J. Appl. Phys. **97**, 674 (2005).

[77] F. A. Ponce, D. Cherns, W. T. Young, and J. W. Steeds, Appl. Phys. Lett. **69**, 770 (1996).

[78] F. Y. Meng, H. McFelea, R. Datta, U. Chowdhury, C. Werkhoven, C. Arena, and S. Mahajan, J. Appl. Phys. **110**, 073503 (2011).

[79] J. Smalc-Koziorowska, C. Bazioti, M. Albrecht, and G. P. Dimitrakopulos, Appl. Phys. Lett. **108**, 051901 (2016).

[80] K. Hiramatsu, Y. Kawaguchi, M. Shimizu, N. Sawaki, T. Zheleva, R. F. Davis, H. Tsuda, W. Taki, N. Kuwano, and K. Oki, MRS Internet J. Nitride Semicond. Res. **2**, U3 (1997).

[81] E. Sakalauskas, O. Tuna, A. Kraus, H. Bremers, U. Rossow, C. Giesen, M. Heuken, A. Hangleiter, G. Gobsch, and R. Goldhahn, Phys. Status Solidi B **249**, 485 (2012).

[82] Q. Yan, P. Rinke, A. Janotti, M. Scheffler, and C. G. de Walle, Phys. Rev. B **90**, 125118 (2014).

[83] T. Tao, T. Zhi, B. Liu, Y. Li, Z. Zhuang, Z. Xie, D. Chen, P. Chen, R. Zhang, and Y. Zheng, Status Solidi A **211**, 2823 (2014).

[84] G. B. Stringfellow, J. Cryst. Growth **68**, 111 (1984).

[85] F. A. Ponce, S. Srinivasan, A. Bell, L. Geng, R. Liu, M. Stevens, J. Cai, H. Omiya, H. Marui, and S. Tanaka, Phys. Status Solidi B **240**, 273 (2003).

[86] B. N. Pantha, J. Li, J. Y. Lin, and H. X. Jiang, Appl. Phys. Lett. **93**, 182107 (2008).

[87] A. V Blant, T. S. Cheng, C. T. Foxon, J. C. Bussey, S. V Novikov, and V. V Tret'yakov, MRS Proc. **449**, 465 (1996).

[88] R. Singh and T. D. Moustakas, MRS Proc. **395**, 163 (1995).

[89] S. Pereira, M. R. Correia, E. Pereira, K. P. O'Donnell, E. Alves, A. D. Sequeira, N. Franco, I. M. Watson, and C. J. Deatcher, Appl. Phys. Lett. **80**, 3913 (2002).

[90] R. R. Lieten, W. -J. Tseng, K. M. Yu, W. van de Graaf, J. -P. Locquet, J. Dekoster, and G. Borghs, CrystEngComm **15**, 9121 (2013).

[91] M. A. Moram, Z. H. Barber, and C. J. Humphreys, J. Appl. Phys. **102**, 023505 (2007).

APPENDIX A

LIST OF PUBLICATIONS DURING THE STUDY TOWARDS THE DOCTORAL

DEGREE

List of publications by Hongen Xie, during his Ph.D. studies at Arizona State University:

H. Xie, R. Prioli, A. M. Fischer, F. A. Ponce, R. M. S. Kawabata, L. D. Pinto, R. Jakomin, M. P. Pires, and P. L. Souza, *Improved optical properties of InAs quantum dots for intermediate band solar cells by suppression of misfit strain relaxation,* J. Appl. Phys. **120**, 034301 (2016).

A. Maros, N. Faleev, R. R. King, C. B. Honsberg, D. Convey, H. Xie, and F. A. Ponce, *Critical thickness investigation of MBE-grown GaInAs/GaAs and GaAsSb/GaAs heterostructures*, J. Vac. Sci. Technol. B **34**, 02L113 (2016).

Y. -S. Liu, A. F. M. S. Haq, T. -T. Kao, K. Mehta, S. -C. Shen, T. Detchprohm, P. D. Yoder, R. D. Dupuis, H. Xie, and F. A. Ponce, *Electrically conducting n-type AlGaN/GaN distributed Bragg reflectors grown by metalorganic chemical vapor deposition*, J. Cryst. Growth **443**, 81 (2016).

G. Torelly, R. Jakomin, L. D. Pinto, M. P. Pires, J. Ruiz, P. G. Caldas, R. Prioli, H. Xie, F. A. Ponce, and P. L. Souza, *Early nucleation stages of low density InAs quantum dots nucleation on GaAs by MOVPE*, J. Cryst. Growth **434**, 47 (2016).

X. Li, H. Xie, F. A. Ponce, J. -H. Ryou, T. Detchprohm, and R. D. Dupuis, *Onset of surface stimulated emission at 260nm from AlGaN multiple quantum wells*, Appl. Phys. Lett. **107**, 241109 (2015).

C. A. M. Fabien, B. P. Gunning, W. A. Doolittle, A. M. Fischer, Y. O. Wei, H. Xie, and F. A. Ponce, *Low-temperature growth of InGaN films over the entire composition range by MBE*, J. Cryst. Growth **425**, 115 (2015).

Y. -S. Liu, T. -T. Kao, M. M. Satter, Z. Lochner, S. -C. Shen, T. Detchprohm, P. D. Yoder, R. D. Dupuis, J. -H. Ryou, A. M. Fischer, Y. O. Wei, H. Xie, and F. A. Ponce, *Inverse-Tapered p-Waveguide for Vertical Hole Transport in High-[Al] AlGaN Emitters*, IEEE Photonics Technol. Lett. **27**, 1768 (2015).

X. -H. Li, S. Wang, H. Xie, Y. O. Wei, T. -T. Kao, M. M. Satter, S. -C. Shen, P. D. Yoder, T. Detchprohm, R. D. Dupuis, A. M. Fischer, and F. A. Ponce, *Growth of high-quality AlN layers on sapphire substrates at relatively low temperatures by metalorganic chemical vapor deposition*, Phys. Status Solidi B **252**, 1089 (2015).

X. -H. Li, Y. O. Wei, S. Wang, H. Xie, T. -T. Mao, M. M. Satter, S. -C. Shen, P. D. Yoder, T. Detchprohm, R. D. Dupuis, A. M. Fischer, and F. A. Ponce, *Temperature*

dependence of the crystalline quality of AlN layer grown on sapphire substrates by metalorganic chemical vapor deposition, J. Cryst. Growth **414**, 76 (2015).

X. -H. Li, T. -T. Kao, M. M. Satter, Y. O. Wei, S. Wang, H. Xie, S. -C. Shen, P. D. Yoder, A. M. Fischer, F. A. Ponce, T. Detchprohm, and R. D. Dupuis, *Demonstration of transverse-magnetic deep-ultraviolet stimulated emission from AlGaN multiple-quantum-well lasers grown on a sapphire substrate*, Appl. Phys. Lett. **106**, 041115 (2015).

X. -H. Li, T. Detchprohm, T. -T. Kao, M. M. Satter, S. -C. Shen, P. D. Yoder, R. D. Dupuis, S. Wang, Y. O. Wei, H. Xie, A. M. Fischer, F. A. Ponce, T. Wernicke, C. Reich, M. Martens, and M. Kneissl, *Low-threshold stimulated emission at 249 nm and 256 nm from AlGaN-based multiple-quantum-well lasers grown on sapphire substrates,* Appl. Phys. Lett. **105**, 141106 (2014).

R. Jakomin, R. M. S. Kawabata, R. T. Mourão, D. N. Micha, M. P. Pires, H. Xie, A. M. Fischer, F. A. Ponce, and P. L. Souza, *InAs quantum dot growth on AlxGa1−xAs by metalorganic vapor phase epitaxy for intermediate band solar cells*, J. Appl. Phys. **116**, 093511 (2014).

T. -T. Kao, Y. -S. Liu, M. M. Satter, X. -H. Li, Z. Lochner, P. D. Yoder, T. Detchprohm, R. D. Dupuis, S. -C. Shen, J. -H. Ryou, A. M. Fischer, Y. Wei, H. Xie, and F. A. Ponce, *Sub-250 nm low-threshold deep-ultraviolet AlGaN-based heterostructure laser employing HfO2/SiO2 dielectric mirrors*, Appl. Phys. Lett. **103**, 211103 (2013).

Z. Lochner, T. -T. Kao, Y. -S. Liu, X. -H. Li, M. M. Satter, S. -C. Shen, P. D. Yoder, J. -H. Ryou, R. D. Dupuis, Y. Wei, H. Xie, A. Fischer, and F. A. Ponce, *Deep-ultraviolet lasing at 243 nm from photo-pumped AlGaN/AlN heterostructure on AlN substrate*, Appl. Phys. Lett. **102**, 101110 (2013).